INFORMATION TO USERS

This manuscript has been reproduced from the microfilm master. UMI films the text directly from the original or copy submitted. Thus, some thesis and dissertation copies are in typewriter face, while others may be from any type of computer printer.

The quality of this reproduction is dependent upon the quality of the copy submitted. Broken or indistinct print, colored or poor quality illustrations and photographs, print bleedthrough, substandard margins, and improper alignment can adversely affect reproduction.

In the unlikely event that the author did not send UMI a complete manuscript and there are missing pages, these will be noted. Also, if unauthorized copyright material had to be removed, a note will indicate the deletion.

Oversize materials (e.g., maps, drawings, charts) are reproduced by sectioning the original, beginning at the upper left-hand corner and continuing from left to right in equal sections with small overlaps. Each original is also photographed in one exposure and is included in reduced form at the back of the book.

Photographs included in the original manuscript have been reproduced xerographically in this copy. Higher quality 6" x 9" black and white photographic prints are available for any photographs or illustrations appearing in this copy for an additional charge. Contact UMI directly to order.

UMI

A Bell & Howell Information Company
300 North Zeeb Road, Ann Arbor MI 48106-1346 USA
313/761-4700 800/521-0600

Reproduced with permission of the copyright owner. Further reproduction prohibited without permission.

Reproduced with permission of the copyright owner. Further reproduction prohibited without permission.

Metal-Insulator Transition in Stressed Si:B

by

Snezana Bogdanovich

A dissertation submitted to the Graduate Faculty in Physics in partial fulfillment of the requirements for the degree of Doctor in Philosophy, the City University of New York.

1998

Reproduced with permission of the copyright owner. Further reproduction prohibited without permission.

UMI Number: 9820512

Copyright 1998 by
Bogdanovich, Snezana

All rights reserved.

UMI Microform 9820512
Copyright 1998, by UMI Company. All rights reserved.

This microform edition is protected against unauthorized
copying under Title 17, United States Code.

UMI
300 North Zeeb Road
Ann Arbor, MI 48103

Reproduced with permission of the copyright owner. Further reproduction prohibited without permission.

© 1998

Snezana Bogdanovich

All Rights Reserved

Reproduced with permission of the copyright owner. Further reproduction prohibited without permission.

This manuscript has been read and accepted for the Graduate Faculty in Physics in satisfaction of the dissertation requirement for the degree of Doctor of Philosophy.

1/13/98
Date

Myriam P. Sarachik
Dist. Prof. Myriam Sarachik

1/13/98
Date

Prof. Lou Celenza
Executive Officer

Supervisory Committee

Prof. Ravindra N. Bhatt
Prof. Joseph Birman
Prof. Joseph Krieger
Prof. Frederick W. Smith
Dr. Gordon A. Thomas

THE CITY UNIVERSITY OF NEW YORK

Reproduced with permission of the copyright owner. Further reproduction prohibited without permission.

ABSTRACT

Metal-Insulator Transition in Stressed Si:B

by

Snezana Bogdanovich

Thesis Advisor: Dist. Prof. Myriam P. Sarachik

This manuscript contains three chapters: (i) Chapter I contains a review of the theory of metal-insulator transitions in doped semiconductors and a review of the scaling theory of localization and its results. (ii) Chapter II contains experimental data on the magnetoconductance of metallic Si:B. It will be shown that the conductivity data for Si:B with dopant concentrations $1.01n_c < n < 1.22n_c$ obey universal scaling of the form expected for electron-electron interactions for a large range of magnetic fields and temperatures. The existence of this scaling implies that the metal-insulator transition is dominated by interactions. Detailed analysis of the data show that the localization, spin-orbit and spin-flip interactions do not play an important role in transport processes in this material.

Reproduced with permission of the copyright owner. Further reproduction prohibited without permission.

(iii) Chapter III contains experimental data on the stress-tuned metal-insulator transition in Si:B. Uniaxial stress drives a metallic sample into the insulating phase by decreasing the impurity wavefunction overlap and increasing the value of the critical concentration n_c. The conductivity obeys dynamical scaling as a function of temperature and stress near the critical point in both metallic and insulating phases. Important findings are:

a) the approach to the transition by variation of stress and variation of the dopant concentration are very different.

b) the critical conductivity has a $T^{1/2}$ behavior similar to the conductivity outside the critical region due to electron-electron interactions.

c) the conductivity of the insulator obeys Efros-Shklovskii hopping due to electron-electron interactions $\sigma \sim T^{1/2}\exp[-(T_0/T)^{1/2}]$ with a temperature dependent prefactor $\propto T^{1/2}$.

Reproduced with permission of the copyright owner. Further reproduction prohibited without permission.

DEDICATION

This work is lovingly dedicated to my mother Toda

Reproduced with permission of the copyright owner. Further reproduction prohibited without permission.

Acknowledgments

There are many people whose ideas, help, guidance and support I benefited from during my Ph. D. years.

Professor Myriam P. Sarachik, my thesis advisor has shown continuous interest in my work and progress. Her moral support and encouragement in my experiment on uniaxial stress, when things didn't go very well, were crucial for its later success. She always had excellent ideas regarding the experiment and data analysis. I am very grateful for her guidance in my research and help in editing this thesis.

I have been fortunate to have Dr. Gordon Thomas from Lucent Technologies as my second advisor. I benefited greatly from his professional expertise as an experimentalist and from his extensive knowledge of the physics of doped semiconductors. He has shown great interest in my career and has often advised me regarding my professional future. I am very happy to have him as a friend.

I owe my gratitude to professor Vladimir Dobrosavljevic a theorist from Florida State University with a rare talent for easy communication with experimentalists. He clarified and explained many complicated theoretical concepts necessary to understand our results on magnetoconductance of Si:B. Personally, I learned a great deal of physics from many conversations with him. He was always extremely supportive of my work and looked forward to help me professionally and personally. I am very grateful for his friendship and his understanding.

I would like to thank Professor Ravindra Bhatt from Princeton University for help in understanding the effects of stress on the band structure and metal-insulator transition. His suggestions in analyses of the data on stress were extremely useful.

Dr. Peihua Dai a former postdoc in the Sarachik group has taught me many experimental skills and low temperature techniques. He always shared his extensive experience and knowledge in the area of doped

Reproduced with permission of the copyright owner. Further reproduction prohibited without permission.

semiconductors and continued being a great source of information even when he left the group.

Dr. Eric Smith from Cornell University gave me much good advice, experimental tips, and provided experimental parts that were crucial in succeeding with the experiment on uniaxial stress.

The advice and expertise of Dr. Dale Jacobson from Lucent Technologies in B^+ ion implanting of Si:B is very much appreciated.

Professor Mikko Paalanen from Helsinki University of Technology had some very useful suggestions regarding the experiment on stress. His experience and knowledge of low temperature techniques and uniaxial stress were very valuable to me.

I thank Prof. Tom Rosenbaum form University of Chicago for lending me his capacitance bridge and advising me on many aspects of the experiment on stress.

I had many interesting and enlightening discussions with Professor Joseph Birman related to band structure and symmetry related properties of crystals. It was always a pleasure talking to him.

Professor Fred Pollak from Brooklyn College has done many studies of the effect of stress on the band structure of p-type Ge and Si, in particular in Si:B. His suggestions and vast knowledge in this area were extremely useful to me. I also thank him for letting me use some of his Si:B samples.

Dr. Jonathan Friedman was a graduate student of Professor Sarachik's group with whom I worked closely. Although we worked on two different projects, he always showed great interest in my work, asking important questions and suggesting ideas regarding my research. I have learned many computer skills from his tutorials and gained a better understanding of physics in general through many discussions with him. I am most grateful to him for his constant support, encouragement and being a very good friend to me.

Dr. Sergey Kravchenko current member of the Sarachik group, assisted me many times with the experiment and measurements on stress and had very useful suggestions in data analysis.

Reproduced with permission of the copyright owner. Further reproduction prohibited without permission.

Dmitri Simonian, graduate student of the Sarachik group helped me with the measurements on my last experimental runs. I appreciate his comments and his input.

Lucianne Walkovich a high school student did a great amount of work on the experimental setup and mounting of the different experimental parts of the apparatus for stress.

Aicha Diop an undergraduate student of City College did lots of sample preparation and characterization for my latest project on stress.

Graduate student Yicheng Zhong, a recent member of Sarachik group assisted me with some preparations for the project on stress.

I am very grateful to Professor Maria Tamargo, Professor Marilyn Gunner, Professor Frederick Smith, Professor Herman Cummins, Professor Kurt Becker, Professor Robert Alfano and the members of their groups for letting me use their laboratory equipment many times and assisting me whenever I needed it.

Mr. Joseph Altmann and the machine shop crew constructed many parts of the experimental apparatus. They advised me many times in the design of the equipment and often gave my work priority. I am very grateful to them for taking their time to instruct me in technical drawing.

I also would like to thank the members of my thesis committee for their interest in my work and for reading this manuscript.

This work would have not been possible without the financial support of The Department of Energy.

Last, I want to thank my sister Gordana Bašic and her family, and my mother Toda Bogdanovic for continuous emotional support and care for my work and my future.

Reproduced with permission of the copyright owner. Further reproduction prohibited without permission.

Table of Contents

Abstract iv
Dedication vi
Acknowledgments vii
List of Tables xi
List of Figures xii

Chapter I: Introduction and Background 1
Introduction 1
A. Scaling Theory of Localization 6
B. Corrections to the Boltzmann Conductivity 7
1. Noninteracting gas of electrons-weak localization 7
2. Interaction effects 9

Chapter II: Universal Scaling of the Magnetoconductance of Metallic Si:B 11
A. Magnetoconductance-Theoretical Background 11
1. Magnetoconductivity Due to Interactions 12
2. Magnetoconductivity Due to Weak Localization 14
B. Experimental Procedure 16
1. Sample preparation 16
2. Sample characterization 17
3. Experimental setup 18
3.1 Sample holder 18
3.2 Thermometry and temperature control 19
3.3 Electrical wiring 21
3.4 Superconducting magnet 21

Reproduced with permission of the copyright owner. Further reproduction prohibited without permission.

3.5 Low AC resistance measurement 22

3.6 Data Acquisition 22

C. Results and Discussion 23

Chapter III: Stress-Induced Metal-Insulator Transition in Si:B 35

A. Metal-Insulator Transition-Scaling Theory 35

1. Dynamical scaling Law 35

1.1 Critical exponents-Universality classes 38

2. Stress-Induced Metal-Insulator Transition 41

2.1 Effective Mass Approximation 41

2.2 Effect of stress on the impurity wave functions-MIT 48

3. Stress-Induced MIT in p-type Si:B 53

3.1 Band Structure of p-type Semiconductors 53

3.2 Acceptor states in EMA 55

3.3 The Effect of Stress on the Valence Band and The Acceptor Ground State of Si 56

3.4 Stress-induced MIT for p-type Si:B 60

B. Experimental Procedure 62

1. Sample Preparation and Characterization 62

2. Experimental setup 63

2.1 Pressure Cell 66

2.1a Design 66

2.1b Calibration 67

2.1c Capacitance measurement 69

2.2 Gas handling system 69

2.3 Electrical wiring 72

2.4 Thermometry and temperature control 73

Reproduced with permission of the copyright owner. Further reproduction prohibited without permission.

2.5 Resistance measurement 74

C. Results and Discussion 75

1. Dynamical Scaling of the Conductivity near the MIT 79

2. Metallic Conductivity-Critical Behavior 90

3. Approach to the MIT from the Insulating Side 96

Summary 108

Suggestions for future work 111

Bibliography 113

Reproduced with permission of the copyright owner. Further reproduction prohibited without permission.

List of Tables

TABLE II-B: Sample designation, room temperature... 18
TABLE III-A: List of uncompensated and compensated... 39,40
TABLE III-B: Room temperature resistivity, ... 63
TABLE III-C-1: Critical stress, exponent ... 89
TABLE III-C-2: Critical parameters for Si:B ... 94

Reproduced with permission of the copyright owner. Further reproduction prohibited without permission.

List of Figures

Fig. I-1 a) Disappearance... b) At the critical ... 2

Fig. I-2 a) Energy E_m separates... b) In a localization .. 4

Fig. II-1 The glass mixing ... 20

Fig. II-2 Conductivity in zero magnetic field ... 24

Fig. II-3 Conductivity as a function of $T^{1/2}$ 26

Fig. II-4 Conductivity as a function of magnetic... 28

Fig. II-5 $-\Delta\sigma/T^{1/2}$ versus H/T for samples A through G... 30

Fig. II-6 $[-\Delta\sigma/T^{1/2}/K]$ versus H/T for samples A ... 31

Fig. II-7 $[-\Delta\sigma/T^{1/2}/K]$ versus H/T for samples A ... 33

Fig. III-1a) Phosphorus atoms...b) Donors form... 42

Fig. III-2 The Mott-Hubbard transition at zero ... 52

Fig. III-3 Energy surfaces of degenerate heavy ... 54

Fig. III-4 Splitting of the heavy and light 56

Fig. III-5 Energy level shifting as a function of 58

Fig. III-6 Resistivity at 4.2K normalized to its ... 59

Fig. III-7 The Mott-Hubbard transition at zero ... 61

Fig. III-8 Pressure cell 64

Fig. III-9 Insert of the dilution fridge with ... 65

Fig. III-10 Several calibration curves ... 68

Fig. III-11 Gas handling system 70

Fig. III-12 Current I and voltage V configuration ... 74

Fig. III-13 Conductivity as a function of stress ... 76

Fig. III-14 Conductivity as a function of boron... 77

Fig. III-15 $\ln\sigma$ as a function of lnT ... 78

Reproduced with permission of the copyright owner. Further reproduction prohibited without permission.

Fig. III-16 Ratio of the conductivity at different ... 81

Fig. III-17 Ratio of the conductivity at different ... 82

Fig. III-18 Ratio of the conductivity at different ... 83

Fig. III-19 Ratio of the conductivity at different ... 84

Fig. III-20 Ratio of the conductivity at different ... 85

Fig. III-21 Ratio of the conductivity at different ... 86

Fig. III-22 Conductivity as a function of ... 87

Fig. III-23 Conductivity as a function of ... 88

Fig. III-24 Conductivity as a function of $T^{1/2}$ ... 91

Fig. III-25 Conductivity as a function of $T^{1/2}$ ... 92

Fig. III-26 Zero-temperature conductivity as 93

Fig. III-27 $\ln\sigma$ as a function of $T^{-1/2}$ ... 97

Fig. III-28 T_0 as a function of uniaxial stress S. 98

Fig. III-29 Semi-log plot of the ratio of σ/σ_c... 101

Fig. III-30 $\ln[(\sigma/\sigma_c)(T/T^*)^y]$ for S_c=613 bar ... 102

Fig. III-31 Semi-log plot of the ratio of σ/σ_c ... 103

Fig. III-32 Semi-log plot of the ratio of σ/σ_c ... 104

Fig. III-33 $\ln(\sigma/T^{1/2})$ as a function of $T^{-1/2}$... 106

Fig. III-34 a) Zero-temperature...b) T* as a ... 107

Reproduced with permission of the copyright owner. Further reproduction prohibited without permission.

CHAPTER I

INTRODUCTION

The Metal-Insulator transition in disordered systems has been the object of intensive theoretical and experimental study over the past three decades. Doped semiconductors with a random distribution of impurities are typical examples of disordered systems that undergo a transition from insulating to metallic behavior when the concentration of impurities is increased above some critical value n_c. Metallic behavior is characterized by a finite conductivity in the limit of zero-temperature, while the conductivity of insulators vanishes in the limit of zero-temperature.

Historically, two different models of the metal-insulator transition have been developed:

a) The Mott-Hubbard model[1] considers a metal-insulator transition driven by electron correlations. This model treats only the Coulomb repulsion between electrons on the same impurity site, neglecting the disorder associated with the random distribution of impurities. At low concentrations of impurities in the insulating phase, the Coulomb repulsion of two electrons opens a gap in the density of states that separates the upper Hubbard (doubly occupied) band and lower Hubbard (singly occupied) band. Increasing the impurity concentration broadens the two bands until they merge; the metallic phase is entered when the gap disappears (see Fig. I-1a). This transition is discontinuous and entails a minimum metallic conductivity, as shown in Fig. I-1b.

Reproduced with permission of the copyright owner. Further reproduction prohibited without permission.

The Mott-Hubbard transition

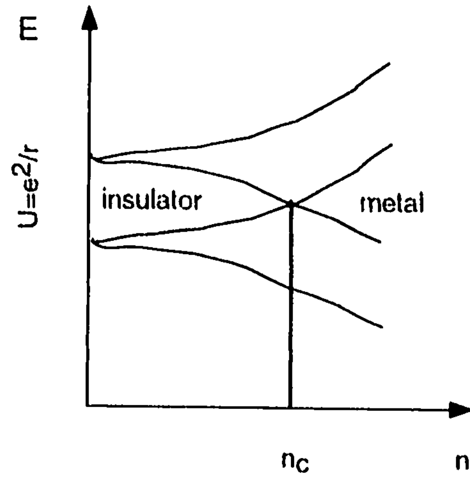

Fig. I-1a. Disappearance of the gap U with the merging upper and lower Hubbard band indicates the Mott-Hubbard transition.

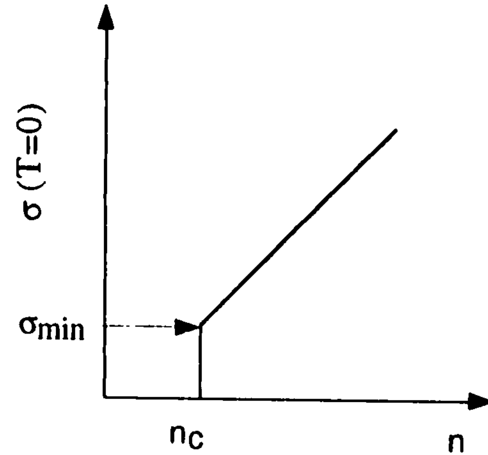

Fig. I-1b. At the critical concentration n_c conductivity goes to zero discontinuously.

Reproduced with permission of the copyright owner. Further reproduction prohibited without permission.

b) The Anderson[2] model considers a metal-insulator transition driven by disorder. This model deals only with a random impurity potential, neglecting the electron-electron interactions. For high enough disorder all the states are localized exhibiting insulating behavior. There is a critical value of disorder below which delocalized states begin to appear in the middle of the band; as the disorder decreases further, the region of extended states becomes larger, eventually filling the whole band (see Fig I-2a). Metallic behavior corresponds to a Fermi level that lies in the region of delocalized states. Here the metal-insulator transition occurs when the Fermi level crosses the mobility edge (the energy separating localized from delocalized states). In this model, the zero temperature conductivity vanishes continuously at the transition, as shown in Fig. I-2b. For comparison, the conductivity for a percolation transition is also presented in Fig. I-2b. In contrast to the localization transition which is a quantum phase transition, the percolation transition that happens in highly disordered media (granular metals, alloys) is of a classical nature. The conductivity vanishes continuously, but with a much bigger critical conductivity exponent than for a localization transition.

Based on a number of experimental results, largely on the elegant stress-tuning experiments of Paalanen et al.[3], the metal-insulator transition that occurs in doped semiconductors is generally believed to be a continuous phase transition[4] and the minimum metallic conductivity characteristic of a discontinuous Mott transition appears to be absent. On the other hand, the observed temperature dependence of the conductivity, the temperature dependence of the Hall coefficient, and the behavior of the magnetoresistance discussed in Chapter I

Reproduced with permission of the copyright owner. Further reproduction prohibited without permission.

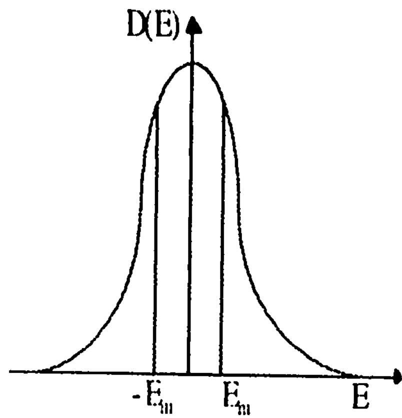

Fig. I-2a. Energy E_m separates delocalized states at the center of the band from the localized states in the tails of the band.

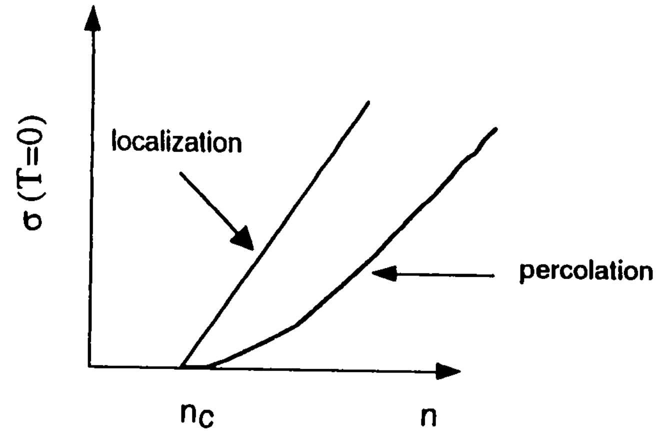

Fig. I-2b. In a localization or percolation transition zero-temperature conductivity goes to zero continuously.

Reproduced with permission of the copyright owner. Further reproduction prohibited without permission.

clearly indicate the importance of electron-electron interactions. Both electron-electron interactions and localization play important roles in the transport properties of doped semiconductors; however, their relative importance in driving the transition continues to be a subject of investigation and debate.

Since a magnetic field is expected to induce different changes in conductivity depending on whether they originate from localization or interactions, the magnetoconductance is in general a useful tool to separate these two contributions. Chapter I gives a review of the scaling theory of localization, and corrections to the Boltzmann conductivity arising from both disorder and electron-electron interactions. Chapter II contains a detailed study of the magnetoconductance of Si:B; these results indicate that electron-electron interactions strongly dominate the behavior of the magnetoconductance of this material. Chapter III is devoted to the effects of uniaxial stress on the conductivity of p-type Si:B and its critical behavior. It will be shown that the approach to the metal-insulator transition in this material by varying the compressive uniaxial stress is very different from the unstressed case, where one changes the dopant concentration to approach the transition.

Reproduced with permission of the copyright owner. Further reproduction prohibited without permission.

A. Scaling Theory of Localization

Many of the important ideas of the scaling theory of localization derive from work of David Thouless and his coworkers[5] in the 1970's. In this approach one considers a hypercube of size L in a d-dimensional space which has a conductance G(L). One can solve the Hamiltonian of a single particle interacting with a random potential in the hypercube. The average spacing between single particle levels is $w = (N_0 L^d)^{-1}$, where N_0 is the number of energy levels per unit volume and per unit energy. If we increase the sample size by putting together hypercubes of size L, the eigenstates of the larger system will be different from those obtained for the separate hypercubes. If the width of an eigenstate dE is much smaller then the separation between the energy levels w, or $dE/w << 1$, the eigenstates in adjoining hypercubes won't mix appreciably, and the eigenstates of the $(2L)^d$ sample will be localized. On the other hand, if $dE/w >> 1$ the eigenstate of the $(2L)^d$ sample will be extended. Thus, Thouless argued that whether the wavefunction is localized or extended depends on the ratio dE/w as the length scale is increased. This ratio is related to the conductance G of the sample by $G = (e^2 / \hbar)(dE/w)$. One can introduce a dimensionless conductance $g = G/(e^2 / \hbar)$, which is a physically measurable quantity. The concept of dimensionless conductance led to the scaling theory of localization.

In 1976 Franz Wegner formulated a scaling theory in analogy with critical phenomena in which g plays the role of the scaling variable[6]. At the critical point the conductivity is expected to vanish continuously as the impurity concentration approaches a critical value n_c.

Reproduced with permission of the copyright owner. Further reproduction prohibited without permission.

$$\sigma = \sigma_0 \left(\frac{n - n_c}{n}\right)^{\mu} \qquad \text{(I-A-1)}$$

Abrahams, Anderson, Licciardello and T. V. Ramakrishnan[7] formulated a one-parameter scaling theory by postulating that the dimensionless conductance g is the only scaling variable. Following the concept of scaling theory of localization, diagrammatic perturbation theory was developed. Section B summarizes the corrections to the Boltzman conductivity calculated by diagrammatic perturbation methods.

B. Corrections to the Boltzman Conductivity

1. Noninteracting gas of electrons- Weak Localization

The conductivity of a noninteracting gas of electrons can be calculated using the Kubo formula[8] for which the perturbation expansion is represented by Feynman diagrams. In disordered systems such as doped semiconductors, electrons scatter frequently, due to the random nature of the impurity potential[9]. The elastic scattering of electrons by impurities does not destroy phase coherence of the electron wave function. The average distance between two elastic scattering events is the elastic mean free path l. In order to calculate the probability of an electron propagating from point A to point B, one must sum the probabilities of all possible paths connecting A and B. Waves taking different paths will arrive at B with random phases, averaging to zero. However, this is not true when one considers closed loops, or the

Reproduced with permission of the copyright owner. Further reproduction prohibited without permission.

probability of returning to the starting point. Any closed path and its time-reversed path interfere constructively, enhancing the probability of the electron returning to the starting point. This phenomenon, referred to as weak localization, inhibits the transport of electrons and thus diminishes the conductivity. The divergent term in the expansion of the Kubo formula leading to weak localization is usually called the particle-particle (Cooper) channel. In three dimensions, the correction to the Boltzmann conductivity arising from weak localization has the following form

$$\sigma_{3d}(L) = \sigma_B - \frac{e^2}{\hbar\pi}[\frac{1}{l} - \frac{1}{L}] \qquad \text{(I-B-1.1)}$$

where $\sigma_B = ne^2\tau/m^*$ is the Boltzmann conductivity, l is the elastic mean free path and L is the size of the sample.

Inelastic scattering of electrons destroys the phase coherence which is the origin of weak localization. Electrons diffuse a distance L_{Th} between dephasing inelastic collisions and localization effects are cutoff beyond L_{Th}. L_{Th} is given by $L_{Th} = (D\tau_{in})^{1/2}$, where D is the diffusion constant and τ_{in} is the inelastic scattering time. The inelastic scattering time depends on temperature as $\tau_{in} \propto T^{-p}$, where p depends on which scattering mechanism (electron-phonon, electron-electron etc.) is dominant in a given temperature range. This gives $L_{Th} = aT^{-p/2}$; the correction to the Boltzmann conductivity then becomes $\Delta\sigma_L = BT^{p/2}$, where B is a constant. The correction $\Delta\sigma_L$ is positive and increases with decreasing temperature due to the diverging nature of L_{Th} as $T\rightarrow 0$.

Reproduced with permission of the copyright owner. Further reproduction prohibited without permission.

2. *Interaction effects*

Coulomb interactions between electrons in metals are of the same order as the kinetic energy of the electrons (30-40meV). Still, most of the properties of metals can be described by treating the electrons as a noninteracting gas of Fermions. Landau's Fermi-liquid theory describes the strongly interacting Fermi gas in terms of weakly interacting quasiparticles. This theory is valid only in translationally invariant systems (without disorder). Altshuler and Aronov[10,11,12] calculated corrections to the conductivity of a weakly disordered electron gas arising from the electron-electron interactions. The dominant correction arises from the particle-hole channel, which in 3-d has the following form:

$$\Delta\sigma_I = \alpha\left(\frac{4}{3} - \frac{3}{2}\gamma F_\sigma\right)T^{\frac{1}{2}} \qquad \text{(I-B-2.1)}$$

where $\alpha = \frac{e^2}{\hbar}\frac{1.3}{4\pi^2}\frac{1}{\sqrt{2D}}$, D is diffusion constant and F_σ is an interaction parameter related to the Fermi-liquid parameter F, the Fermi-surface average of the screened electron-electron interaction [11]

$$F_\sigma = -\frac{32}{3}\left[1 - \frac{3F}{4} - \left(1 - \frac{F}{2}\right)^{\frac{3}{2}}\right]F. \qquad \text{(I-B-2.2)}$$

The value of γ depends on the valley degeneracy, mass anisotropy, and intervalley scattering[13], and it is not known for Si:B. The Fermi-liquid parameter that results from the Hartree interaction can be written as

Reproduced with permission of the copyright owner. Further reproduction prohibited without permission.

$$F=(1/x)\ln(1+x), \qquad \text{(I-B-2.3)}$$

where $x=(2k_F/K)^2$, k_F is the Fermi wave number and K is the Thomas-Fermi screening wave vector. The screening length K^{-1} becomes very large near the transition, and F goes to zero approaching the transition.

Reproduced with permission of the copyright owner. Further reproduction prohibited without permission.

CHAPTER II

UNIVERSAL SCALING OF THE MAGNETOCONDUCTANE OF METALLIC Si:B[14]

A. Magnetoconductance-Theoretical Background

As shown in the preceding chapter, the conductivity of a doped semiconductor has the following form:

$$\sigma(T) = \sigma(T=0) + mT^{\frac{1}{2}} + BT^{\frac{p}{2}} \qquad \text{(II-A-1)}$$

where the second term is the correction due to electron-electron interactions and the third term is the correction due to localization. Localization and electron-electron interactions play crucial roles in determining the behavior of doped semiconductors near metal-insulator transition. The application of a magnetic field causes different changes in the conductivity depending on whether they arise from localization or interactions, and the magnetoconductance has often been used to attempt to separate these components. To leading order, the magnetoconductance due to localization and electron correlations are additive:

$$\Delta\sigma = \sigma(H,T) - \sigma(0,0) = \Delta\sigma_I(H,T) + \Delta\sigma_L(H,T) \qquad \text{(II-A-2)}$$

Reproduced with permission of the copyright owner. Further reproduction prohibited without permission.

1. Magnetoconductivity due to interactions

In the absence of a magnetic field, the interaction term due to the particle-hole channel is given by equation (I-B-2.1). A magnetic field splits the spin-up and spin-down bands and gives rise to two terms:[8,11,15,16,17]

$$\Delta\sigma_I(H,T) = \sigma_I(H,T) - \sigma_I(0,0) = \Delta\sigma'_I(T) + \Delta\sigma''_I(H,T), \quad \text{(II-A-1.1)}$$

where $\Delta\sigma'_I(T) = \alpha[4/3-\gamma F_\sigma/2]T^{1/2}$ is the field-independent exchange + singlet Hartree contribution and $\Delta\sigma''_I(H,T) = -0.77\alpha\gamma F_\sigma T^{1/2} g_3(h) - \alpha\gamma F_\sigma T^{1/2}$ is the spin dependent triplet contribution, with $h = g\mu_B H/k_B T$, and

$$g_3(h) = \int_0^\infty d\Omega[\Omega/(e^\Omega - 1)]\{(\Omega+h)^{1/2} + (|\Omega-h|)^{1/2} - 2\Omega^{1/2}\}. \quad \text{(II-A-1.2)}$$

The limiting behavior of $g_3(h)$ is the following:

$$g_3(h) = \begin{cases} \sqrt{h} - 1.3 & h \gg 1 \\ 0.053h^2 & h \ll 1 \end{cases} \quad \text{(II-A-1.3)}$$

The quantity that is deduced experimentally is the difference at finite temperature T between the conductivity in a magnetic field and in zero field:

Reproduced with permission of the copyright owner. Further reproduction prohibited without permission.

$$\Delta\sigma_I = \sigma_I(H,T) - \sigma_I(0,T) = -0.77\alpha\gamma F_\sigma T^{1/2} g_3(h) \qquad \text{(II-A-1.4)}$$

The contribution to the magnetoconductance due to the particle-hole channel of the interacting electron gas is negative (positive magnetoresistance).

The magnetoconductivity arising from orbital effects associated with the Cooper channel in an interacting electron gas is also negative and has the following form[18]:

$$\Delta\sigma_{int}(H,T) = -g(T)\frac{e^2}{2\pi^2\hbar}\left(\frac{eH}{\hbar c}\right)^{1/2}\varphi_3\left(\frac{2DeH}{\pi cT}\right) \qquad \text{(II-A-1.5)}$$

where the interaction constant g(T) > 0 for the mutual repulsion of electrons, D is a diffusion constant and H is magnetic field. The limiting behavior of the function φ_3 is:

$$\varphi_3 = \begin{cases} 1.9 & x >> 1 \\ 0.33x^{3/2} & x << 1 \end{cases} \qquad \text{where } x = 2DeH/\pi cT. \qquad \text{(II-A-1.6)}$$

Reproduced with permission of the copyright owner. Further reproduction prohibited without permission.

2. Magnetoconductivity Due to Weak Localization

A magnetic field breaks time reversal symmetry and destroys the quantum interference between the time-reversed backscattered loops responsible for localization effects. The destruction of localization leads to an increase of the conductivity with magnetic field (positive magnetoconductance). The magnetoconductance due to weak localization is given by the following expression[18]:

$$\Delta\sigma_L(H,T) = \frac{e^2}{2\pi^2\hbar}\left(\frac{eH}{\hbar c}\right)^{1/2} f_3\left(\frac{4DeH}{\hbar c}\tau_\varphi\right) \qquad \text{(II-A-2.1)}$$

where D and H are the diffusion constant and magnetic field, respectively, and τ_φ is the inelastic scattering time. The limiting behavior of the function f_3 is:

$$f_3(x) = \begin{cases} 0.6 & x \gg 1 \\ x^{3/2}/48 & x \ll 1 \end{cases}, \qquad \text{where } x=(4DeH/\hbar c)\tau_\varphi \qquad \text{(II-A-2.2)}$$

The presence of strong spin-orbit effects results in coherent back-scattering that is out-of-phase rather than in-phase, leading to destructive rather than constructive interference for a closed loop path, or antilocalization. In this case the application of a magnetic field dephases the destructive interference, yielding a negative magnetoconductance. In many materials studied to date, spin-orbit scattering is associated with the presence of impurities which have large mass. In p-type materials such as Si:B, however, strong spin orbit effects are expected, but they are instead associated with the nature of

Reproduced with permission of the copyright owner. Further reproduction prohibited without permission.

the valence band of the host material itself. Silicon has degenerate light and heavy-hole $J=3/2$ valence bands at $k=0$ and a spin-orbit split $J=1/2$ band 44 meV below these. The scattering by impurities causes transitions among states of different m_J values at a rate comparable to ordinary potential scattering[19,20].

According to Altshuler et al.[18,21], the magnetoconductivity of a p-type semiconductor is given by:

$$\Delta\sigma_L = \sigma_L(H,T) - \sigma_L(0,T) = -1/4\Sigma_0 + 3/4\Sigma_1 - 5/4\Sigma_2 + 7/4\Sigma_3. \qquad \text{(II-A-2.3)}$$

where the four terms correspond to total angular momentum $J = j_1 + j_2$ ($j_1=j_2=3/2$) of two holes with values 0, 1, 2 and 3.
Σ_0 is the same as without the spin-orbit scattering[22], which is:

$$\Sigma_0 = (e^2/2\pi^2\hbar)(eH/\hbar)^{1/2} f(H/H_i), \qquad \text{(II-A-2.4)}$$

where $H_i = (\hbar/4De)\tau_{in}^{-1}$, and the other terms have not been calculated. For strong spin-orbit scattering the first term of equation (II-A-2.3) gives the major contribution in small magnetic fields. The magneto-conductivity due to weak antilocalization for small magnetic fields is then given by:

$$\Delta\sigma_L(H,T) \approx -1/4\Sigma_0 \propto H^2 \qquad \text{(II-A-2.5)}$$

Significant contributions to the magnetoconductance associated with localization have been observed in many systems[23], yielding information regarding the dominant phase-breaking processes. On the other hand, magnetoconductance measurements in Si:P[24] at very low

Reproduced with permission of the copyright owner. Further reproduction prohibited without permission.

temperature have shown that electron correlations are very important in this bellwether material.

As described below, our measurements of the magnetoconductance of metallic Si:B near the metal-insulator transition demonstrate that electron-electron interactions strongly dominate the behavior of this system.

B. Experimental Procedure

1. Sample Preparation

The samples for these measurements had already been prepared by Dr. Peihua Dai. Details of sample preparation, attaching contacts, and sample characterization can be found in his earlier publications[25,26] and his Ph.D. thesis[27]. A brief summary is given below:

Samples were purchased as wafers of thickness 0.3 mm from Pensilco Corporation (currently called Puresil). They were grown by the Czochralski method. Their segregation coefficient (ratio of the equilibrium concentration of dopant in the crystal to that in the melt)[28] is 0.8, which makes these crystals considerably more homogeneous compared to Si:P (segregation coefficient = 0.35). Samples were cut into bars of approximate dimensions 8x1.5x0.3 mm^3 . They were then etched in a CP-4 solution to remove any mechanical surface damage and impurities incurred during the cutting process. Each sample was ion-implanted on four thin striplike areas to insure good

Reproduced with permission of the copyright owner. Further reproduction prohibited without permission.

electrical contact to the surface. Four wires were attached to the implanted areas by an arc discharge technique[29].

2. Sample Characterization

The room temperature resistivity of a large number of Si:B samples was measured in the van der Pauw[30] geometry by Peihua Dai[26]. The resistivity was plotted as a function of resistivity ratio $\rho(4.2K)/\rho(300K)$, and the Thurber[31] calibration was used to obtain a calibration curve for resistivity ratio versus boron concentration. The estimated errors in $\rho(300K)$ and n for bar-shaped samples were 1%. The advantage of this method is that the resistivity ratio is independent of sample geometry and a more sensitive function of the concentration than the room-temperature resistivity.

Boron concentrations of the seven samples used in the measurements described below were determined by measuring the resistance ratio and using the calibration curve established by Dai. Table II-B lists room-temperature resistivities, resistance ratios $R_{4.2}/R_{300}$, boron concentrations n, and concentration ratios n/n_c (n_c - critical concentration) for all seven samples. The critical concentration n_c = 4.06×10^{18} cm^{-3} for Si:B was determined earlier by Dai et al[32].

Reproduced with permission of the copyright owner. Further reproduction prohibited without permission.

TABLE II-B. Sample designation, room temperature resistivities ρ_{300K}, resistance ratios $R_{4.2K}/R_{300K}$, dopant concentration n, and dopant concentrations n/n_c, relative to zero-field critical concentration, $n_c = 4.06 \times 10^{18}$ cm^{-3}.

sample	$\rho_{300K}(\Omega cm)$	$R_{4.2K}/R_{300K}$	$n(10^{18} cm^{-3})$	n/n_c
A	0.017	2.711	4.11	1.012
B	0.0167	2.466	4.20	1.034
C	0.0165	2.270	4.30	1.059
D	0.0162	2.110	4.38	1.079
E	0.0158	1.833	4.56	1.123
F	0.0154	1.609	4.75	1.170
G	0.015	1.423	4.97	1.224

3. Experimental Setup

The magnetoconductivity of Si:B samples was measured between 0.07 and 0.5K in a Oxford model 75 dilution refrigerator equipped with a 9-T superconducting magnet. The basic principles of dilution refrigeration can be found, for example, in O. V. Lounasma[33] or R. Richardson and E. N. Smith[34].

3.1. Sample Holder

To establish good thermal contact, samples were immersed in the H^3-H^4 mixture inside a glass mixing chamber. For the measurements in high magnetic field (up to 9T) a teflon sample holder was used in-

Reproduced with permission of the copyright owner. Further reproduction prohibited without permission.

stead of a copper one. This avoids heating due to eddy currents. Particular care was taken in mounting the samples onto the sample holder. It was found by P. Dai that the use of low temperature grease or GE varnish for thermal anchoring of the samples to the sample holder changes the character of the samples as the temperature decreases. Due to the pronounced sensitivity of Si:B to stress, the stress applied by the grease as it hardens changes the properties of the samples. Samples were attached to the sample holder using dental floss, oriented perpendicular to the magnetic fields, as shown in Fig. II-1

3.2 Thermometry and Temperature Control

Two RuO_2 thin film thermometers, obtained from Dr. Eric Smith at Cornell University, were used for measuring the temperature: one placed at the top, the other at the bottom of the sample holder. The thermometers were calibrated in zero magnetic field at Cornell and one of the thermometers was calibrated in magnetic field by Dr. Youzhu Zhang at Rutgers University. Temperatures were then determined in a magnetic field by taking the magnetoresistance of the thermometer into account. The advantage of RuO_2 thermometers are their stability, low noise and small magnetoresistance.

A 500Ω heater made of Evenohm wire was placed at the top of the sample holder to obtain uniform heating of the He^3-He^4 mixture. The heater was controlled using a BTI Model 1000 Conductance Bridge/Controller.

Reproduced with permission of the copyright owner. Further reproduction prohibited without permission.

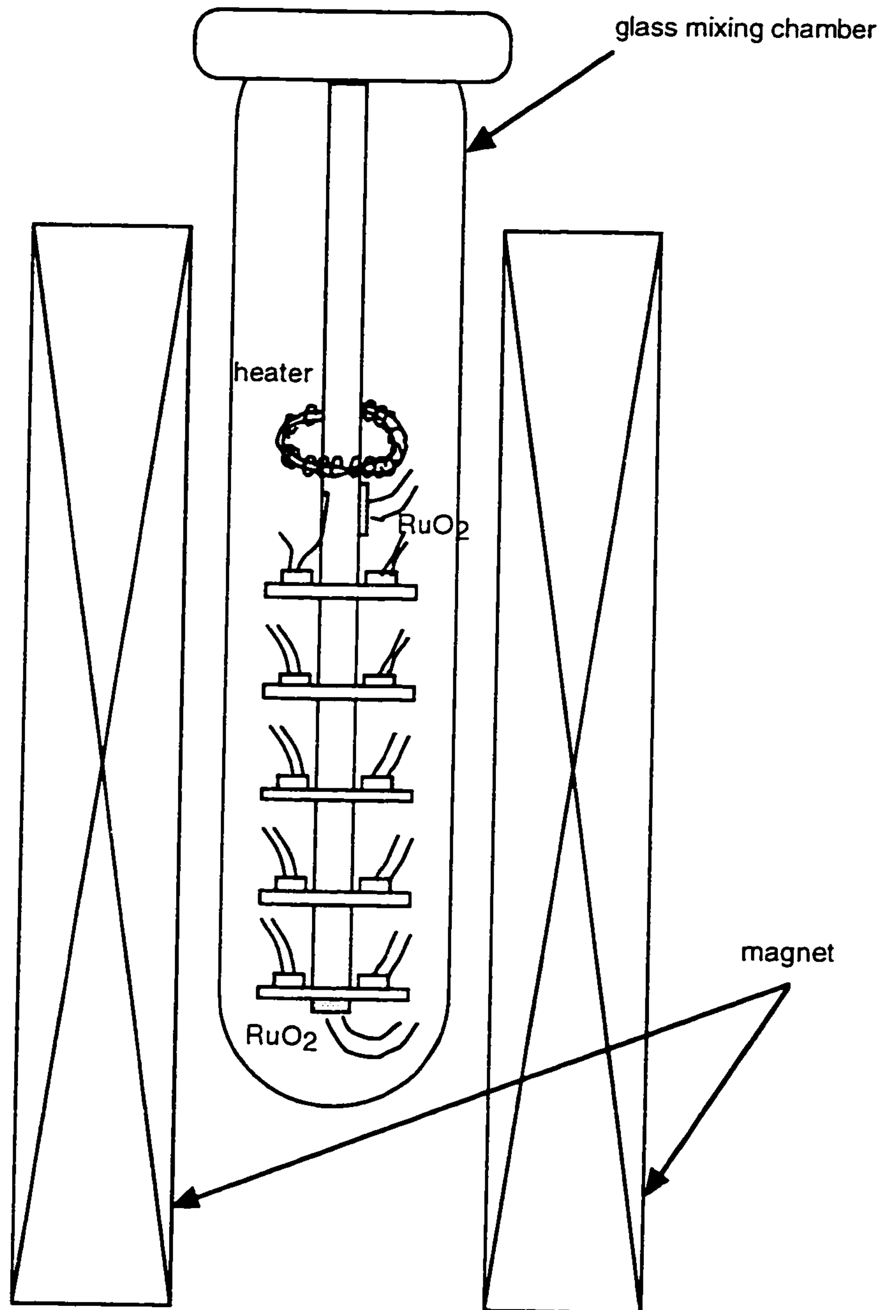

Fig. II-1. The glass mixing chamber with the sample holder, RuO_2 thermoneters, heater, and Si:B samples.

Reproduced with permission of the copyright owner. Further reproduction prohibited without permission.

3.3 Electrical Wiring

Electrical wires connecting samples, heater and thermometers to the measuring instruments were thermally anchored at the 1K pot, at the still (0.6K), at the heat exchangers (0.3K) and at the top of the mixing chamber (0.07K). Heat sinks were made of copper in the shape of a spool, about one inch long. Wires were wound several times around the spool applying GE-varnish for thermal contact, and the spool was thermally anchored with a screw. This prevented heat leaks from outside (room temperature) into the mixing chamber. Superconducting wires were used from the bottom of the 1K pot to the top of the mixing chamber. Since their thermal conduction is very poor at low temperature, this further reduced the heat leaks to the mixing chamber. The wires used inside the mixing chamber were made of copper.

3.4 Superconducting Magnet

The superconducting magnet produced magnetic fields up to 90kOe at 4.2 K, and with the use of a λ fridge it can reach 100kOe. The current provided by a HP model 6260 DC Power Supply was controlled by a Cryomagnetics model 60 Programmer/Monitor. The persistent switch heater was controlled by a Cryomagnetics Model 30 Power Supply.

Reproduced with permission of the copyright owner. Further reproduction prohibited without permission.

3.5 Low AC Resistance Measurements

A standard four terminal low-frequency AC method was used to measure the resistance of the samples. AC methods were used rather than DC to eliminate possible thermal voltages between the contacts.

The resistance was measured with an AVS-46 ac resistance bridge of excitation frequency 15 Hz and minimum excitation voltage of 10μV corresponding to an input power of 10^{-11} W for a 2Ω sample. At the lowest temperatures, the resistance was measured with a Stanford Research Systems model SR850DSP lock-in amplifier. The excitation frequency was 17.5Hz, and the lowest excitation voltage used was 0.1μV. This corresponds to a power level of 10^{-14} W for a 1Ω sample.

3.6 Data Acquisition

The temperature controller, magnetic field controller/monitor, AC resistance bridge and SS lock-in amplifier were interfaced with an Apple Macintosh II computer. A Labview program was written and used to control and record the temperature, magnetic field and sample resistance.

Reproduced with permission of the copyright owner. Further reproduction prohibited without permission.

C. Results and Discussion

The conductivities of seven metallic Si:B samples listed in Table II-B are plotted in Fig. II-2 as a function of the square root of temperature between 70 mK and 500 mK in zero magnetic field. The conductivity below 500 mK is generally fitted by the form

$$\sigma(0,T) = \sigma(0,0) + mT^{\frac{1}{2}}, \qquad \text{(II-C-1.1)}$$

where the second term is due to electron-electron interactions and the slope m is given by:

$$m = \alpha(4/3-3/2\gamma F_{\sigma}), \qquad \text{(II-C-1.2)}$$

(see also equation (I-B-2.1). Good fits were obtained for all samples except for the two closest to the transition. More detailed discussion of the temperature dependence of Si:B in a wide range of temperatures (0.055 - 4.2 K) and concentrations can be found in Physical Review B 45, 3984 (1992) by Dai et al. For concentrations well above the critical (n_c = 4.06×10^{18} cm^{-3})[32] concentration the conductivity increases with decreasing temperature, or $m<0$. For samples very near the transition, however, the conductivity decreases as the temperature is lowered, or $m<0$. A similar change in the sign of the slope m has been observed in other doped semiconductors, including Si:P[35], Si:As[36], Si:P,B[37], Ge:Sb[38], and Ge:Ga[39]. From equation (I-B-2.1) one can see that m depends on γ and F_{σ}. γ can take different values depending on the valley degeneracy (6 in the case of n-type silicon) and the presence or absence of intervalley scattering[13].

Reproduced with permission of the copyright owner. Further reproduction prohibited without permission.

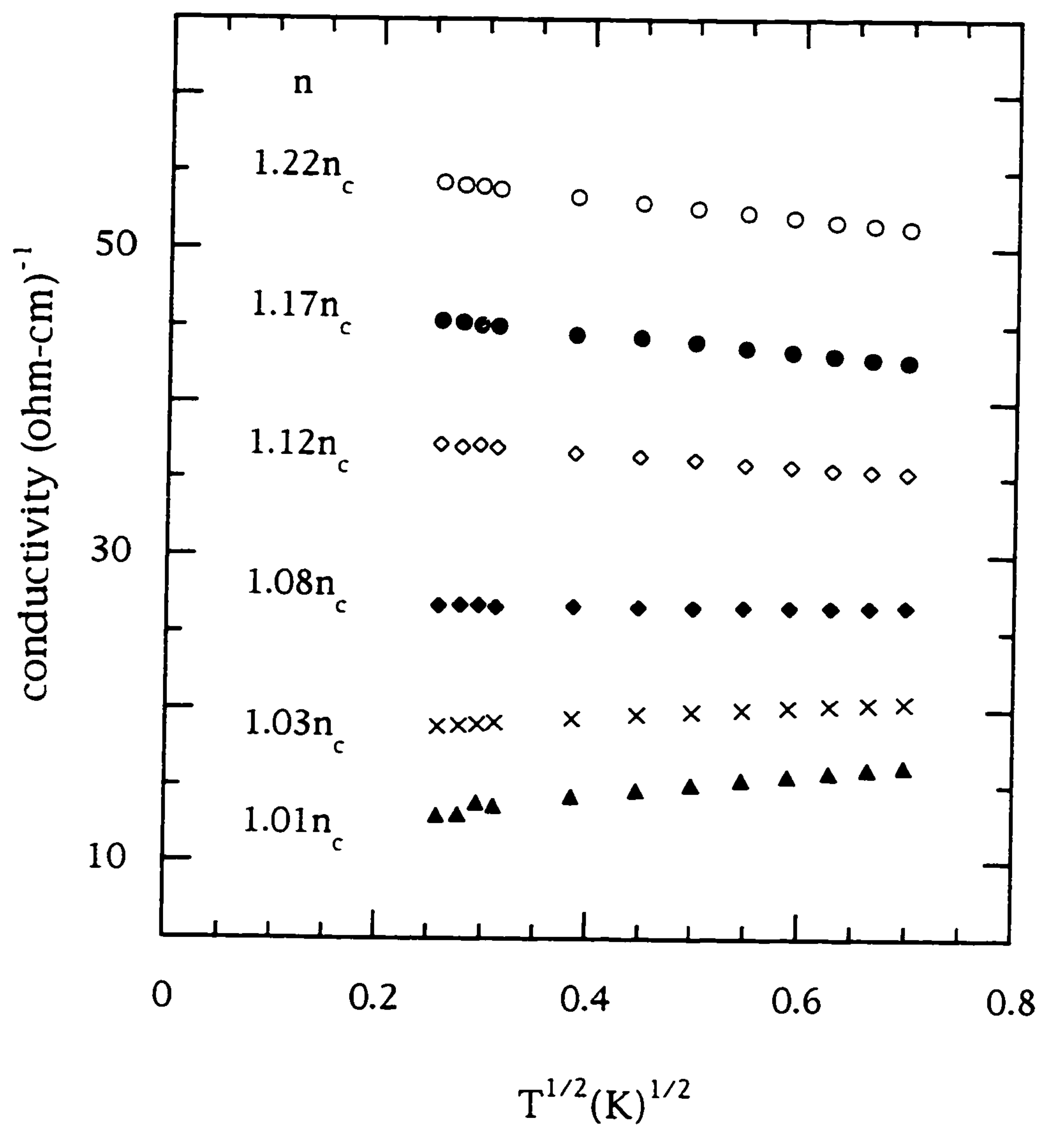

Fig. II-2. Conductivity in zero magnetic field for six metallic Si:B samples plotted as a function of $T^{1/2}$. Dopant concentration n/n_c for each sample is given relative to the zero-field critical concentration $n_c = 4.06 \times 10^{18}\ cm^{-3}$.

Reproduced with permission of the copyright owner. Further reproduction prohibited without permission.

In the case of p-type Si:B, however, the effects of mass anisotropy are negligible and intervalley scattering is absent because of its p-type character. Despite these differences, we note that the behavior as well as the magnitude of m as a function of the concentration is quite similar for n-type and p-type[25]. According to theory[10,12], m can change sign depending on the value of the interaction parameter F_σ. In earlier studies[35,38], the change in sign of m near the transition was attributed to a diverging screening length K^{-1} (see equation (II-C-1.2)) and the consequent vanishing interaction parameter F_σ.

In Fig. II-3 the conductivity of two samples A and G is plotted as a function of the square root of temperature in zero field and 18 fixed magnetic fields from 0.1-8.9 T. The theoretical prediction[8,17] for the temperature dependence of the conductivity in a strong magnetic field such that $g\mu_B H >> k_B T$ is:

$$\sigma(H,T) = \sigma(H,T=0) + m'\sqrt{T} \qquad \text{(II-C-1.3)}$$

where slope m′ is given by:

$$m' = \alpha(4/3 - \gamma F_\sigma/2). \qquad \text{(II-C-1.4)}$$

This is the field-independent exchange + singlet Hartree contribution of equation (II-A-1.1).

For a high-concentration sample such as G ($n = 4.97 \times 10^{18}$ cm^{-3}) that displays a negative slope m in the absence of a magnetic field, the magnetic field changes the slope of the conductivity to positive: the negative slope at high temperatures becomes positive at low temperatures, the maximum occuring when $g\mu_B H \approx k_B T$, where g=1.2 for Si:B.

Reproduced with permission of the copyright owner. Further reproduction prohibited without permission.

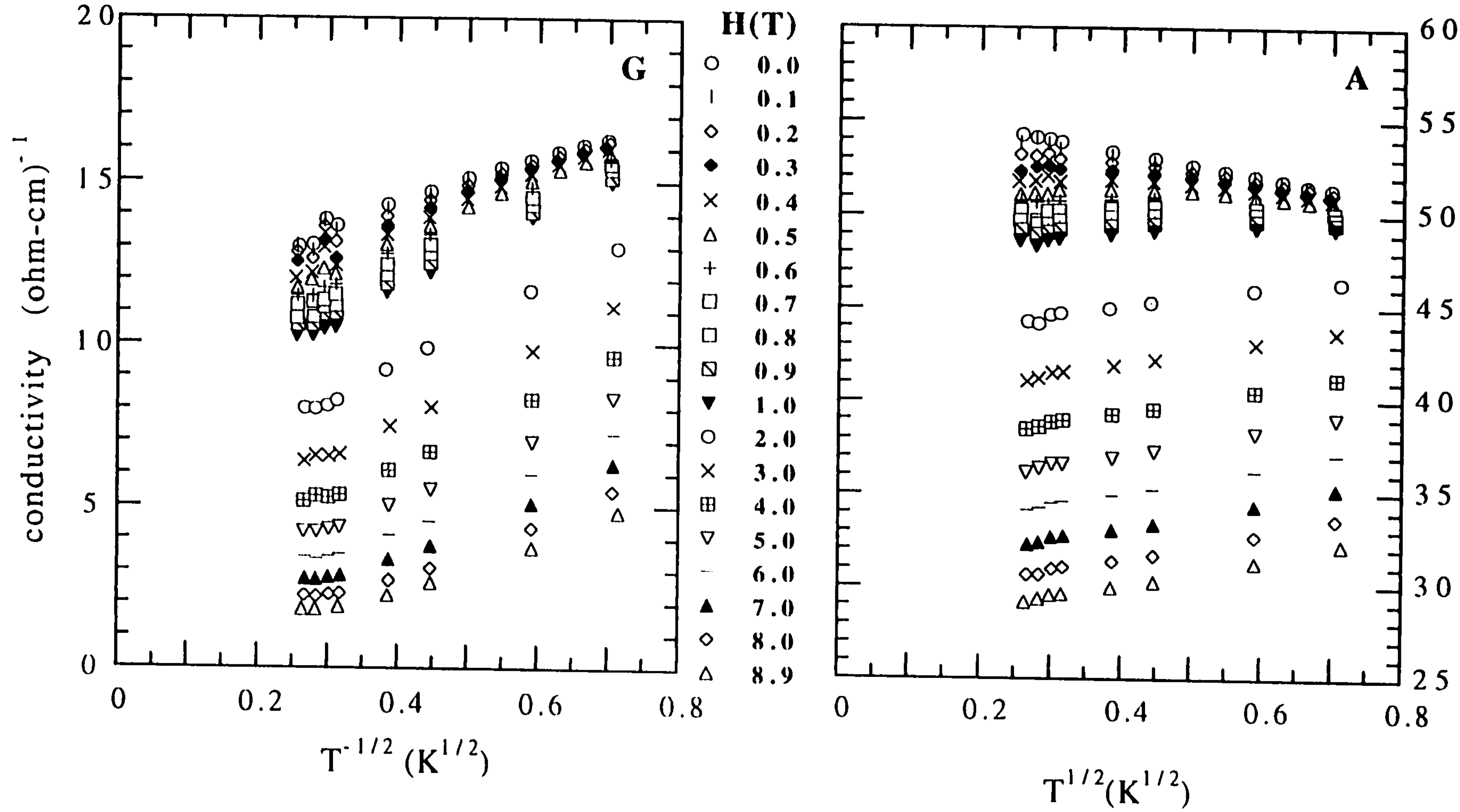

Fig. II-3. Conductivity as a function of $T^{1/2}$ in zero magnetic fields and 18 fixed magnetic fields between 0.1 and 8.9 T as labeled for (a) sample A closest to the metal-insulator transition ($n=4.06 \times 10^{18}$ cm^{-3}); (b) sample G farthest from the transition ($n=4.97 \times 10^{18}$ cm^{-3})

Reproduced with permission of the copyright owner. Further reproduction prohibited without permission.

For magnetic fields of 1T and above, the maximum disappears and the slope is positive in the whole range of temperatures. As mentioned earlier, this negative contribution to the magnetoconductance is attributed to Zeeman splitting in the particle-hole channel of acceptor hole states that becomes the dominant effect at high magnetic fields. A large magnetic field such that $g\mu_B H >> k_B T$ and $g\mu_B H >> h/\tau_{s.o.}$ ($1/\tau_{s.o.}$ is the spin-orbit scattering rate) suppresses the spin dependent triplet channel which is responsible for the negative slope in zero magnetic field. The remaining field-independent channel given by equation (II-A-1.1) gives net positive slope.

For samples closer to the transition which have positive slope in zero field, the curves become steeper with the increasing field, as in sample A ($n=4.11\times10^{18}$ cm^{-3}). Sample A is just 1% above the critical concentration ($n_c=4.06\times10^{18}$ cm^{-3}) for the metal-insulator transition; in agreement with earlier results[26] this sample enters the insulating phase at high magnetic fields. This is evidenced here by negative zero-temperature intercepts and a distinct flattening below about 100mK. Data at H=5T and higher were therefore not included in the scaling analysis for this sample presented below. For the same reason, data at 8T and above were omitted for sample B.

Fig. II-4 shows the conductivity of sample G as a function of magnetic field at several different temperatures. As expected, the magnetoconductivity of p-type Si:B is negative for both high and low magnetic fields. All seven samples show negative magnetoconductance in the measured range of temperatures and magnetic fields. The presence of spin-orbit scattering contributes to a negative

Reproduced with permission of the copyright owner. Further reproduction prohibited without permission.

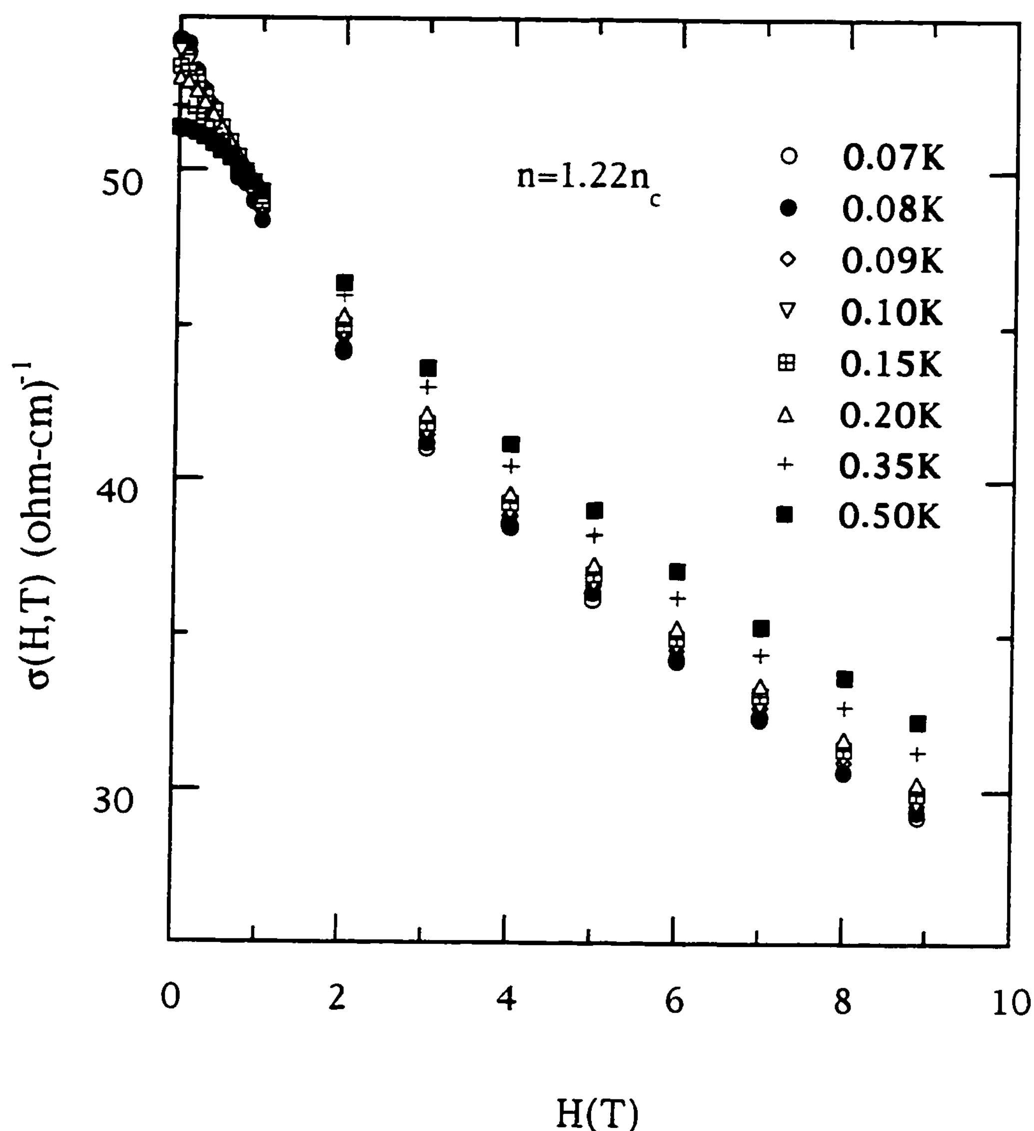

Fig. II-4. Conductivity as a function of magnetic field at eight different temperatures, as shown, for a Si:B sample with dopant concentration $n=1.22\ n_c$.

antilocalization term at low fields, making it very difficult to separate contributions deriving from localization and electron-electron interactions.

Reproduced with permission of the copyright owner. Further reproduction prohibited without permission.

Earlier experiments on the magnetoconductance of Si:P[24] and Si:B[26] indicated the importance of electron-electron interactions near the transition. An attempt was made to separate the contributions from localization and interactions data by plotting the data following the functional form expected for electron-electron interactions (see equation (II-A-1.4). Fig. II-5 is a plot of $\Delta\sigma_I/T^{1/2}$ as a function of H/T for all seven samples. Surprisingly, the data for each sample in all the magnetic fields up to 9T and temperatures between 0.07 and 0.5K collapse onto a single universal curve. The shape of the curve essentially does not vary with the concentration, but the amplitude of the curve is reduced as the concentration is decreased toward the critical concentration. Appropriate multiplicative factors applied to each curve results in superposition onto a single curve, as demonstrated in Fig. II-6. The prefactor $K= 0.77\alpha\gamma F_\sigma$ is plotted as a function of dopant concentration in the inset of Fig. II-6. It decreases as the critical concentration is approached, indicating the decrease of the interaction strength F_σ. Similar behavior of the interaction strength in Si:B was deduced from the slope m of equation equation (II-C-1.2). and slope m' of equation (II-C-1.4) by Dai et al[26].

Collapse of the data onto a single universal curve suggests that the magnetoconductance is strongly dominated by electron-electron interactions. Note that at low fields, localization is expected to contribute a term $\Delta\sigma_L(H,T) \propto H^{1/2}f_3(DH/T^p)$ (see equation (II-A-2.1)), where the diffusion constant D is expected to decrease rapidly as the transition is approached. The Cooper (particle-particle) channel of interacting electrons given by equation (II-A-1.5) contributes a term: $\Delta\sigma_L(H,T) \propto -H^{1/2}f_3(HD/T)$.

Reproduced with permission of the copyright owner. Further reproduction prohibited without permission.

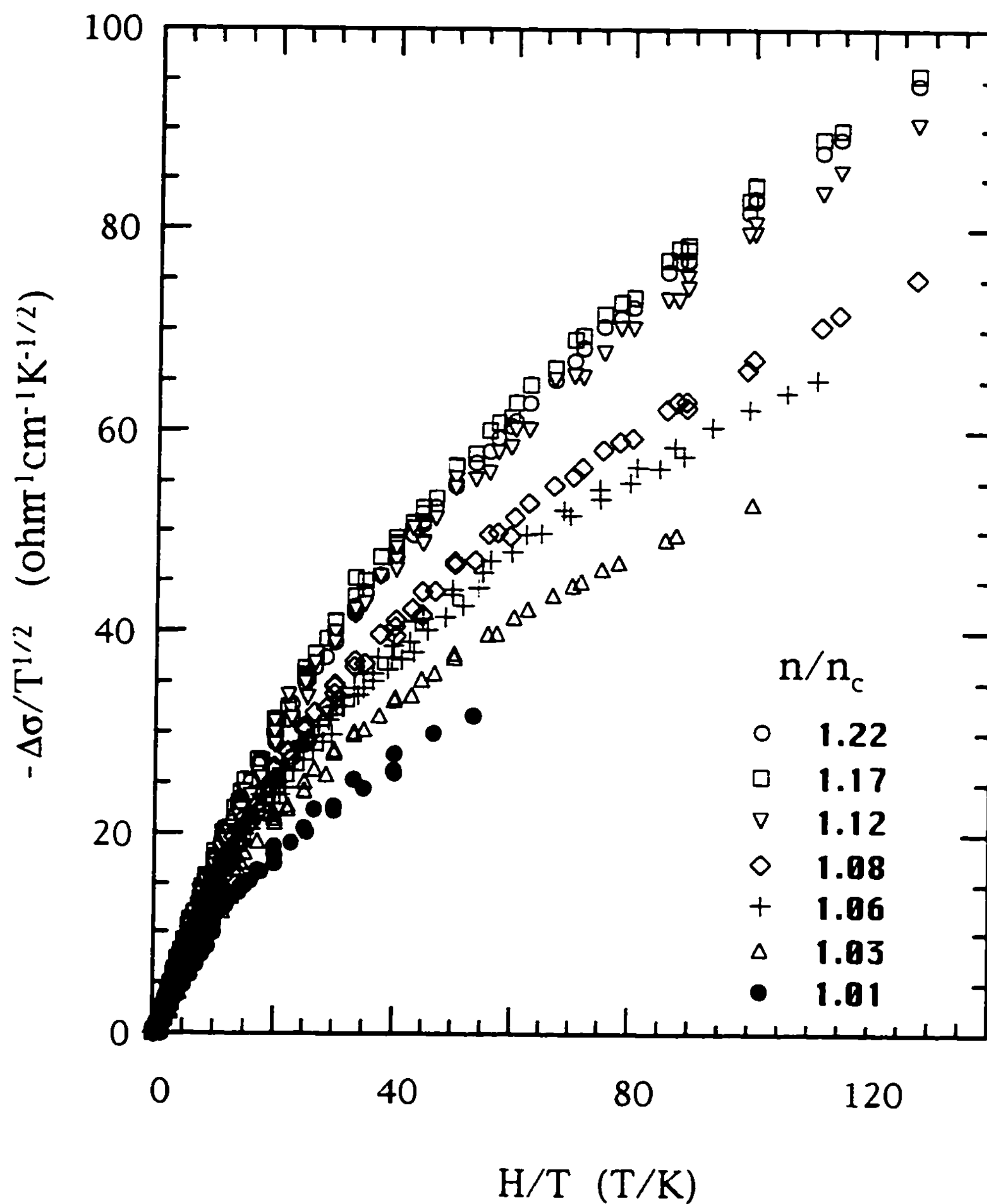

Fig. II-5. $-\Delta\sigma/T^{1/2}$ versus H/T for samples A through G, as labeled.

Reproduced with permission of the copyright owner. Further reproduction prohibited without permission.

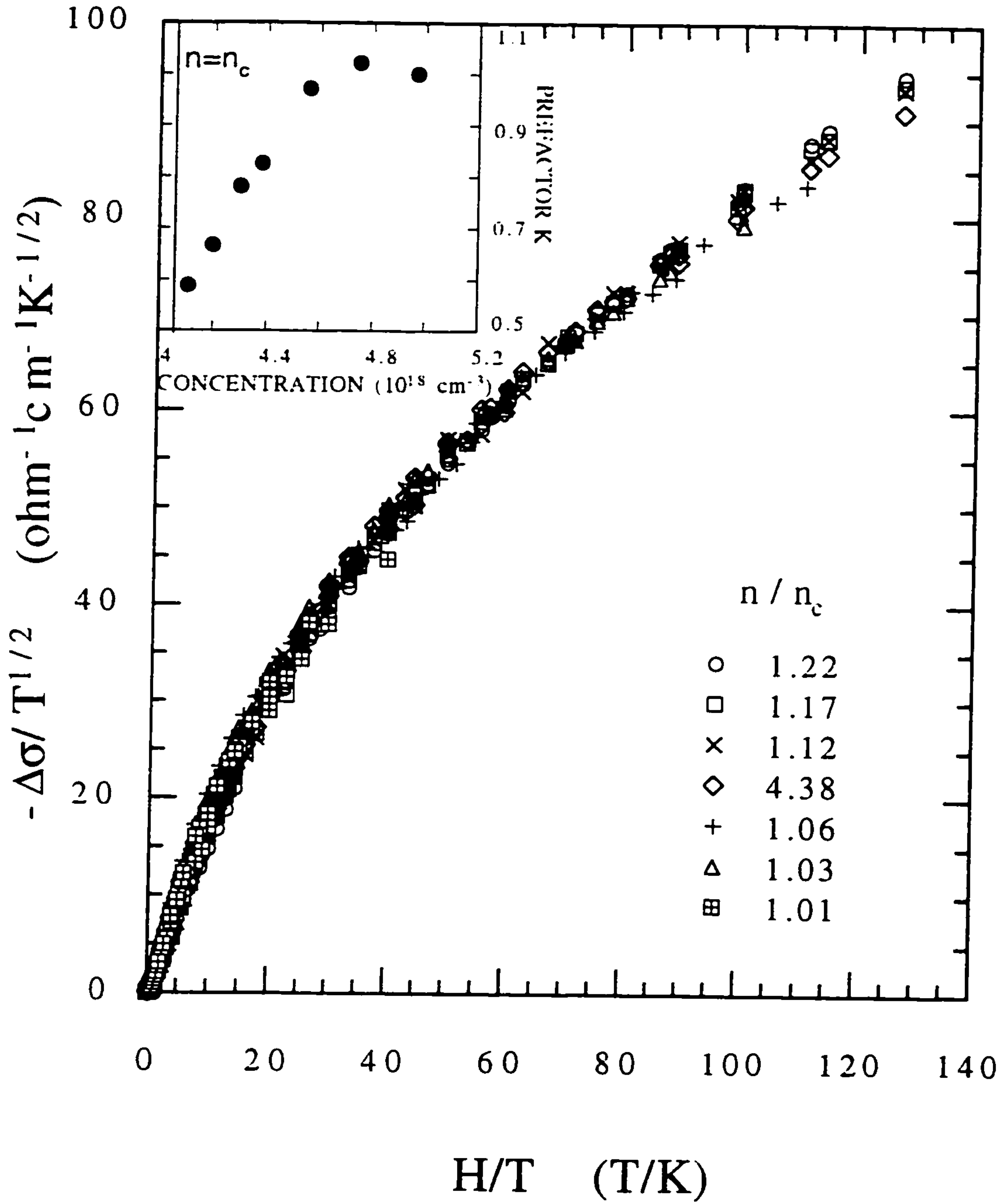

Fig. II-6. [$-\Delta\sigma/T^{1/2}/K$] versus H/T for samples A through G, where K is a constant chosen to shift each curve relative to sample G. The inset shows the prefactor K as a function of dopant concentration; the vertical line denotes the critical concentration $n_c=4.06\times10^{18}$ cm^{-3}.

Reproduced with permission of the copyright owner. Further reproduction prohibited without permission.

The presence of D in the argument of the f_3 function would introduce a different shift for each sample on the x axis of a log-log plot; therefore both terms must play negligible role. Another important implication is that the H/T scaling implies the absence of spin-orbit and spin-flip scattering. If either scattering mechanism were present, one would have to replace the argument of $g_3(g\mu_B BH/k_B T)$ function with $(g\mu_B BH + \hbar/\tau_s)/k_B T$, where τ_s is the characteristic scattering time. This would weaken the field dependence and also violate H/T scaling. Despite the large spin-orbit coupling that characterizes the valence band of p-type Si:B, we see no effects associated with spin-orbit scattering in the range of temperatures and magnetic fields of our experiments.

However, detailed comparison of the form of the experimental function shown in Fig. II-7 with the theory of electron-electron interactions of Lee and Ramakrishnan (dashed line) shows obvious inconsistencies. The dashed curve in Fig. II-7 was obtained by numerical integration of the function g_3 of equation (II-A-1.2) using a g value of 1.2 characteristic of p-type Si:B. A different choice of g factor simply shifts the theoretical curve along the x axis and therefore cannot yield agreement with the experimental curve. It was noted by V. Dobrosavljevic that this discrepancy arises from the limitations of the above theory, which is derived for spin-1/2 particles in the absence of spin-orbit coupling. P-type semiconductors like Si:B have strong-spin-orbit coupling due to the nature of their valence band, and the acceptor states are characterized by total angular momentum J=3/2 rather than 1/2. It was shown by Dobrosavljevic at al.[40] that the angular momentum of holes does not change in transport processes at these relatively low acceptor concentrations.

Reproduced with permission of the copyright owner. Further reproduction prohibited without permission.

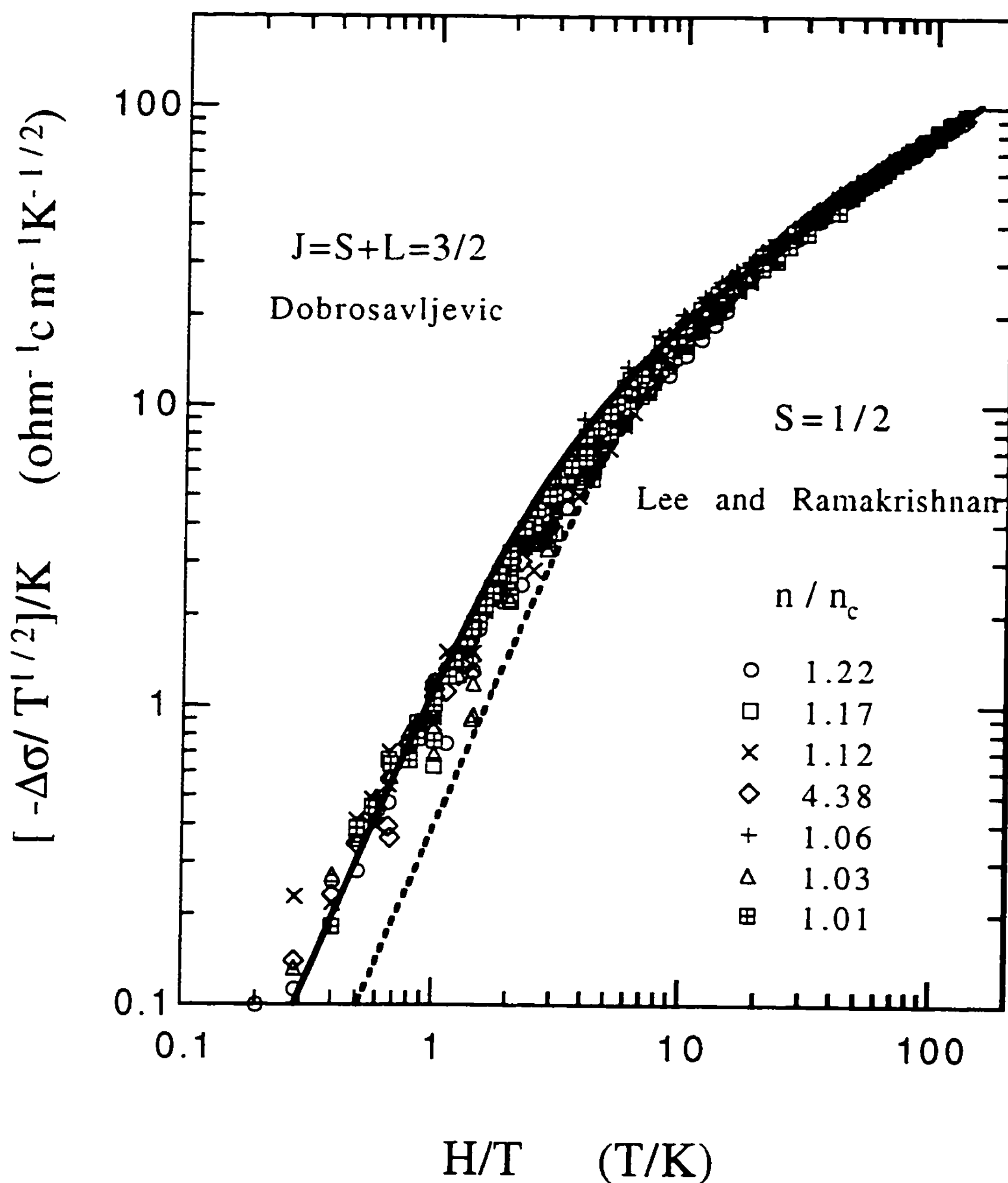

Fig. II-7. $[-\Delta\sigma/T^{1/2}]/K$ versus H/T for samples A through G on a log-log plot. The theoretical function $g_3(g\mu_B H/k_B T)$ of equation II-A-1.2 is shown for j=1/2 and j=3/2 by the dashed and solid lines, respectively.

Reproduced with permission of the copyright owner. Further reproduction prohibited without permission.

This can explain the absence of spin-orbit scattering in the presence of strong spin-orbit coupling.

Taking this into account, one can generalize[40] the standard theory for interactions[8] to the case of J=3/2. The general form of the equation (II-A-1.4) remains the same, but the scaling function $g_3(h)$ is replaced by

$$g'(h) = a_1 g_3(h) + a_2\, g_3(2h) + a_3 g_3(3h) \qquad \text{(II-C-1.5)}$$

where a_1, a_2, and a_3 are parameters related to the interaction amplitudes in the three magnetic interaction channels. Since the total angular momentum of the particle and hole is conserved $J = J_1 + J_2$, the corresponding three magnetic channels have $M_J = \pm 1, \pm 2, \pm 3$. With the simplest assumption that $a_1 = a_2 = a_3$, the new function yields an excellent fit to the experimental data, shown by the solid line in Fig. II-7. A better fit can be obtained by allowing independent variation of the three parameters of equation (II-C-1.5).

Reproduced with permission of the copyright owner. Further reproduction prohibited without permission.

CHAPTER III

STRESS-INDUCED METAL-INSULATOR TRANSITION IN Si:B

A. Metal-Insulator Transition-Scaling Theory

The metal-insulator transition in doped semiconductors is generally believed to be a continuous quantum phase transition. From the point of view of general scaling theory of phase transitions, one expects certain physical quantities such as the conductivity, density of states, specific heat, etc., to scale as a function of temperature (frequency), magnetic field, concentration, stress or some other parameter near the critical point[41].

1. Dynamical Scaling Law

The electrical conductivity is expected to scale as a function of temperature T and the parameter δt in the following form:

$$\sigma(n.T) = AT^{\frac{\mu}{z\nu}} f\left(\frac{\delta t}{T^{1/z\nu}}\right), \qquad \text{(III-A-1.1)}$$

Reproduced with permission of the copyright owner. Further reproduction prohibited without permission.

Here $\delta t = t - t_c$, where t is the parameter that drives the transition (such as concentration, stress or magnetic field), A is a constant and μ, z, and ν are the critical conductivity exponent, the dynamical exponent and the correlation length exponent, respectively. The temperature dependence of the conductivity at the critical point t_c is given by $\sigma_c(t_c,T) = AT^{\mu/z\nu}$. At zero temperature equation (III-A-1.1) reduces to:

$$\sigma(t,T \rightarrow 0) \propto \delta t^{\mu} \qquad \text{(III-A-1.2)}$$

and describes the critical behavior of the zero-temperature conductivity consistent with (I-A-1).

For a noninteracting gas of electrons, there is only one relevant length in the problem, namely the correlation length ξ. Since conductivity has dimensions of a length to the power (2-d) and d is the dimension of the system, the critical conductivity $\sigma(T=0) \sim 1/\xi^{d-2}$. The correlation length ξ is expected to diverge at the transition as $\xi \sim \delta t^{-\nu}$ which implies:

$$\mu = (d-2)\nu \qquad \text{(III-A-1.3)}$$

or $\mu = \nu$ for $d = 3$ in the critical region. This is referred to as Wegner's law. From general theoretical arguments for phase transitions in random systems, Chayes et al.[42] calculated a bound on the correlation length exponent:

Reproduced with permission of the copyright owner. Further reproduction prohibited without permission.

$$\nu \geq 2/d, \qquad \text{(III-A-1.4)}$$

For $\mu = \nu$ this gives $\mu \geq 2/3$ in three dimensions. This inequality is expected to hold at all metal-insulator transitions and it is generally valid unless either the dimensionless disorder vanishes at the transition or there are multiple divergent lengths at the transition.

For a metal-insulator transition in an interacting gas of electrons there are three different time scales[43] : $\tau \propto \xi^{z_1}$, $\tau \propto \xi^{z_2}$, $\tau \propto \xi^{z_3}$, that diverge with different dynamical scaling exponents z_1, z_2 , and z_3. The scaling law defined by equation (III-A-1.1) is not known in this case and Wegner's law (III-A-1.3) is not valid.

If the scaling law (III-A-1.1) is valid, it is also expected to hold on the insulating side of the transition and should have the form given by hopping conduction :

$$\sigma(t,T) \propto e^{-(\frac{T_0}{T})^x} \qquad \text{(III-A-1.5)}$$

where $x = 1/4$ for Mott variable range hopping or $x = 1/2$ for Efros-Shklovskii hopping[44]. T_0 for ES hopping is given by:

$$T_0 \propto \frac{e^2}{\kappa\xi}, \qquad \text{(III-A-1.6)}$$

where κ is dielectric constant and ξ is localization length. Both κ and ξ behave critically as t approaches t_c from the insulating side: $\kappa \propto \delta t^{-\zeta}$ and $\xi \propto \delta t^{-\nu}$ so that T_0 becomes:

Reproduced with permission of the copyright owner. Further reproduction prohibited without permission.

$$T_0 \propto \delta t^{\alpha}, \qquad \text{(III-A-1.7)}$$

where $\alpha = \zeta + \nu$.

For Mott variable range hopping T_0 has the following form:

$$T_0 = \frac{\beta}{k_B N(E_F)\xi^3}, \qquad \text{(III-A-1.8)}$$

where β is a numerical coefficient, ξ is the localization radius and $N(E_F)$ is the density of states at the Fermi level. Since density of states $N(E_F)$ does not diverge, here

$$T_0 \propto \frac{1}{\xi^3} \propto \delta t^{3\nu} \qquad \text{(III-A-1.9)}$$

1.1 Critical Conductivity Exponents-Universality Classes

Based on theoretical work of Finkelshtein[45] and Castellani et al.[46] critical behavior near the transition is determined by symmetry breaking processes such as spin-orbit scattering, spin-flip scattering or magnetic field. Each of the symmetry breaking mechanisms defines a different universality class. Theoretically, a critical conductivity exponent $\mu=1$ is expected for the magnetic field universality class (MF), and in presence of magnetic impurities (MI) and spin-orbit scattering (SO). Note that these results were obtained for $2+\varepsilon$ expansion where $\varepsilon \ll 1$. In 3 dimensions $\varepsilon = 1$, so that the above results can not be taken rigorously. For the generic universality class

Reproduced with permission of the copyright owner. Further reproduction prohibited without permission.

(G), where all of the above symmetry breaking mechanisms are absent, the critical conductivity exponent has not been calculated. Experimentally, $\mu \approx 1$ was found for compensated semiconductors and amorphous alloys, while $\mu \approx 1/2$ was found for a large number of uncompensated semiconductors. The following table (Table III-A) lists the results for systems studied by various experimental groups. All of these were obtained by varying the dopant concentration n, except for the first entry for Si:P which was obtained by varying uniaxial stress (ref. 3.).

Table III-A. List of uncompensated and compensated doped semiconductors, corresponding references and values of critical conductivity exponents.

Uncompen Systems	Reference	μ
Si:P	3	0.55±0.1
Si:P	47	1.3
Si:As	48	0.60±0.05
Si:Sb	49	0.49±0.09
Si:(P,As)	50	0.7±0.2
Si:B	32	0.65±0.05
Ge:As	51	0.5
Ge:Sb	52	0.9
Ge:Ga	39	0.502±0.025

Reproduced with permission of the copyright owner. Further reproduction prohibited without permission.

Compens. Systems	**Reference**	μ
Ge:Sb	53	1
Si:(P,B)	54	0.9±0.08
Ge: (Ga,As)	55	1
Ga:As	56	1

Note that uncompensated p-type Si:B and Ge:Ga due to their degenerate valence band are expected to have strong spin-orbit scattering and consequently should belong to a **SO** universality class with $\mu = 1$. Nevertheless experimental findings for μ are closer to 1/2 than 1.

Reproduced with permission of the copyright owner. Further reproduction prohibited without permission.

2. Stress Induced Metal-Insulator Transition

A doped semiconductor is an example of a disordered system where the metal-insulator transition can be tuned by the application of uniaxial stress. The shallow impurity bands (energies of the order of ~meV compared to the gap energies ~1eV) strongly couple to the stress[57] and allow one to study the metal-insulator transition in a single sample of dopant concentration n as the critical concentration n_c is tuned through n.

2.1 Effective Mass Approximation

Small impurity binding energies (~ meV) are the consequence of the large dielectric constant of the host material (κ=11.4 for Si and κ=15.4 for Ge)[58]. Impurity wave functions extend over many lattice sites with the Bohr radii a_B of the order of 10-100Å (see Fig. III-1a). Whether a given impurity is a donor or an acceptor is determined by its position in the periodic table. In common Group IV semiconductors like Ge and Si donor impurities are from Group V (P, Sb, As). The elements of Group V have five valence electrons; four will form covalent bonds with four valence electrons of Ge or Si, and the extra electron becomes a donor. Elements from Group III (B, Al, Ga and In) are acceptors since they lack one electron. The proximity of a donor (acceptor) level to the bottom (top) of the conduction (valence) band (see Fig. III-1b) implies that an excess electron (hole) is weakly bound to the impurity center, and located far from it.

Reproduced with permission of the copyright owner. Further reproduction prohibited without permission.

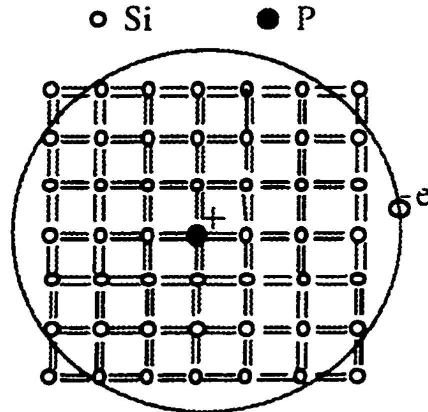

Fig. III-1a. Phosphorus atom makes four covalent bonds with nearby silicon atoms, leaving one extra electron that is available for conduction.

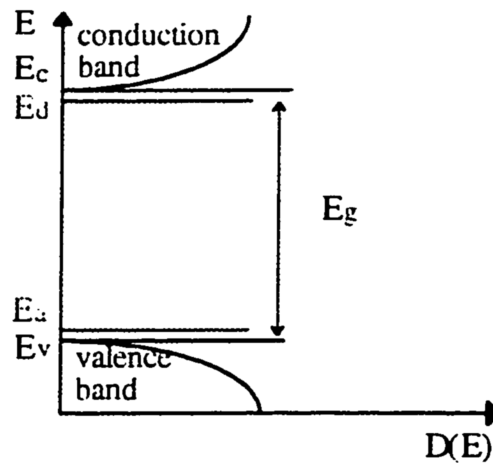

Fig. III-1b. Donors form an impurity band E_d near the bottom of the conduction band E_c, where E_c-E_d ~ 45 meV in Si. Similarly, acceptors form a band E_a-E_v ~ 45 meV above the valence band. Energy of the gap E_g=E_c-E_v ~ 1eV.

Reproduced with permission of the copyright owner. Further reproduction prohibited without permission.

One can therefore regard the impurity center as a point charge and assume its potential to be[59]:

$$U(r)=-e^2/\kappa r \qquad \text{(III-A-2.1.1)}$$

where e is the electron charge, r the distance from the center and κ the dielectric constant of the lattice. This is the basic premise of the Effective Mass Approximation EMA, and is only valid far from the impurity center.

For an ideal lattice, one can write a single electron Hamiltonian of the following form[60]:

$$H_0 = -\frac{\hbar^2}{2m_0}\Delta + V(\vec{r}) \qquad \text{(III-A-2.1.2)}$$

where m_0 is the free-electron mass, Δ is the Laplace operator and V(r) is the periodic potential of the lattice. The solution to the Schrödinger equation with the above Hamiltonian is given by the Bloch functions:

$$\phi_{n,\vec{k}} = \frac{1}{V_0^{1/2}} u_{n,\vec{k}} e^{i\vec{k}\cdot\vec{r}} \qquad \text{(III-A-2.1.3)}$$

where V_0 is a normalization volume, $u_{n,\mathbf{k}}$ is a periodic function with the period of lattice, **k** is the wave vector and n is the band index. If one restricts the wave vector to the first Brillouin zone and assumes that the eigenvalues $E_n(\mathbf{k})$ of Hamiltonian (III-A-2.1.2) are known within the zone then solutions of the EMA equation[61]

$$(H_0 - e^2/\kappa r)\Psi = E\,\Psi \qquad \text{(III-A-2.1.4)}$$

Reproduced with permission of the copyright owner. Further reproduction prohibited without permission.

should be of the form

$$\psi = \sum_{n',\vec{k}'} B_{n'}(\vec{k}')\phi_{n',\vec{k}'}(\vec{r}) . \qquad \text{(III-A-2.1.5)}$$

Substituting (III-A-2.1.5) into (III-A-2.1.4), taking into account normalization of the Bloch wave functions, one arrives at:

$$\left[E_n(\vec{k}) - E\right]B_n(\vec{k}) + \sum_{n',\vec{k}'} U^{n,\vec{k}}_{n',\vec{k}'} B_{n'}(\vec{k}') = 0 . \qquad \text{(III-A-2.1.6)}$$

For the nondegenerate extrema in the center of the Brillouin Zone the minimum of $E_n(\mathbf{k})$ occurs at $\mathbf{k}$=0, so for small values of $\mathbf{k}$ one can write $E_n(\mathbf{k})=\hbar k^2/2m$, where m is the effective mass. It is plausible to assume that $B_n(\mathbf{k})$ is nonvanishing only near the center of the Brillouin Zone at k=0 and $u_{n,\mathbf{k}} \approx u_{n,0}$ for small k, so that equation (III-A-2.1.6) will take the form:

$$[\frac{\hbar^2 k^2}{2m} - E]B_n(\vec{k}) - \frac{4\pi e^2}{\kappa V_0}\sum_{\vec{k}'}\frac{1}{(\vec{k} - \vec{k}')^2}B_n(\vec{k}') \qquad \text{(III-A-2.1.7)}$$

where the summation over $\mathbf{k}'$ runs only over the k vectors within the first Brillouin Zone. Since $B_n(k)$ is vanishingly small outside the neighborhood of k=0 one can easily extend this summation to infinity. This allows the change of the coordinate representation of the wave function

$$F(\vec{r}) = \frac{1}{V_0^{1/2}}\sum_{\vec{k}} B_n(\vec{k})e^{i\vec{k}\cdot r} \qquad \text{(III-A-2.1.8)}$$

Reproduced with permission of the copyright owner. Further reproduction prohibited without permission.

where the summation is over all **k**. Substitution of (III-A-2.1.8) into (III-A-2.1.7) gives equation:

$$[-\frac{\hbar^2}{2m}\Delta - \frac{e^2}{\kappa \bar{r}}]F(\bar{r}) = EF(\bar{r}) \qquad \text{(III-A-2.1.9)}$$

that looks like the Schrödinger equation for a hydrogen atom, with an effective mass m and dielectric constant κ. The spectrum of the bound states is given by

$$E_l = -\frac{1}{l^2}\frac{e^4 m}{2\kappa^2\hbar^2}\ , \ l = 1,\ 2,\ \ldots \qquad \text{(III-A-2.1.10)}$$

and the ground state-wave function is of the form

$$F(r) = (\pi a^3)^{-\frac{1}{2}} e^{-r/a_B}, \qquad \text{(III-A-2.1.11)}$$

where $a_B = \hbar\kappa/me^2$ is an effective Bohr radius and is the characteristic dimension of the impurity wave function. The full wave function of the impurity center becomes

$$\Psi(\mathbf{r}) = u_{n,0}\, F(\mathbf{r}) \qquad \text{(II-2.1.12)}$$

which is basically the Bloch wave $u_{n,0}$ at the extremum of the band modulated by large-scale hydrogen like function $F(\mathbf{r})$.

In semiconductors like Ge and Si the conduction band has several minima located at equivalent points of the Brillouin zone. The conduction band of Si has six equivalent minima located at $k_i^0 = 0.85(2\pi/a_0)$ along [100]directions, where a_0 is a lattice constant. The constant energy surfaces are ellipsoids of revolution around [100].

Reproduced with permission of the copyright owner. Further reproduction prohibited without permission.

Along the z-axis the energy surface near [100] extrema has the following form[62]:

$$E = \frac{\hbar^2}{2m_l}(k_z - k_z^0)^2 + \frac{\hbar^2}{2m_t}(k_x^2 + k_y^2). \qquad \text{(III-A-2.1.13)}$$

The longitudinal effective mass of Si is $m_l = 0.916\ m_0$ and the transverse mass is $m_t = 0.19\ m_0$. The extrema of the conduction band of Ge lie exactly on the Brillouin zone boundary along the cube's body diagonals. Each extremum is shared by two zones, so that the number of extrema equals half the number of equivalent directions, which is four. The constant energy surfaces are ellipsoids of revolution around the (111) axis with effective masses $m_l = 1.58 m_0$ and $m_t = 0.08\ m_0$. In complete analogy with (II-2.1.12) the solution of (II-2.1.4) near the extremum at $\mathbf{k} = \mathbf{k}_j$ has the form

$$\chi_j(\mathbf{r}) = F_j(\mathbf{r})\ \phi_j(\mathbf{r}), \qquad \text{(III-A-2.1.14)}$$

where ϕ_j is the Bloch wave at $\mathbf{k} = \mathbf{k}_j$, and F_j is the envelope function satisfying the EM equation

$$[E_j(-i\bar{\nabla}) - \frac{e^2}{\kappa\bar{r}}]F_j(\bar{r}) = EF_j(\bar{r}) \qquad \text{(III-A-2.1.15)}$$

where $E_j(\mathbf{k})$ is the conduction band energy in the vicinity of $\mathbf{k}_j$. The eigenvalues E are the same for all equivalent minima. This equation was solved successfully by Kohn and Luttinger[63] by variational methods. The trial function was chosen in the form

Reproduced with permission of the copyright owner. Further reproduction prohibited without permission.

$$F = (\pi a_\perp^2 a_\parallel)^{-\frac{1}{2}} \exp\{-[\frac{(x^2+y^2)}{a_\perp^2} + \frac{z^2}{a_\parallel^2}]^{1/2}\} \qquad \text{(III-A-2.1.16)}$$

and the parameters $a_\perp$ and $a_\parallel$ were found by minimizing the energy. It was found that the EMA approximation gives very good estimates of excited states; however, it seriously underestimates the energies of the ground states of silicon and germanium. In reality, the six-fold degeneracy of the Si ground state and the four-fold degeneracy of the Ge ground state are partially lifted by the short range potential representing corrections to the EMA. Very near the impurity, the potential is not spherically symmetric; instead, local symmetry is broken by the change of the angle and the length of the tetrahedral covalent bonds between the impurity and nearby host atoms. The addition of the short-range potential to equation (III-A-2.1.4) produces matrix elements in (III-A-2.1.6) that connect the wave functions belonging to different extrema. This leads to the so called valley-orbit splitting of the ground state and a shift in the energy levels usually referred to as a chemical shift. The form of the splitting can be predicted on the basis of symmetry alone, without detailed knowledge of the short-range potential. The correct donor wave functions are linear combinations of the form

$$\phi^i = \sum_{j=1}^{N} \alpha_j^i \chi_j \, , \; i = 1, \ldots N. \qquad \text{(III-A-2.1.17)}$$

The exact form of the splitting, as well as the coefficients α_j^i for Ge and Si are determined from the symmetry properties of the tetrahedral group T_d. The six-fold degenerate ground state of Si splits into one

Reproduced with permission of the copyright owner. Further reproduction prohibited without permission.

singlet, one doublet, and one triplet, while the four-fold degenerate ground state of Ge splits into one singlet and one triplet. Calculations of the acceptor wave functions near the degenerate maximum of the valence band will be given in sections 3.3.

2.2 Effect of Stress on the Impurity Wave Function-MIT

Even a modest stress can induce large changes in Bohr radii affecting the overlap of the neighboring impurity wave functions which in turn effectively shifts the value of n_c defined by the Mott relation[64]

$$n_c^{1/3} a_B \approx 0.25 \qquad \text{(III-A-2.2.1)}$$

This relation was derived from the condition that at the critical point for the Mott-Hubbard transition,

$$U = 2zI, \qquad \text{(III-A-2.2.2)}$$

where $U = (5/8)(e^2/a_B)$ is the Coulomb energy of repulsion between two electrons on the same impurity and 2zI is the bandwidth of the Hubbard band, z is the coordination number and I is an overlap integral between neighboring impurity atoms. If one defines R as an average distance between impurity atoms, then for large values of R or $R/a_B \sim 4$, the overlap integral obtained for s-states is $I \sim 10(e^2/a_B)\exp(-R/a_B)$. Taking $z = 6$ in equation (III-A-2.2.2) gives $R/a_B \cong 5$ and since $R = n^{1/3}$ one arrives at the Mott criterion (III-A-2.2.1).

Reproduced with permission of the copyright owner. Further reproduction prohibited without permission.

Theoretical calculations related to the change of n_c with stress, have beeen done only for n type Ge[65] and Si[66]. Particularly striking are the results for Ge:Sb, where n_c increases by a factor of ≈ 2.2 for a rather modest compressional stress of ~1 kbar along the [111] direction. Unstressed Ge:Sb has a four-fold degenerate donor ground state (due to the degeneracy of the four valleys), so that electrons are distributed over four donor envelope wave functions to maximize their transfer integral (maximum overlap among the wave functions) and lower their energy. Such a big response of Ge:Sb to stress is related to the lifting of the degeneracy of the ground state (shifting the [111] valley down in energy and the remaining three up) and the redistribution of electrons among the different donor wave functions. Accordingly, H. Fritzsche[67] found that the longitudinal resistance measured along the direction of the stress [111] increases rapidly with the stress. At very large stresses all electrons are transferred to the state related to the lower valley, any further variation with stress is small and this is reflected by saturation of the longitudinal piezoresistance. The limiting form of the ground state wave function at large stress is pancake-shaped with the axis of rotation along [111]. The extent of the wave function along the [111] direction is therefore greatly reduced, as is the overlap of the neighboring donor wave functions. The overlap in the direction perpendicular to [111] is still close to its zero stress value, but the carriers in this plane hardly contribute to the current along [111].

In Ge:As approximately the same stress changes n_c only by 20%. In contrast to Ge:Sb, Ge:As has a large central cell potential that has already removed the four-fold degeneracy of the ground state without stress. Valley-orbit splitting between the ground-state and the

Reproduced with permission of the copyright owner. Further reproduction prohibited without permission.

three-fold excited state is $4\Delta = 4.15$ meV. Because of this, the ground-state orbit of As is about 17% smaller than its effective-mass value[57]. Application of stress increases the ground-state radius and mixes the ground state wave function with the more extended valley-orbit split excited states, leading to more overlap along the direction of the stress. Piezoresistance measurement of Ge:As[67] at temperatures between 1.5 - 4.2 K show a slight increase of the resistance with the stress at low stresses, followed by a rapid decrease of the resistance to very small values. For stresses above 2 kbar the resistance of Ge:As saturates with a further increase of stress. This in turn implies that unlike Ge:Sb, n_c of Ge:As shifts towards smaller values with increasing stress.

The valley-orbit splitting of Ge:P with $4\Delta=2.9$ meV lies between that of antimony (0.57 meV) and arsenic (4.15 meV). One expects the piezoresistance of Ge:P to be somewhere between that of As and Sb, namely, an appreciable increase followed by a large decrease of the resistivity with stress, which was in fact observed experimentally[67].

The first study (experimental[3] and theoretical[66]) of a metal-insulator transition induced by uniaxial stress was done in n-type Si:P. Si has six conduction band valleys along the [100] axis; the six-fold degeneracy of the donor ground state of Si:P is again removed by the relatively strong central-cell potential (~13 meV) producing a 1-fold, one 2-fold and one 3-fold degenerate state. Application of a moderate stress causes expansion of the ground state of Si:P, like in Ge:As. One can look at the metal-insulator transition under stress as a correlation-driven transition (Mott-Hubbard transition) in a lattice of hydrogenic atoms, where the disorder is effectively fixed. Stress

Reproduced with permission of the copyright owner. Further reproduction prohibited without permission.

alters only the donor wavefunctions and their overlap. In a Mott-Hubbard model, the transition from an insulator to a metal occurs at the concentration $n = n_c$ for which the upper Hubbard band (doubly occupied D^- band) merges with the lower Hubbard band (singly occupied D band) and the correlation gap disappears. R. N. Bhatt showed[66] that the application of uniaxial stress in Si:P strong central cell potential, mixes the ground state with the extended valley-orbit-split excited state, which in turn causes broadening of the occupied D band and lowering of the empty D^-. The latter is caused by the change of the effective potential due to the occupied band. Both effects reduce n_c as shown in Fig. III-2. He found that a stress of 2 kbar in a plane normal to the (111) axis induces a 3% decrease in n_c, in reasonable agreement with experimental findings of Paalanen et al[3].

Reproduced with permission of the copyright owner. Further reproduction prohibited without permission.

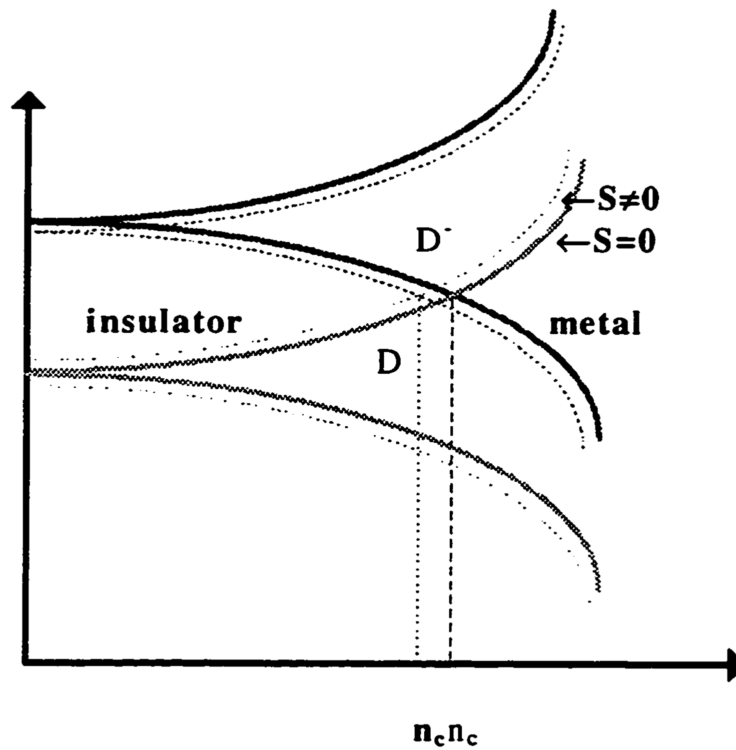

Fig. III-2. Mott-Hubbard transition at zero stress (solid line) and at some value of stress (dashed line). D^- band denotes doubly occupied donor (electron) band, whereas D denotes the singly occupied neutral donor state.

Reproduced with permission of the copyright owner. Further reproduction prohibited without permission.

3. *Stress-Induced MIT in p-type Si:B*

3.1 *Band Structure of p-type Semiconductors*

The acceptor wave functions of p-type semiconductors are derived from the Bloch functions at the top of the valence band. The valence bands of Si and Ge are degenerate at $k = 0$ at the center of the Brillouin zone due to the symmetry of their crystal lattice. Both Si and Ge have diamond structures that consist of two interpenetrating face-centered cubic (fcc) Bravais lattices, displaced along the body diagonal of the cubic cell by one quarter the length of the diagonal. They can be regarded as (fcc) lattices with two-point bases. Point Γ at $k = 0$ has the symmetry Γ'_{25} of the full cubic group O_h and the valence band edge state has 3-fold orbital degeneracy without spin[68]. Bloch wave functions corresponding to point Γ have the transformation properties of atomic p-wave functions (X, Y, Z) with orbital angular momentum L=1. This means that the top of the valence band would be 6-fold degenerate including 2-fold spin S degeneracy, (3-fold orbital degeneracy) x (2-fold spin degeneracy) without spin-orbit coupling. Spin-orbit coupling (total angular momentum $J = L + S$) partially removes the 6-fold degeneracy, leaving the top of the valence band 4-fold degenerate corresponding to $J=3/2$ state and shifting the 2-fold spin-orbit split, $J=1/2$ state down in energy by $\Delta = 0.044$ eV in Si[69] and $\Delta = 0.29$ eV in Ge[70](also see Bassani et al.[58]).

Reproduced with permission of the copyright owner. Further reproduction prohibited without permission.

Valence-band energy surfaces have been calculated by **k·p** perturbation techniques (see p. 187 ref. 68) generalized to (J,M_J) representation to include the spin-orbit interaction. The energy surface for the J=3/2 band has the following form:

$$E(k)_{l,h} = Ak^2 \pm [B^2k^4 + C^2(k^2_x k^2_y + k^2_x k^2_z + k^2_y k^2_z)]^{1/2}, \qquad \text{(III-A-3.1.1)}$$

where A, B, and C are inverse band parameters determined by cyclotron resonance measurement of Dresselhaus et al.[62] for Ge and Si and Hensel and Feher[71] for Si. The top of the valence band has two branches which are usually called light and heavy hole band and are shown in Fig. III-3. The energy surface of the J=1/2 band has the form

$$E(k) = -\Delta + Ak^2 , \qquad \text{(III-A-3.1.2)}$$

where Δ is the spin-orbit splitting energy mentioned above.

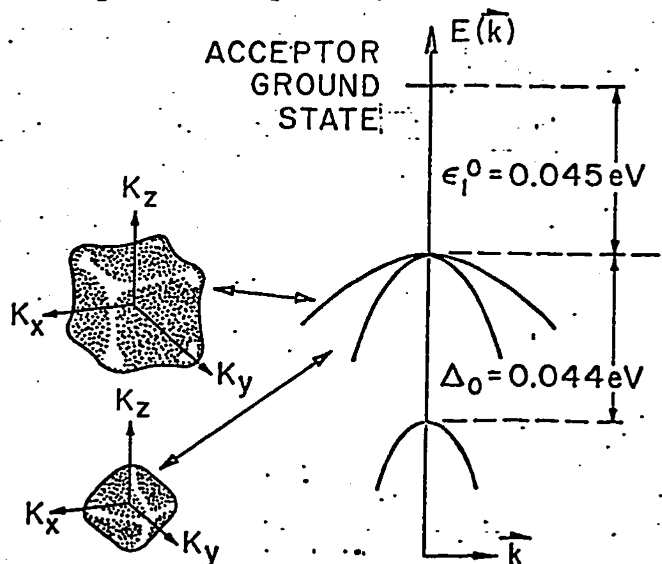

Fig. III-3 Energy surfaces of degenerate heavy and light hole bands with spin-orbit split band 44 meV below the top of the valence band.

Reproduced with permission of the copyright owner. Further reproduction prohibited without permission.

3.2 Acceptor States in EMA

The acceptor wave function in the EMA is a product of Bloch waves from near the top of the valence band and hydrogen-like envelope wave functions associated with each valence state[72]:

$$\psi(\bar{r}) = \sum_{j=1}^{6} F_j(\bar{r})\phi_j(\bar{r}) \qquad \text{(III-A-3.2.1)}$$

The envelope function F_j extends over dimensions of the order of 14 Å in Si and 42 Å in Ge. Each ϕ_j is a Bloch wave from the different j^{th} valence state, and it is a rapidly varying function compared to the envelope function, with the periodicity of the lattice. The effective-mass equation for the holes consists of six coupled differential equations

$$\sum_{j'}^{6} D_{jj'}^{\alpha\beta}\left(\frac{1}{i}\frac{\partial}{\partial \bar{x}_\alpha}\right)\left(\frac{1}{i}\frac{\partial}{\partial \bar{x}_\beta}\right)F_{j'}(\bar{r}) - \left(\Delta\delta_j + \frac{e^2}{\kappa \bar{r}}\right)F_j(\bar{r}) = EF_j(\bar{r}), \quad j = 1, \ldots 6, \quad \text{(III-A-3.2.2)}$$

where $\delta_j = \begin{cases} 0 & j = 1,\ldots4 \\ 1 & j = 5,6 \end{cases}$ and D is 6x6 $\mathbf{k \cdot p}$ perturbation matrix in (J, M_j) representation[62]. Approximate solutions to the equation (III-A-3.1.4) by variational methods[73,74,75] gave estimates for the acceptor ground state and a large number of excited states for Ge and Si. Results for the ground state energy of Si, in contrast to Ge, were not in a good agreement with experiments, since they neglected the contribution of the spin-orbit split band to the acceptor wave function. Variational calculations of Mendelson and Schultz[76] with trial wave functions

Reproduced with permission of the copyright owner. Further reproduction prohibited without permission.

containing a contribution from the spin-orbit split band gave much better estimates of the ground state energy and ground state wave function for Si. Reflecting the degeneracy of the valence band, the acceptor ground state is 2-fold degenerate.

3.3 The Effect of Stress on the Valence Band and The Acceptor Ground State of Si

Application of uniaxial compressive stress lifts the degeneracy of the light and heavy hole bands at k = 0. The splitting is highest for stress applied along the (100) or (111) direction, where the light hole band shifts upward in energy crossing the heavy hole band that shifts downward[71,77,78]. In the limit of very high stress, complex warped energy surfaces at zero stress will decouple and become prolate ellipsoids, as shown in Fig. III-4.

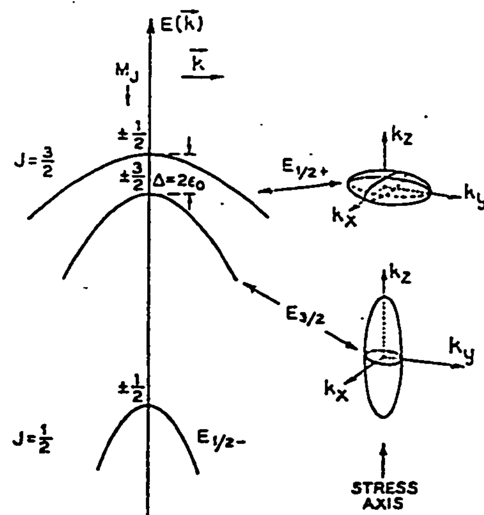

Fig. III-4 Splitting of the heavy and light hole bands under uniaxial compression along (001) axis.

Reproduced with permission of the copyright owner. Further reproduction prohibited without permission.

Detailed calculations of the energy shifts with stress for different valence bands can be found in the paper of Chroboczek et al.[77] and the Ph. D. thesis of Harold Staunton[79] (also, see references therein). In brief, one starts with the Hamiltonian describing the effects of spin-orbit interaction and strain on the valence band near $k = 0$[79]:

$$H = H_0 + H_\varepsilon \quad \text{(III-A-3.3.1)}$$

where $H_0 = H_k + H_{s.o.}$ is the EM Hamiltonian of Luttinger and Kohn[61] in (J, m_J) representation and H_ε (in the same representation) is the strain Hamiltonian given by[71,78,79,80]

$$H_\varepsilon = -a(\varepsilon_{xx} + \varepsilon_{yy} + \varepsilon_{zz}) - 3b[(L_x^2 - L^2/3)\varepsilon_{xx} + \text{c.p.}] - 6d/\sqrt{3}[\{L_xL_y\}\varepsilon_{xy} + \text{c.p.}] \quad \text{(III-A-3.3.2)}$$

Here $\varepsilon_{ij} = \Sigma S_{ijkl}X_{kl}$ are components of the 3x3 strain tensor, L is the angular momentum operator, c.p. are the cyclic permutations with respect to x, y, and z and $\{L_xL_y\}=1/2(L_xL_y + L_yL_x)$, etc. The parameters a, b, and d are the hydrostatic deformation potential, and the shear deformation potentials for strains of tetragonal [001] and rhombohedral [111] symmetries, respectively. For the stress applied along the [001] axis, ignoring the hydrostatic term (since it shifts all the bands equally) equation (III-3.3.2) becomes

$$H_\varepsilon = -3b(L_z^2 - L^2/3)(S_{11} - S_{12})X \quad \text{(III-A-3.3.3)}$$

S_{11} and S_{12} are elastic compliance constants and X is stress. By diagonalizing the Hamiltonian of equation (II-3.3.1) Chroboczek et

Reproduced with permission of the copyright owner. Further reproduction prohibited without permission.

al.[77] calculated the displacement of the valence bands and the acceptor states with stress. The 2 fold acceptor state splits into two levels Γ_7 and Γ_6 shifting in opposite directions with stress, as shown in the Fig. III-5 (adopted from Chroboczek et al.[77]). Measurements[77] of Si:B down to 1.5 K showed a rapid increase of the resistivity with stress up to approximately 3 - 4 kbar, followed by a much slower decrease in resistivity with a further increase of the stress. Similar behavior of the resistivity with stress at 4.2 K shown in Fig. III-A-6 was found by Bogdanovich et al.[81] (unpublished). An initial, rapid increase of the resistivity with stress is attributed to splitting of the degenerate impurity ground state (as in n-type Ge:Sb) that leads to shrinkage of the impurity wave function and a consequent decrease in the overlap. Application of stress drives a metallic sample into the insulating phase by increasing n_c.

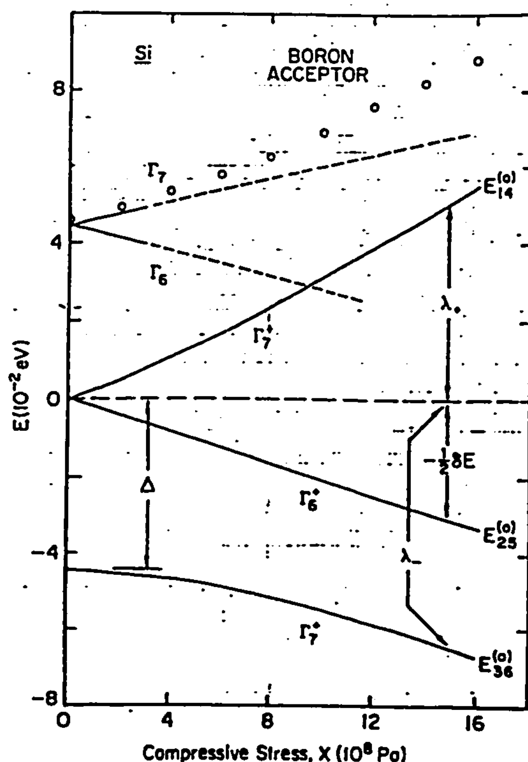

Fig. III-5. Energy level shifting as a function of uniaxial stress along (001) axis. (Chroboczek et al.[77])

Reproduced with permission of the copyright owner. Further reproduction prohibited without permission.

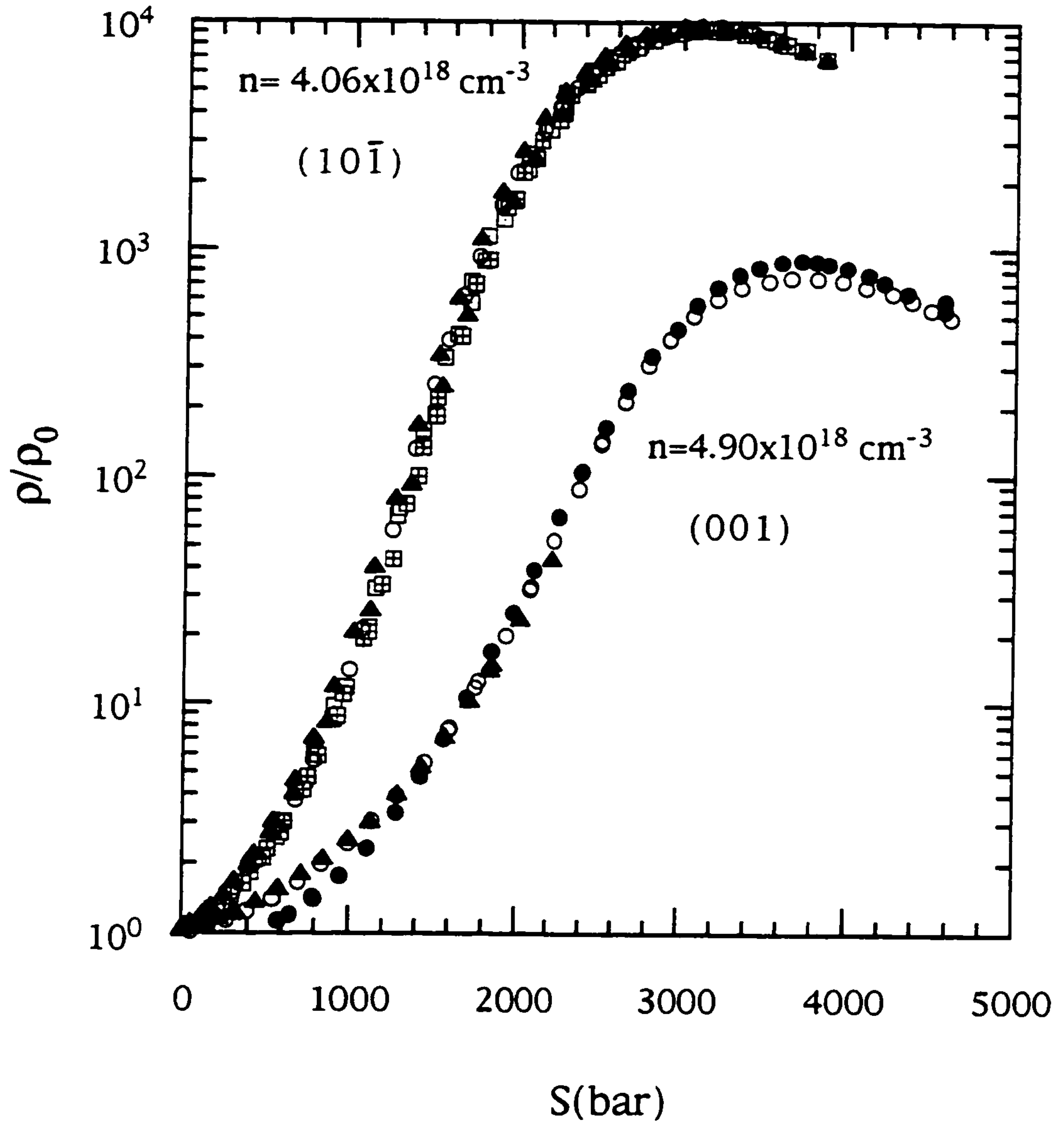

Fig. III-6. Resistivity at 4.2K normalized to its zero-stress value as a function of uniaxial stress for two samples with dopant concentration n and direction of stress as denoted above.

Reproduced with permission of the copyright owner. Further reproduction prohibited without permission.

3.4 Stress-Induced MIT for p-type Si:B

It was found by Bogdanovich at al.[82] that the application of a uniaxial stress of ~ 600 bar in Si:B along the (001) axis induces an increase of n_c of about 20% (for details see part *C* of this chapter). Using the same method applied to the stressed-tuned MIT in n-type Si:P[65] one could predict approximately how the stress-induced MIT occurs in Si:B. Within the Mott-Hubard picture of the MIT, one expects the shrinkage of the lower Hubbard (A) band with increasing stress reflected by the decrease in the overlap of the neighboring wave function and the splitting of the acceptor ground state with stress. This in turn, should raise the upper Hubbard (A^+) band, so that the bands will cross each at some higher value of n_c, as shown in Fig. III-7.

Reproduced with permission of the copyright owner. Further reproduction prohibited without permission.

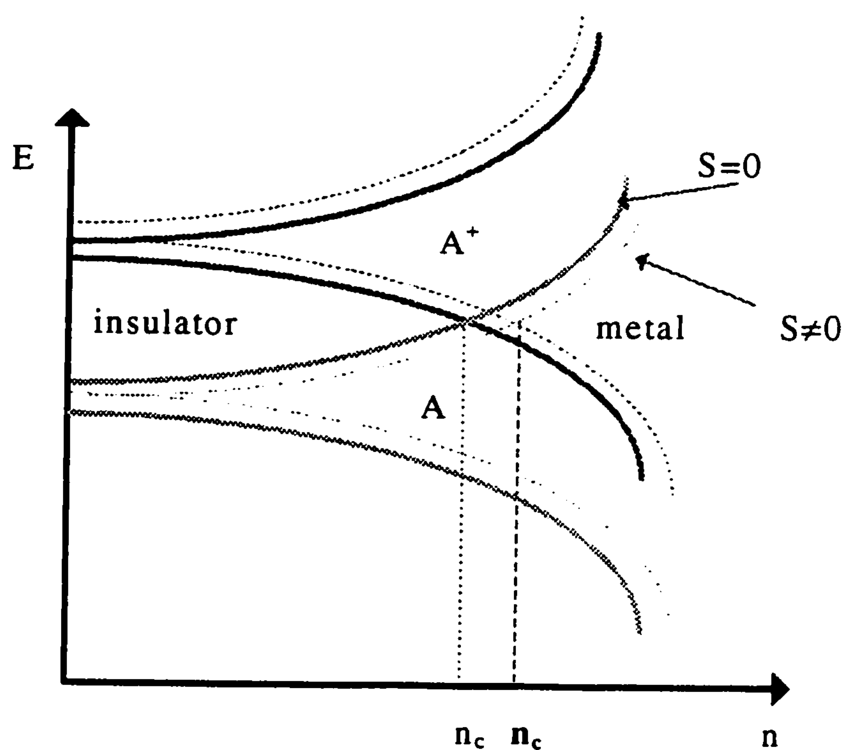

Fig. III-7. Mott-Hubbard transition at zero stress(solid line) and at some value of stress(dashed line). The A^+ band denotes doubly occupied acceptor (hole) band, whereas A denotes the singly occupied neutral acceptor state.

Reproduced with permission of the copyright owner. Further reproduction prohibited without permission.

B. Experimental Procedure

1. Sample preparation and characterization

A boule of Si:B grown along the [100] axis by the Czochralski method was obtained from Dr. Gordon Thomas at Bell Labs, Lucent Technologies and cut into 0.3 mm thick wafers with [100] orientation by Semiconductor Processing Corporation. One side of the wafer was fine polished at The Laboratory for Laser Crystal Growth at the Physics Department of City College for better contrast between ion-implanted areas of the sample and the rest of the sample surface. Laue backscattering x-ray diffraction was used to determine the orientation of the [001] axis within the plane of each wafer. Wafers were then cut along the [001] into bars. The dimensions of a bar shaped-sample used in these measurements were 8.0x1.25x0.30 mm^3. The sample was then etched in a 2% HF solution of HNO_3 for 10 minutes to remove all the impurities and mechanical damage incurred during the cutting process. For better electrical contacts to the sample (see Chapter II, part B, section 1) boron B^+ ion implants were applied to four thin striplike areas. It was found that doses of E = 20keV and a concentration of B^+ ions $C = 5\times10^{15}cm^{-2}$ gave best results. The sample was then annealed in vacuum at 800^0C for 30 minutes to activate the implants. After the removal of the oxide layer (using $HF:H_2O$ in the ratio 1:50) four thin gold wires were attached to the implanted areas using an arc discharge technique[29]. The room-temperature resistivity ρ_{300K} and the ratio $r = \rho_{4.2K}/\rho_{300K}$ of the 4.2 K resistivity and the room temperature resistivity was measured to determine the boron concen-

Reproduced with permission of the copyright owner. Further reproduction prohibited without permission.

tration as described in Chapter II, part B, section 2. The ratio r was also measured for several other samples cut from the same wafer with different lead configurations to check for possible inhomogeneous doping. It was found that the variation in dopant concentration n was less then 1%. The following table, lists the values of ρ_{300K}, $r = R_{4.2K}/R_{300K}$, and n of the sample used in these measurements.

TABLE III-B Room temperature resisitivity, ratio of the 4.2 K resistance and room temperature resistance, and Boron concentration of the sample.

ρ_{300K} (ohm-cm)	$r = R_{4.2K}/R_{300K}$	$n(cm^{-3})$
0.0151	1.53	4.84×10^{18}

The boron concentration of this sample is 20% above the critical concentration $n_c = 4.06 \times 10^{18}$ cm^{-3} at zero stress[32].

2. *Experimental setup*

The sample was cooled down to 0.05 K in an Oxford model 75 dilution refrigerator. A capacitive pressure cell[3] using He^4 was used to uniaxially compress the sample (see Fig. III-8). This device was tightly screwed to the mixing chamber of the dilution refrigerator, which is shown in Fig. III-9.

Reproduced with permission of the copyright owner. Further reproduction prohibited without permission.

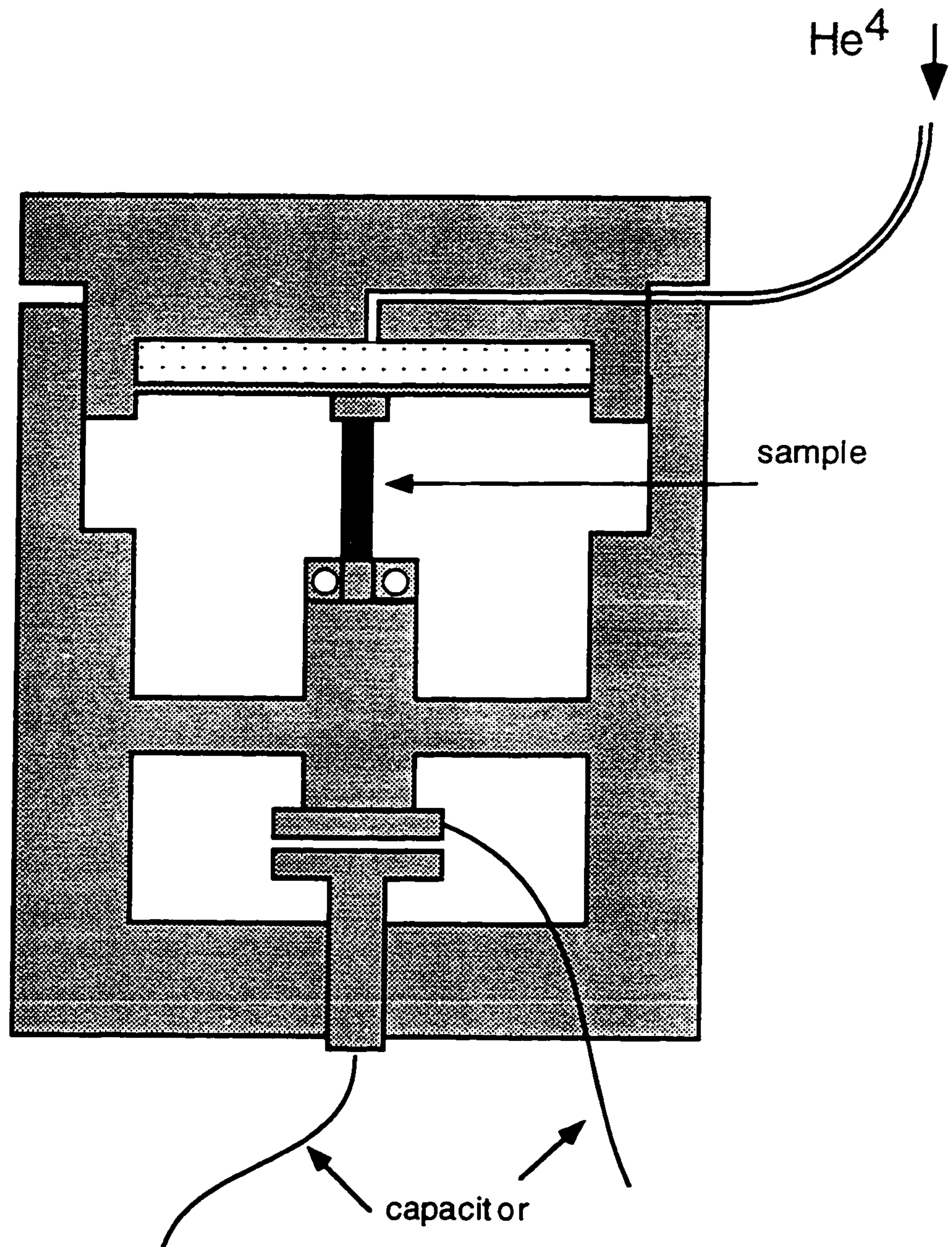

Fig. III-8 Pressure cell

Reproduced with permission of the copyright owner. Further reproduction prohibited without permission.

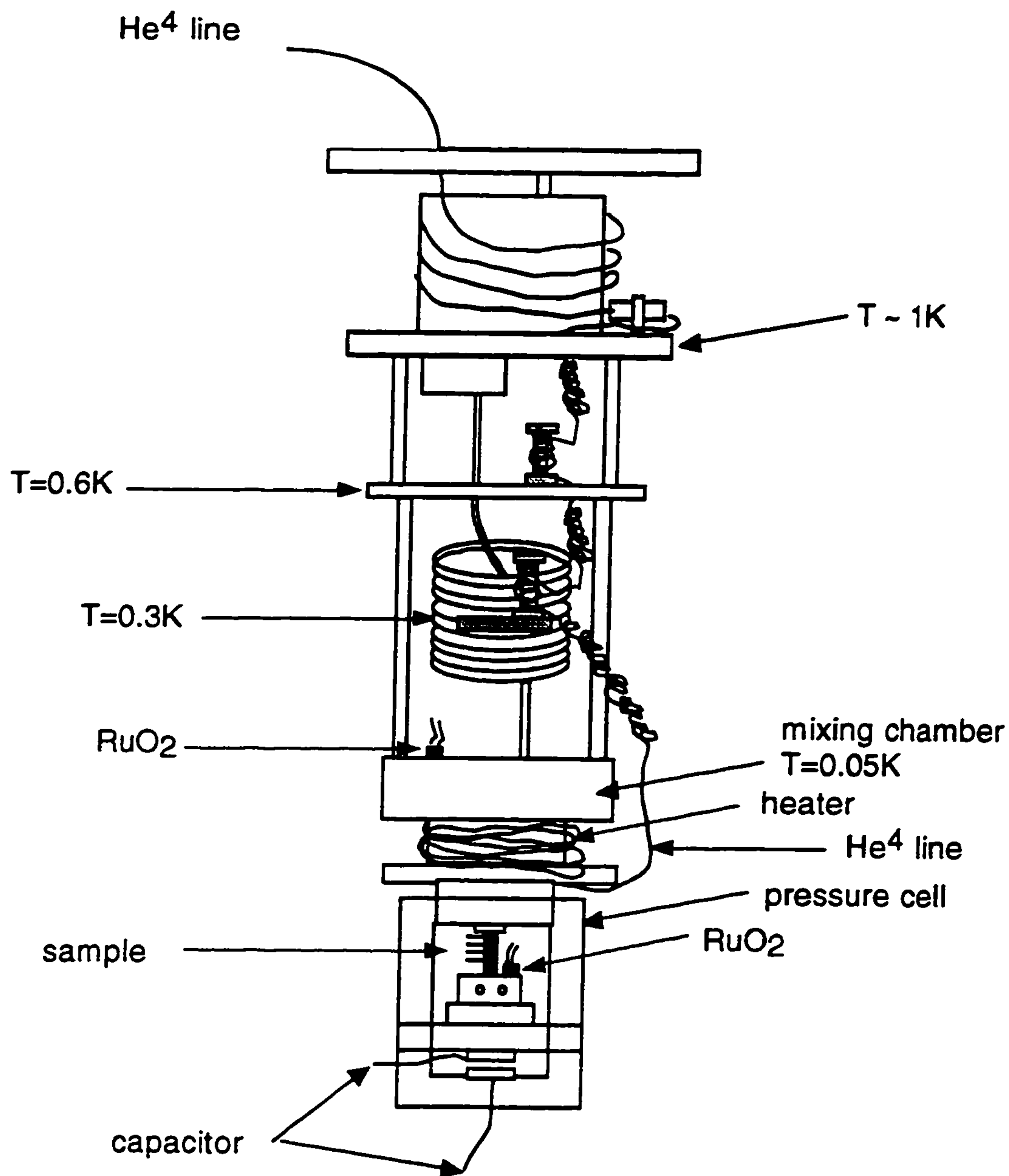

Fig. III-9 Insert of the dilution fridge with the pressure cell

Reproduced with permission of the copyright owner. Further reproduction prohibited without permission.

2.1 Pressure Cell

2.1a Design

The design of the pressure cell used in the experiments of Paalanen et al.[3] was obtained from Bell Labs. The cell was made of BeCu, a material known for its hardness, good elastic properties (small hysteresis) and relatively good thermal conductivity. The sample was seated in the center of the cell, fixed with a copper plate and two screws to prevent any horizontal motion. In this arrangement half the area of the sample was covered by the plate. The other half contained four electrical leads connected to the outside wires through the oval opening on the wall of the cell. The top part of the cell (the cap) contains a small compartment with a thin circular membrane and an opening on one side to introduce He^4. The cap slides into the body of the cell and the six copper screws are tightened until the membrane touches the sample. OFC (oxygen free copper) screws were used for better thermal contact between the cap and the body of the cell. The lower part of the cell contains a plate capacitor; the capacitance is defined as $C = \varepsilon_0 A/d$, where ε_0 is dielectric constant of vacuum, A is the area of the capacitors plates and d is the distance between the plates. When stress is applied to the sample the upper plate moves downward decreasing the distance d between the capacitor plates, which in turn will increase the value of the capacitance. By recording the changes in capacitance one can determine the amount of stress applied. Increasing the He^4 pressure at the top exerts force on the sample through a ≈1" diameter membrane. Due to the large ratio of the area of the membrane to the area of the sample, a few bars of He^4 pressure produces a few hundred or thousands of bars of compres-

Reproduced with permission of the copyright owner. Further reproduction prohibited without permission.

sional stress. Thin sheets of silver or 50%-50% SnPb solder were placed at both ends of the sample to cushion surface roughness and increase the amount of stress one can apply without breaking it.

2.1b Calibration

The cell was calibrated at room temperature by recording the changes of capacitance with applied force (weight). The stress is obtained by dividing the force F by the area A of the sample perpendicular to the force, $S = F/A$. Several curves of force F versus relative change of capacitance ΔC were recorded and are presented in Fig. III-10 a). When the temperature is lowered to 4.2K, the capacitance of the cell (~ 10 pF) decreases by less than 1% and it stays the same with further decrease of the temperature. At temperatures of 4.2 K and lower the slope of the calibration curve is smaller in comparison to the room temperature slope. One can account for this difference by recording the changes of capacitance ΔC as a function of He^4 pressure ΔP at 300 K and 4.2 K presented in Fig. III-10 b). Using the ratio (~ 1.6) of the two slopes $(\Delta C/\Delta P)_{300K}$ and $(\Delta C/\Delta P)_{4.2K}$ allows us to rescale the room-temperature calibration to 4.2K (or lower T)-calibration. An alternative method would be to calibrate the cell at 4.2 K, since further decrease of temperature will not cause any change of the slope.

Reproduced with permission of the copyright owner. Further reproduction prohibited without permission.

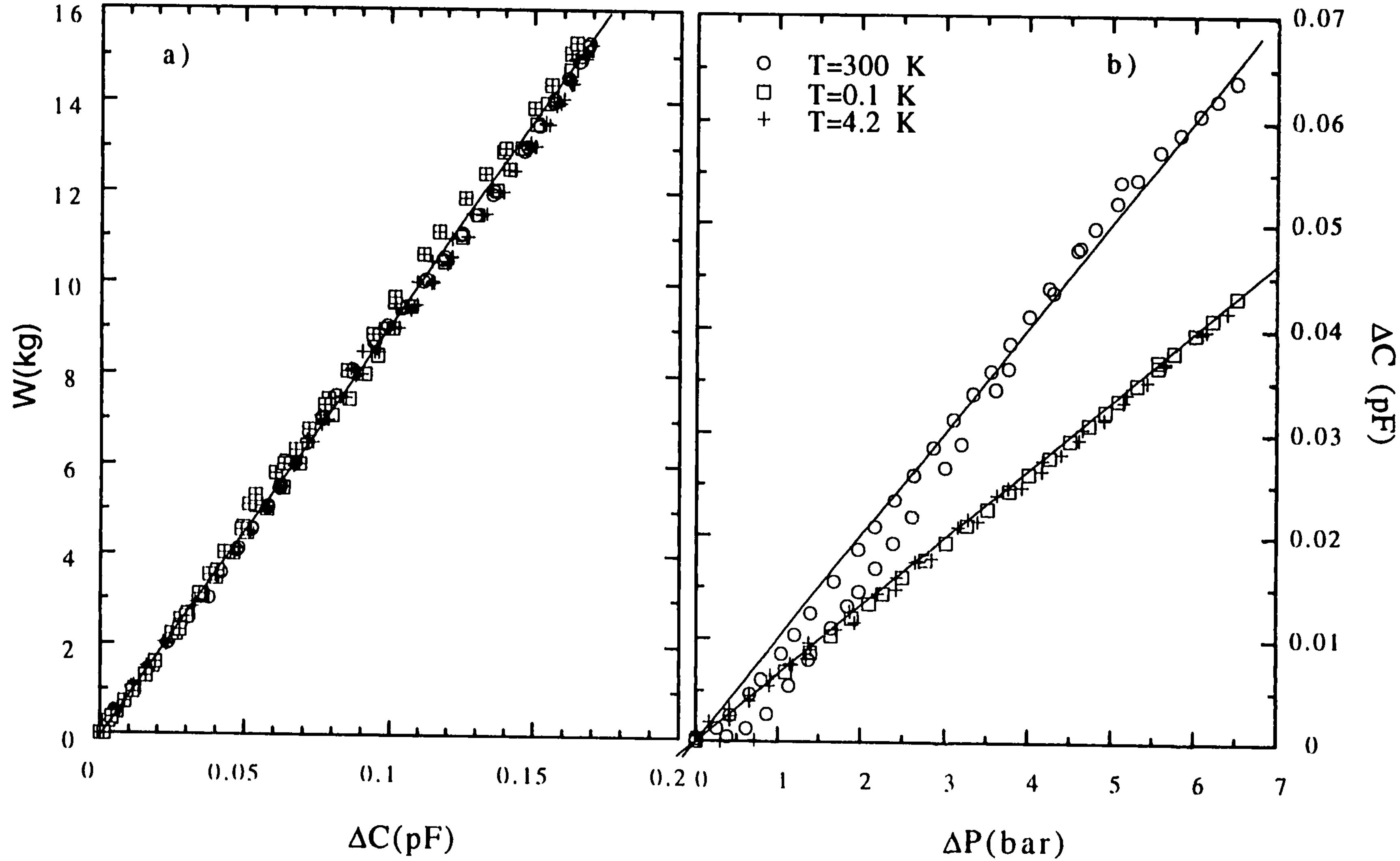

Fig. III-10. a) Several calibration curves showing the relative change of the capacitance as a function of weight; b) Relative change of the capacitance as a function of relative change of the He^4 pressure at 300 K, 4.2 K and 0.1K.

Reproduced with permission of the copyright owner. Further reproduction prohibited without permission.

2.1c Capacitance Measurements

The capacitance of the pressure cell was measured using a General Radio Capacitance Bridge model 1615-A, at a frequency of f = 1 kHz. The accuracy of the bridge at this frequency is (±0.01% ±0.00003pF). The smallest change of capacitance recorded on the 100pF range was 10^{-4} pF corresponding to approximately 3 bar of stress. The capacitance bridge was interfaced with a PAR Lock-in Amplifier model 124A with input impedance of 100 MΩ.

The excitation voltage used for the measurement of the impedance of the cell was 2 V. Values of the capacitance were obtained by balancing the bridge until the voltage reading of the in-phase and out-of-phase signal of the Lock-in Amplifier became zero (on the 5 μV scale). A three-terminal measurement of capacitance was used, with the body of the cell and the shields of the two coaxial cables connected to ground. Two Lakeshore stainless steel coaxial cables (0.04 inch in diameter) were connected to the capacitor at the lower end of the cell with Microtec miniature coaxial connectors.

2.2 Gas Handling System

The pressure cell was operated by high purity He^4, which is in gaseous form at room temperature. The gas-handling system consisting of a cylinder of high purity He^4, a 15 liter ballast cylinder, a liquid nitrogen cold trap and a capacitive pressure gauge connected by different size tubes and capillaries is shown in Fig. III-11.

Reproduced with permission of the copyright owner. Further reproduction prohibited without permission.

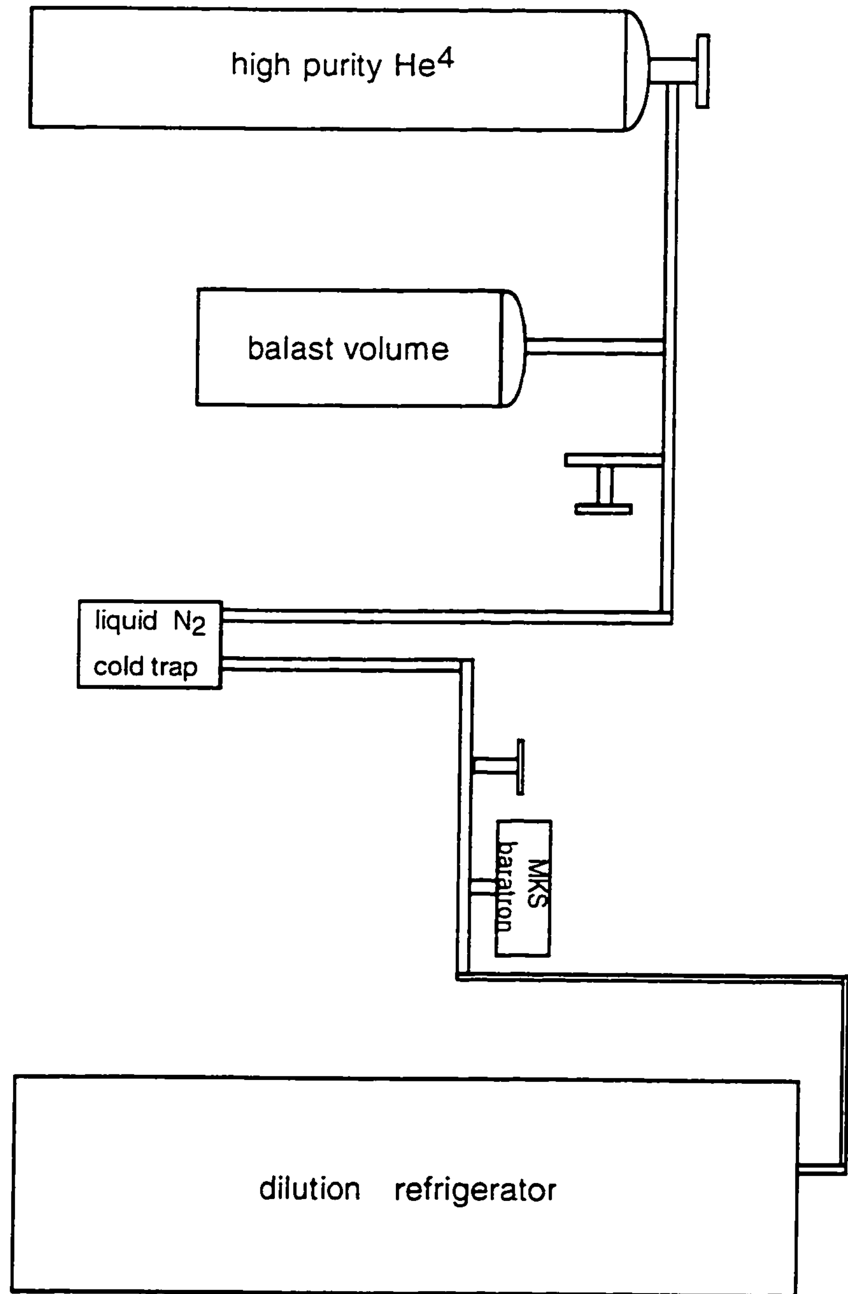

Fig. III-11 Gas handling system

Reproduced with permission of the copyright owner. Further reproduction prohibited without permission.

A large ballast volume was used to reduce the variations in pressure caused by the continuous change of the liquid helium level inside the dilution refrigerator and variations in room temperature. Variations in pressure in this measurement were of the order of a few mbar, while the measured changes of pressure were approximately 250 mbar. Before introducing it into the dilution refrigerator, purified He^4 was additionally cleaned by using a liquid nitrogen cold trap filled with charcoal. The pressure of the He^4 gas at room temperature was measured with MKS baratron model 120A, with an accuracy of $\pm$ 0.12% in the range of 33 bar (500 psi). At the lowest temperatures ~50 mK, He^4 is in its superfluid phase, and the pressures that could be reached before He^4 solidifies are ~30 bar. The highest pressure recorded in this measurement was 9 bar, much smaller than the critical pressure at which He^4 enters its solid phase. Two cylinders, the cold trap and the pressure gauge were connected by soft-soldered 1/4 inch copper tubes with a set of high pressure regulating valves. The copper tube was hard-soldered to a long stainless-steel capillary of 1/16 inch outer diameter and 0.01 inch inner diameter that entered the dilution refrigerator from the top. The capillary was then wound several times around the 1K pot for thermal heat sinking. Additional heat-sinking at 1K was accomplished by using a small volume (few cm^3) OFC cylinder thermally anchored to the 1K plate. The cylinder contained two different size holes on the two ends with the stainless-steel capillary entering from one end and a Cu-Ni capillary of 0.01 inch outer diameter and 0.004 inch inner diameter connected to it at the other end. He^4 undergoes a liquid to superfluid transition at 2.19 K below which it becomes a an excellent heat conductor. Additional heat-sinking of the capillary at 0.6 K and 0.3 K was necessary. Since the heat con-

Reproduced with permission of the copyright owner. Further reproduction prohibited without permission.

duction of superfluid He^4 drops with increasing length of the capillary and with decreasing radius[33], one needs to use very thin capillary and extend its length to approximately 1/2 m between each heat-sinking stage. Heat-sinking was achieved by coiling the Cu-Ni capillary around a OFC spool and then soft-soldering to it. Each copper spool was then tightly screwed to a different cold surface. The end of the capillary was soft-soldered to the upper part (cap) of the pressure cell, which is thermally anchored to the mixing chamber of the dilution refrigerator. In this configuration one has a large density gradient of He^4, but uniform pressure from 300 K down to 0.05 K along the He^4 line.

2.3 Electrical wiring

Electrical wiring of the sample heater and thermometers was very similar to that already described in Chapter II, part B, section 3.3, except for different wiring at the mixing chamber. The mixing chamber used in this experiment was made of stainless steel and had much smaller volume of cooling He^4-He^3 mixture. The sample was seated inside the cell tightly screwed to the bottom of the mixing chamber and surrounded by vacuum instead of mixture. Four wires connecting the sample to the outside of the dilution refrigerator were low resistance, thin copper wires heat-sinked at several stages as described above. Again, superconducting wires were used between the 1K pot and the mixing chamber. Additional heat-sinking of the sample wires at the mixing chamber was necessary to provide better cooling of the sample. Four superconducting wires were then connected to

Reproduced with permission of the copyright owner. Further reproduction prohibited without permission.

four thick copper wires thermally anchored at the mixing chamber and then connected to the sample leads inside the cell. Thick copper wires were used to increase the cooling of the sample by electrons. At mili Kelvin temperatures there are very few phonons available for heat transfer and therefore cooling of the sample through the thermal contact with the cell is limited.

2.4 Thermometry and Temperature Control

Two RuO_2 thermometers were used to measure the temperature of the mixture and the sample. One of the thermometers was placed at the mixing chamber and the other inside the pressure cell very near the sample. To improve the thermal contact between the thermometer and the cell, the RuO_2 thermometer was placed in a small drop of stycast 2850, which was allowed to harden and then glued to the surface of the cell. The temperature of both thermometers was recorded as the sample heated up and as it cooled down slowly. A substantial temperature difference between the sample and mixing chamber developed on heating, becoming larger as the temperature increased; there was no gradient during slow cooling. Data obtained using the thermometer inside the cell on heating and cooling showed very good consistency.

Heating of the sample and the cell was achieved by winding a 500Ω heater wire around the top part of the cell, just between the mixing chamber and the cell. The heater and the sample thermometer were connected to a Linear Research INC. AC Resistance Bridge model LR-700 for temperature control and measurement.

Reproduced with permission of the copyright owner. Further reproduction prohibited without permission.

2.5 Resistance Measurement

Longitudinal low-frequency AC resistance measurements were done by passing the current along the stress direction through two outer leads in a configuration shown in Fig. III-12 and measuring the voltage between the two inner leads. The resistance was measured with a Stanford Research System model SR850DSP lock-in amplifier at a frequency of 13 Hz. A 100 kΩ resistor was placed in series with the lock-in amplifier to obtain low excitation currents. At the lowest temperatures the power level was always kept below 10^{-14} W.

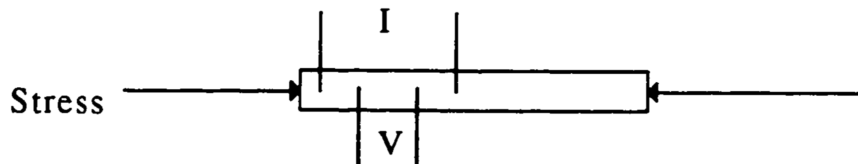

Fig. III-12 Current I and voltage V configuration of electrical leads on the sample, with the current applied along the stress direction.

Reproduced with permission of the copyright owner. Further reproduction prohibited without permission.

C. Results and Discussion

The longitudinal conductivity of a Si:B sample with dopant concentration $n = 4.84 \times 10^{18}$ cm^{-3} was measured between 0.05 - 0.76 K at different values of uniaxial compressional stress. Increasing stress drives this metallic sample into the insulating phase by decreasing its conductivity. The conductivity as a function of stress at 4.2K is presented in Fig. III-13. It decreases approximately linearly with the stress for $S > 200$bar. Comparing the conductivity as a function of stress and the conductivity as a function of dopant concentration n one can determine the relation between the stress and the dopant concentration. The data at 4.2 K is used to establish this relation, since at this temperature one is well above the critical region. The conductivity as a function of dopant concentration at 4.2 K (data adopted from Dai et al.[25]) is presented in Fig. III-14. The boron concentration n was determined from Thurber[31] calibration curve as mentioned before. From the Fig. III-14, it is clear that the conductivity varies linearly with dopant concentration as well, suggesting that stress scales linearly with dopant concentration.

The temperature dependence of the conductivity for twenty different fixed values of stress is shown on a log-log plot in Fig. III-15. Starting with metallic behavior at zero stress one enters the insulating phase at some critical stress which will be determined from the analysis of the data presented in sections 1, 2, and 3. Flattening of the curves below 70 mK is due to some thermal decoupling of the sample from the cell and the thermometer. For the curves with the highest value of stress the resistance of the sample below 150 mK

Reproduced with permission of the copyright owner. Further reproduction prohibited without permission.

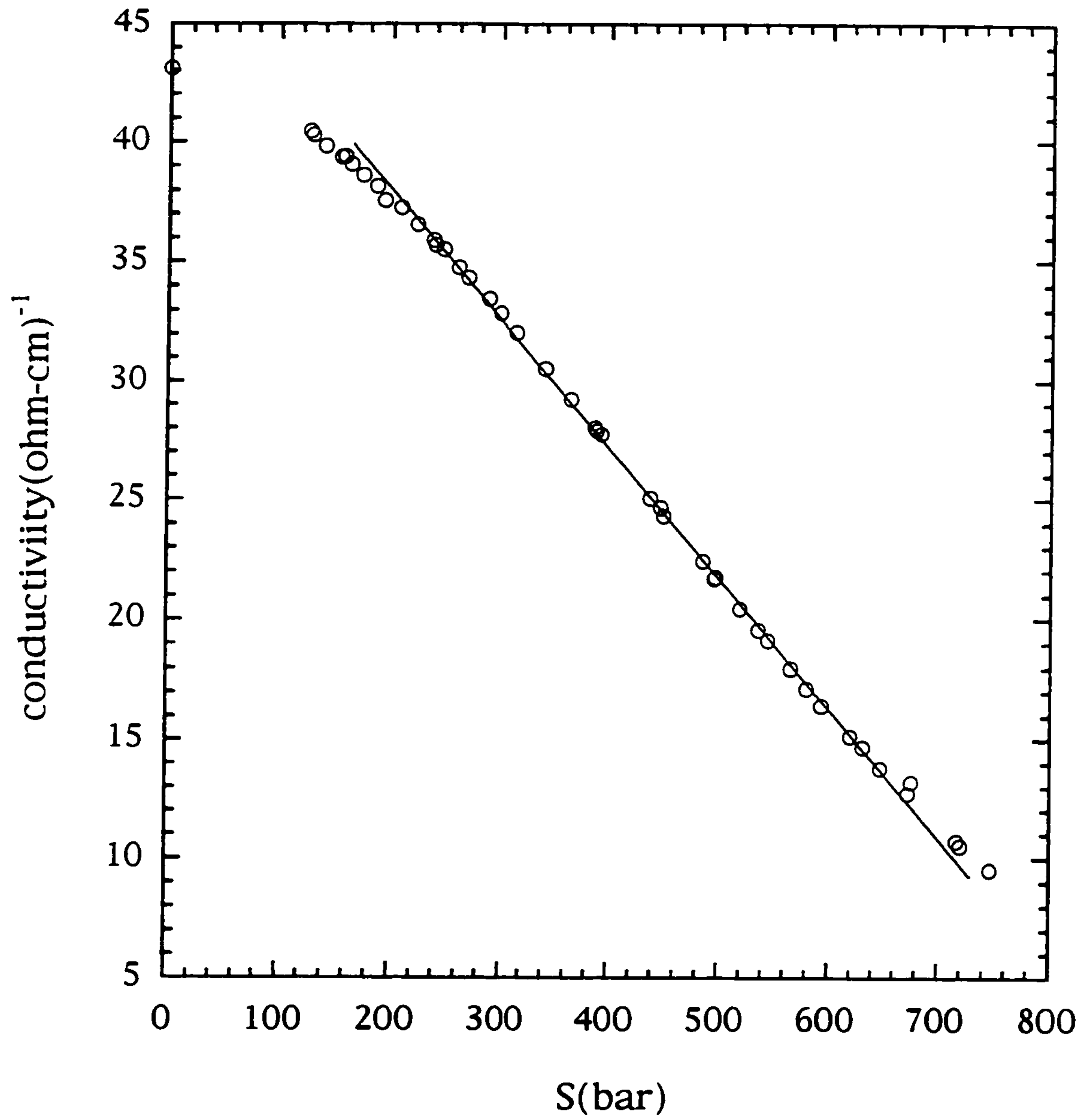

Fig. III-13 Conductivity as a function of stress at T=4.2 K.

Reproduced with permission of the copyright owner. Further reproduction prohibited without permission.

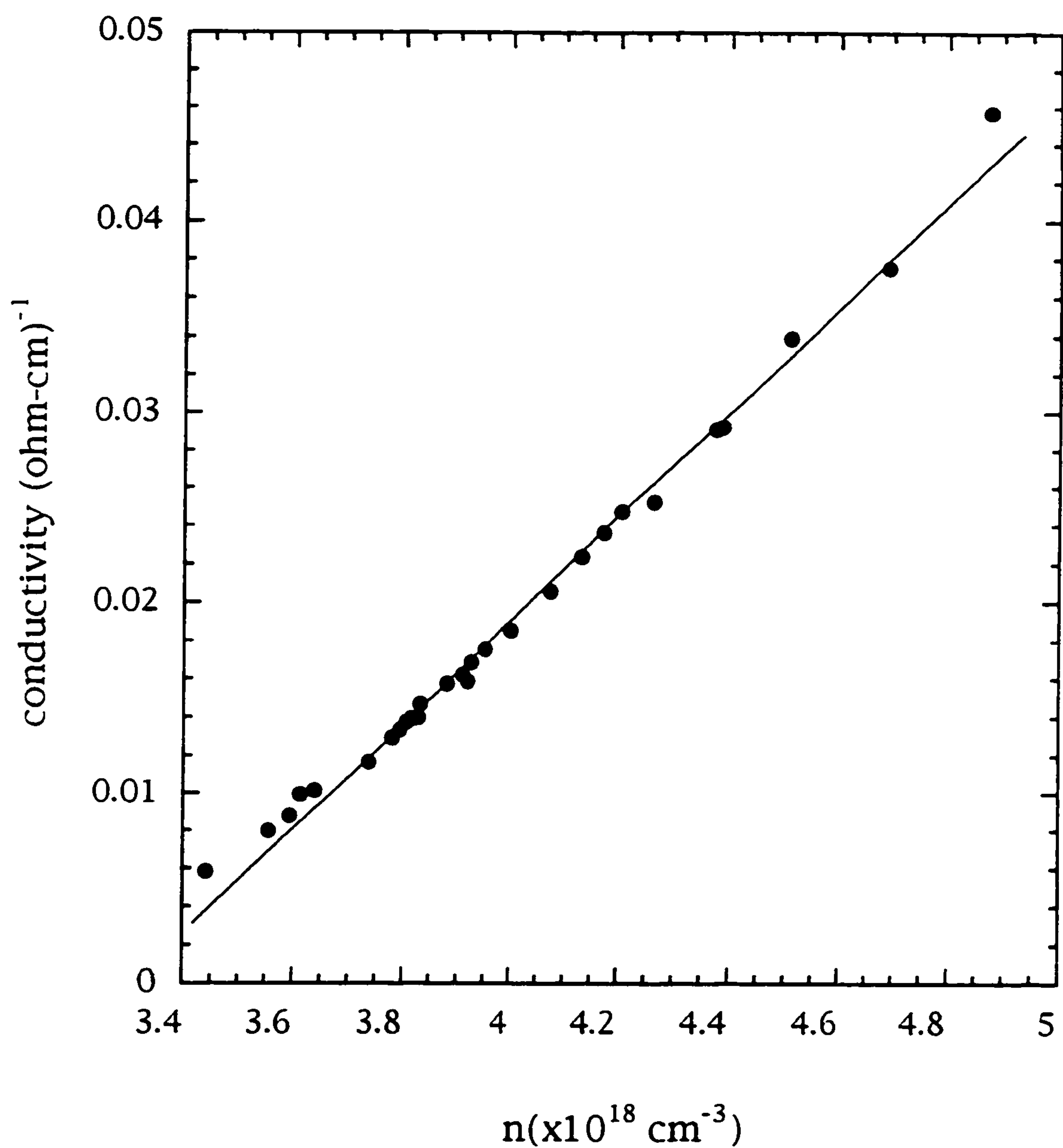

Fig. III-14 Conductivity as a function of boron concentration at T=4.2 K. (Data adopted from Dai et al.[25])

Reproduced with permission of the copyright owner. Further reproduction prohibited without permission.

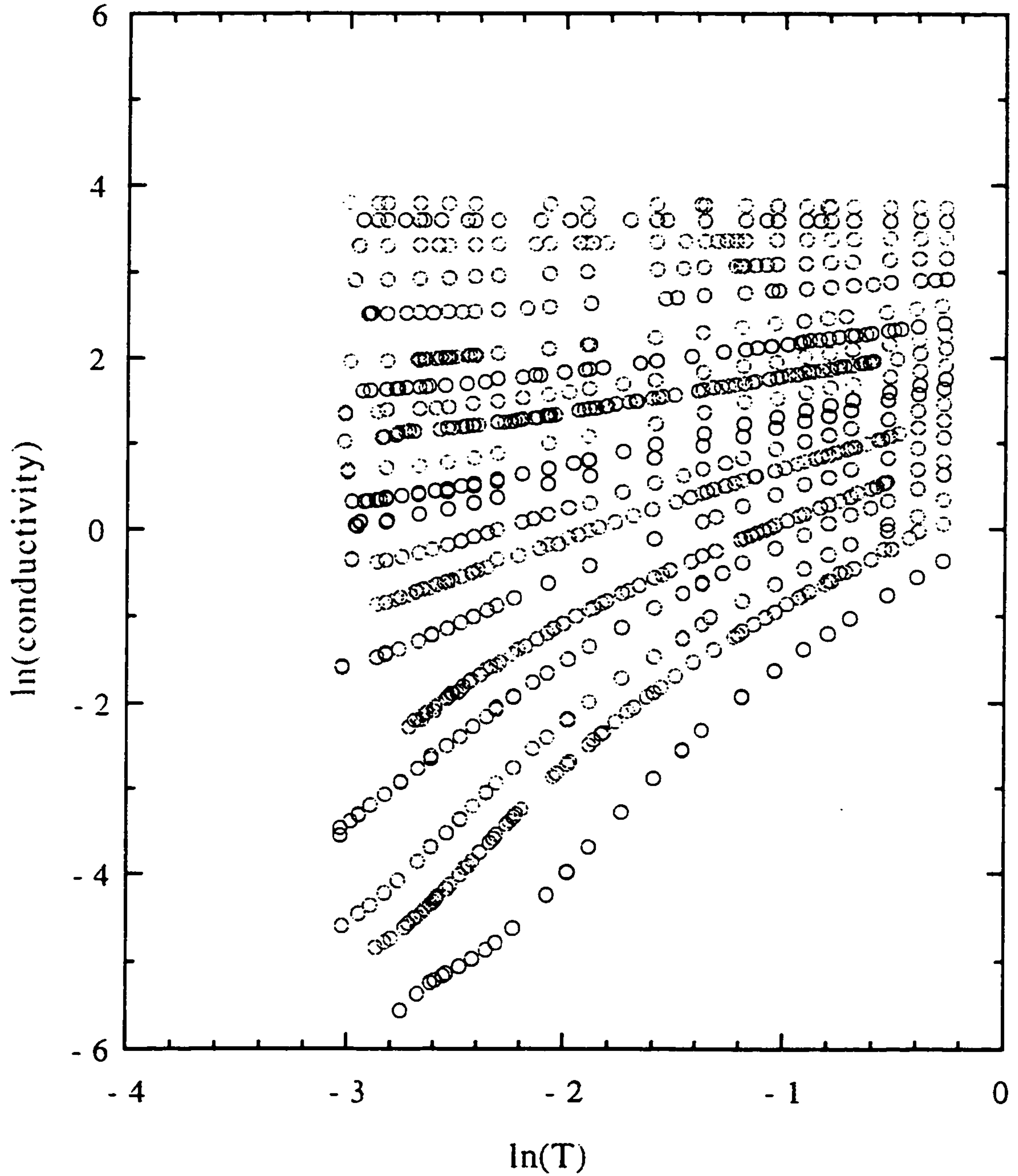

S(bar): 100, 211, 296, 369, 430, 503, 560, 583, 613, 637, 649, 678, 708, 726, 756, 778, 809, 832, 873

Fig. III-15. Ln(σ) as a function of ln(T)

Reproduced with permission of the copyright owner. Further reproduction prohibited without permission.

becomes of the order of $10^4\Omega$ above which it cannot be measured accurately using the low frequency AC method. These data will be disregarded in the following analysis.

1. Dynamical Scaling of the Conductivity near the MIT

Using the dynamical scaling analysis described in part A, section 1, one can try to scale the conductivity as a function of temperature T and stress S. Equation (III-A-1.1),where parameter t = S and $\delta t = \delta S = S - S_c$ can be rewritten in the form $\sigma = \sigma_c f(T^*/T)$, where the critical conductivity $\sigma_c = AT^{\mu/z\nu}$and $T^* \propto \delta S^{\nu z}$. One starts by assuming that one of the curves in Fig. III-15 is the critical curve and then divides every other curve by the critical curve. The ratio of the conductivity for different values of stress to the critical conductivity σ_c for six different choices of S_c is plotted as a function of T*/T in Fig. III-16, Fig. III-17, Fig. III-18, Fig. III-19, Fig. III-20 and Fig. III-21on a log-log scale. Reasonably good scaling is obtained for four choices of S_c between 583 and 708 bar. The data collapse onto two different conductivity branches, one metallic (top curve) and one insulating insulating branch (bottom curve). This was achieved by shifting each curve on a log-log scale along the x-axis corresponding to different multiplicative factors T*. It is obvious from Fig. III-16 and Fig. III-21 that the scaling begins to break down for the choice of S_c = 583 bar (the metallic branch doesn't scale) and for the choice of S_c = 708 bar (the insulating branch doesn't scale). These two are limiting values for the choice of critical stress. Small deviations from scaling for S_c = 613 bar and S_c = 637 bar are due to thermal decoupling at the lowest temperature, mentioned above. The

Reproduced with permission of the copyright owner. Further reproduction prohibited without permission.

multiplicative factor T^* is plotted as a function of $\delta S = |S-S_c|$ for both metallic and insulating phase in the insets to Fig. III-17, Fig. III-18, Fig. III-19, and Fig. III-20. The temperature dependence of the critical conductivity for the choices of S_c =613 bar and S_c =638 bar are presented in Fig. III-22 and Fig. III-23, respectively.

Reproduced with permission of the copyright owner. Further reproduction prohibited without permission.

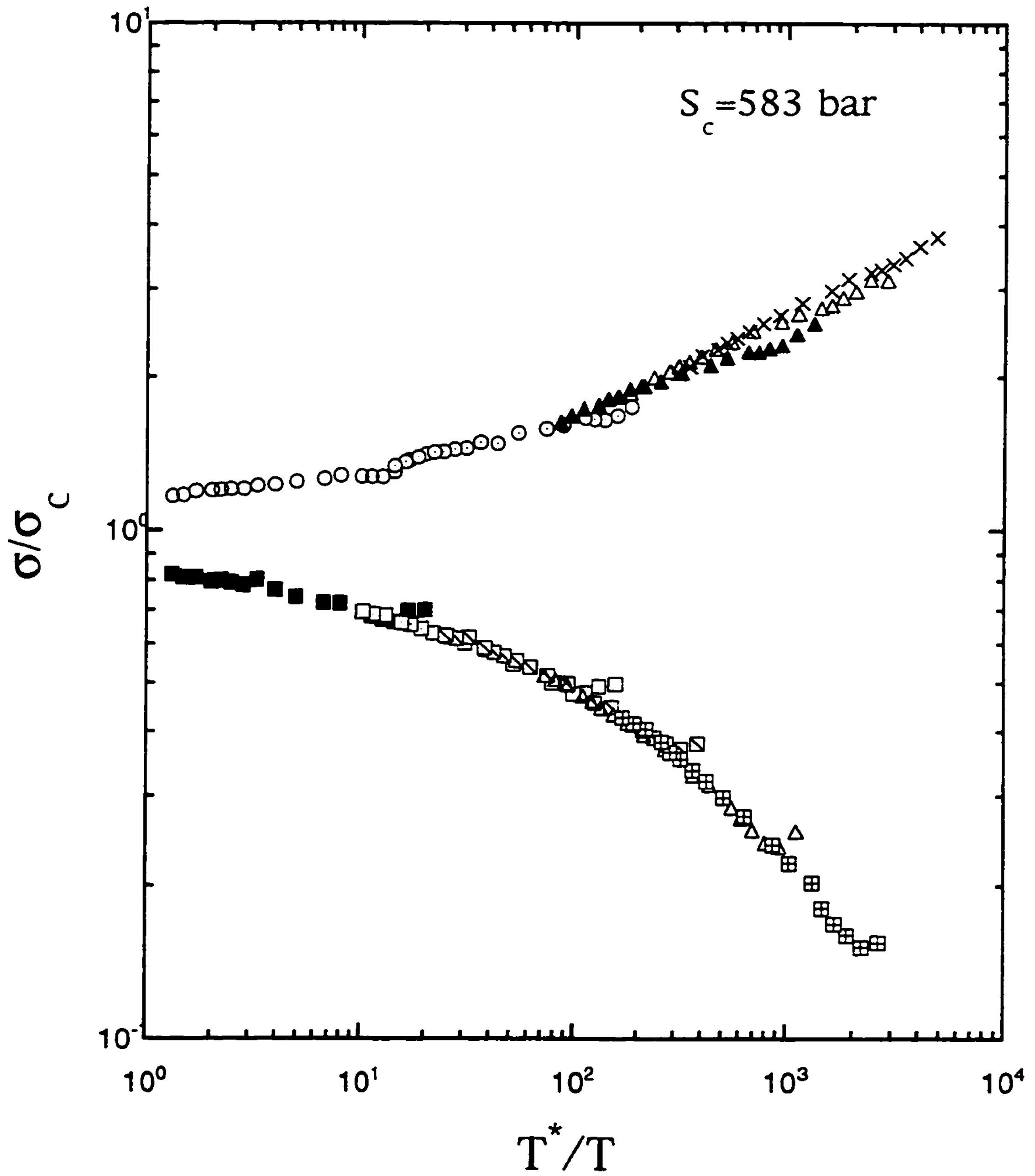

Fig. III-16 Ratio of the conductivity at different value of stress and the critical conductivity at S_c= 583 bar as a function of T*/T.

Reproduced with permission of the copyright owner. Further reproduction prohibited without permission.

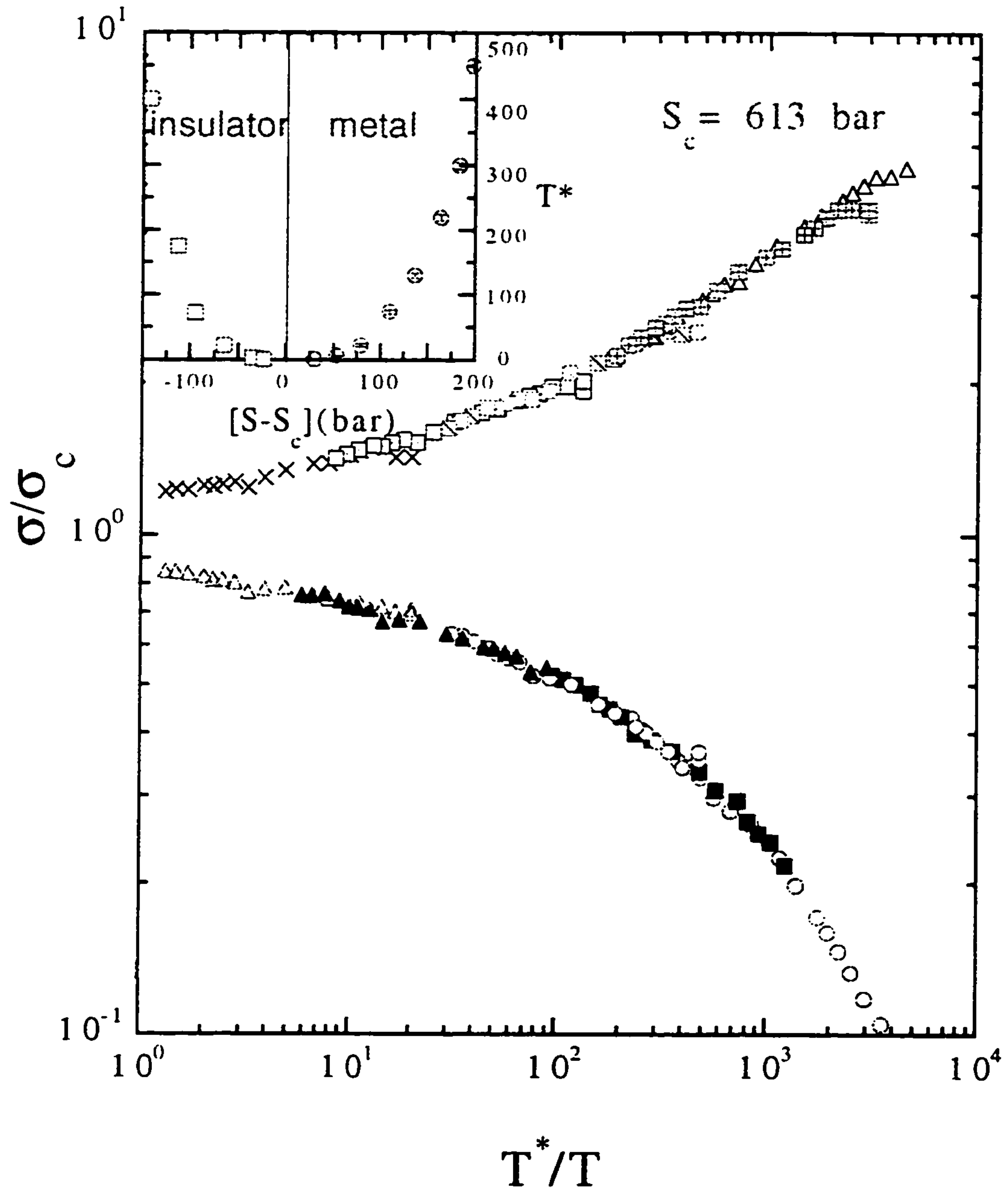

Fig. III-17 Ratio of the conductivity at different value of stress and the critical conductivity at S_c= 613 bar as a function of T*/T. Inset: T* as a function of $|S-S_c|$.

Reproduced with permission of the copyright owner. Further reproduction prohibited without permission.

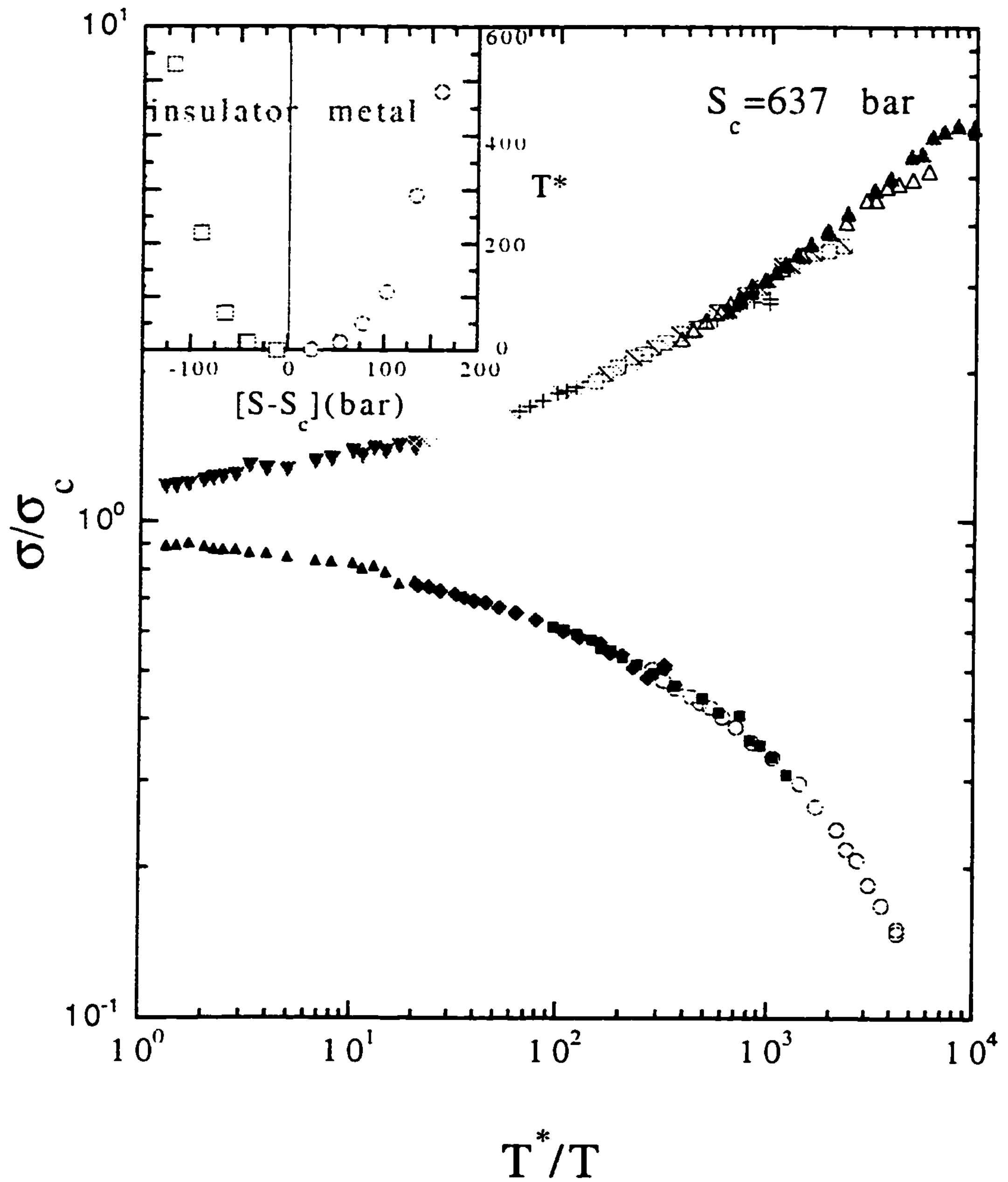

Fig. III-18 Ratio of the conductivity at different value of stress and the critical conductivity at S_c= 637 bar as a function of T*/T. Inset: T* as a function of $|S-S_c|$.

Reproduced with permission of the copyright owner. Further reproduction prohibited without permission.

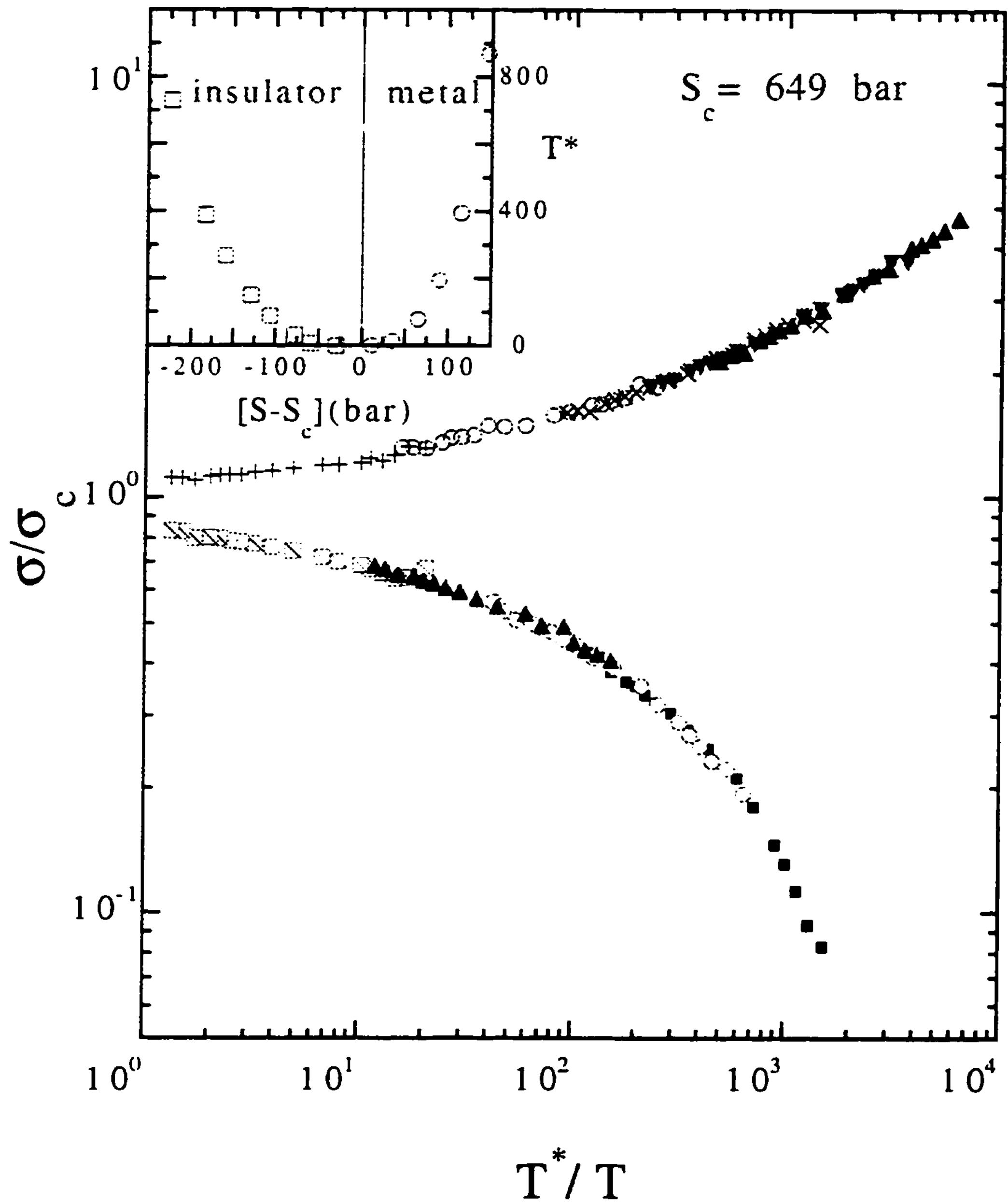

Fig. III-19 Ratio of the conductivity at different value of stress and the critical conductivity at S_c= 649 bar as a function of T*/T. Inset: T* as a function of $|S\text{-}S_c|$.

Reproduced with permission of the copyright owner. Further reproduction prohibited without permission.

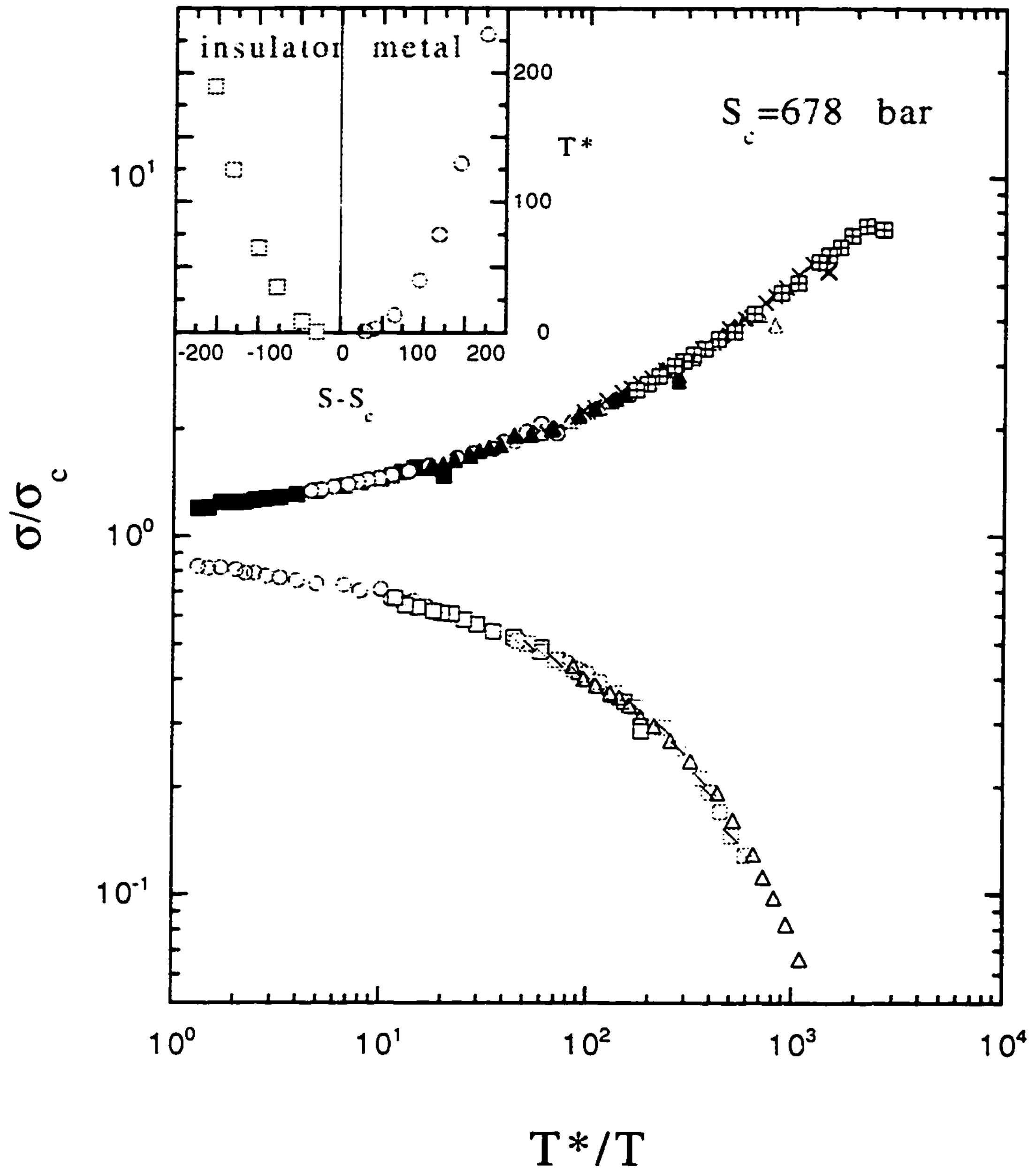

Fig. III-20 Ratio of the conductivity at different value of stress and the critical conductivity at S_c= 678 bar as a function of T*/T. Inset: T* as a function of $|S-S_c|$.

Reproduced with permission of the copyright owner. Further reproduction prohibited without permission.

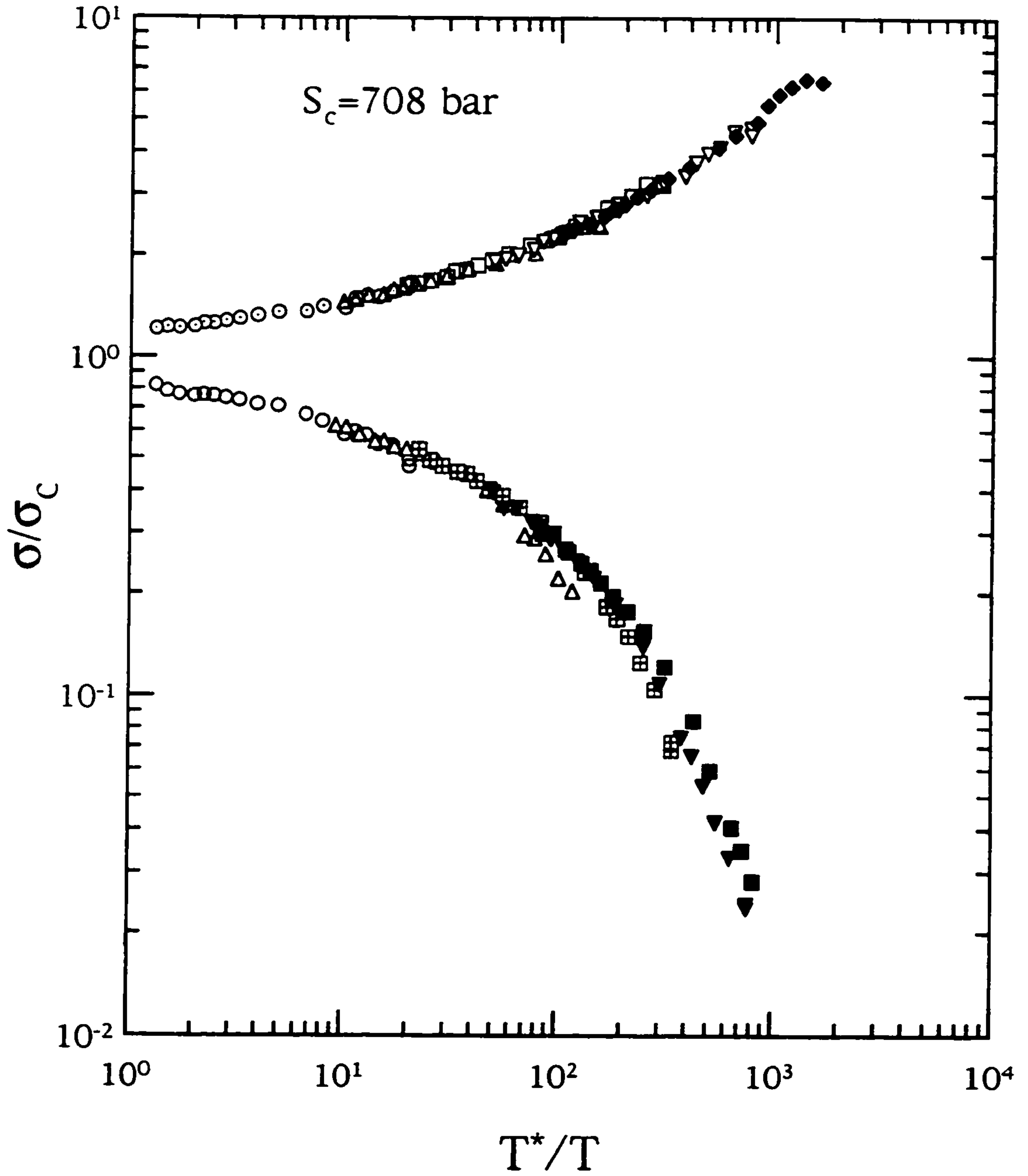

Fig. III-21 Ratio of the conductivity at different value of stress and the critical conductivity at S_c= 708 bar as a function of T*/T.

Reproduced with permission of the copyright owner. Further reproduction prohibited without permission.

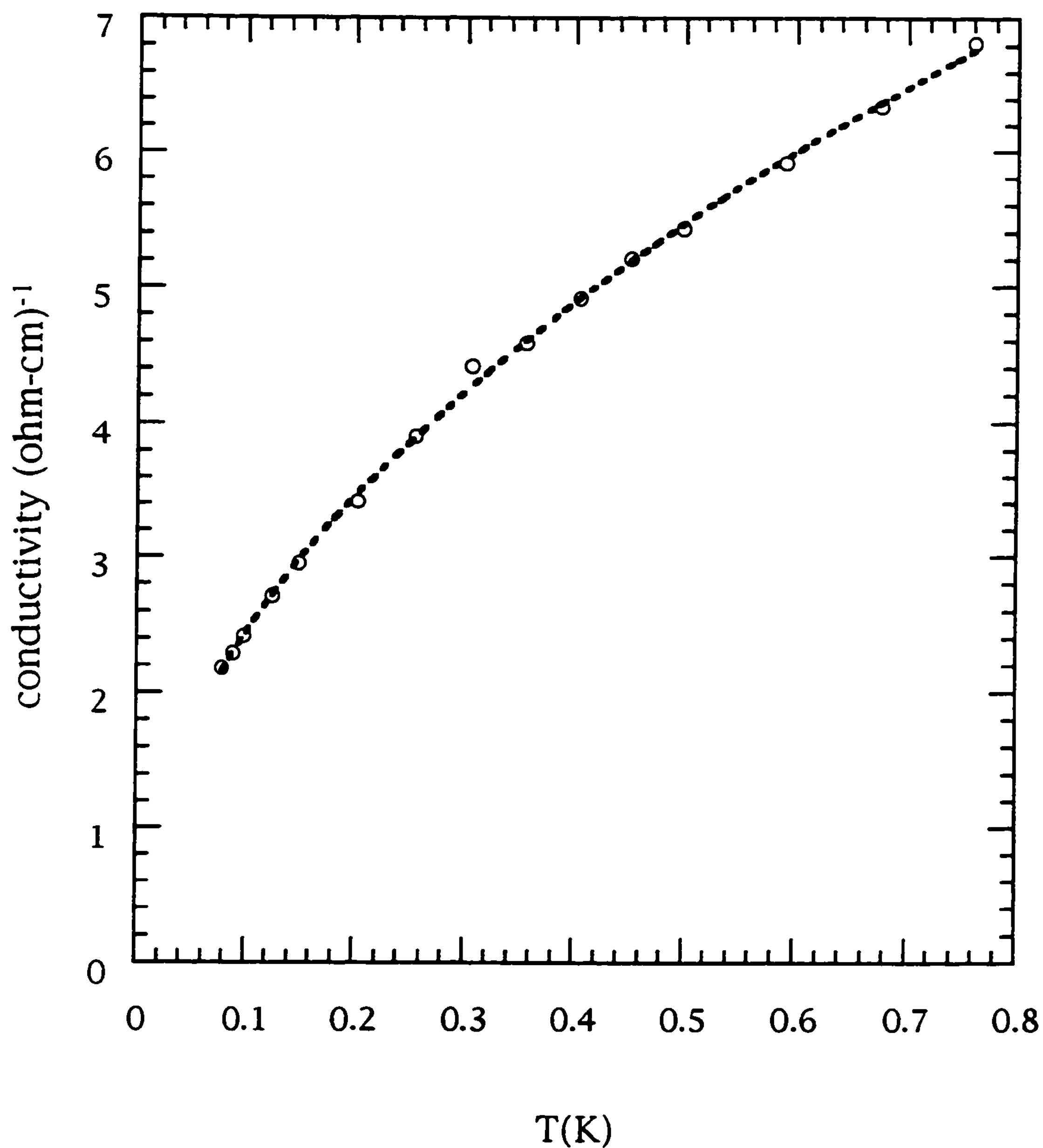

Fig. III-22 Conductivity as a function of temperature for the choice of S_c = 613 bar. Power low fit to the data gives $\sigma_c = AT^{0.5}$

Reproduced with permission of the copyright owner. Further reproduction prohibited without permission.

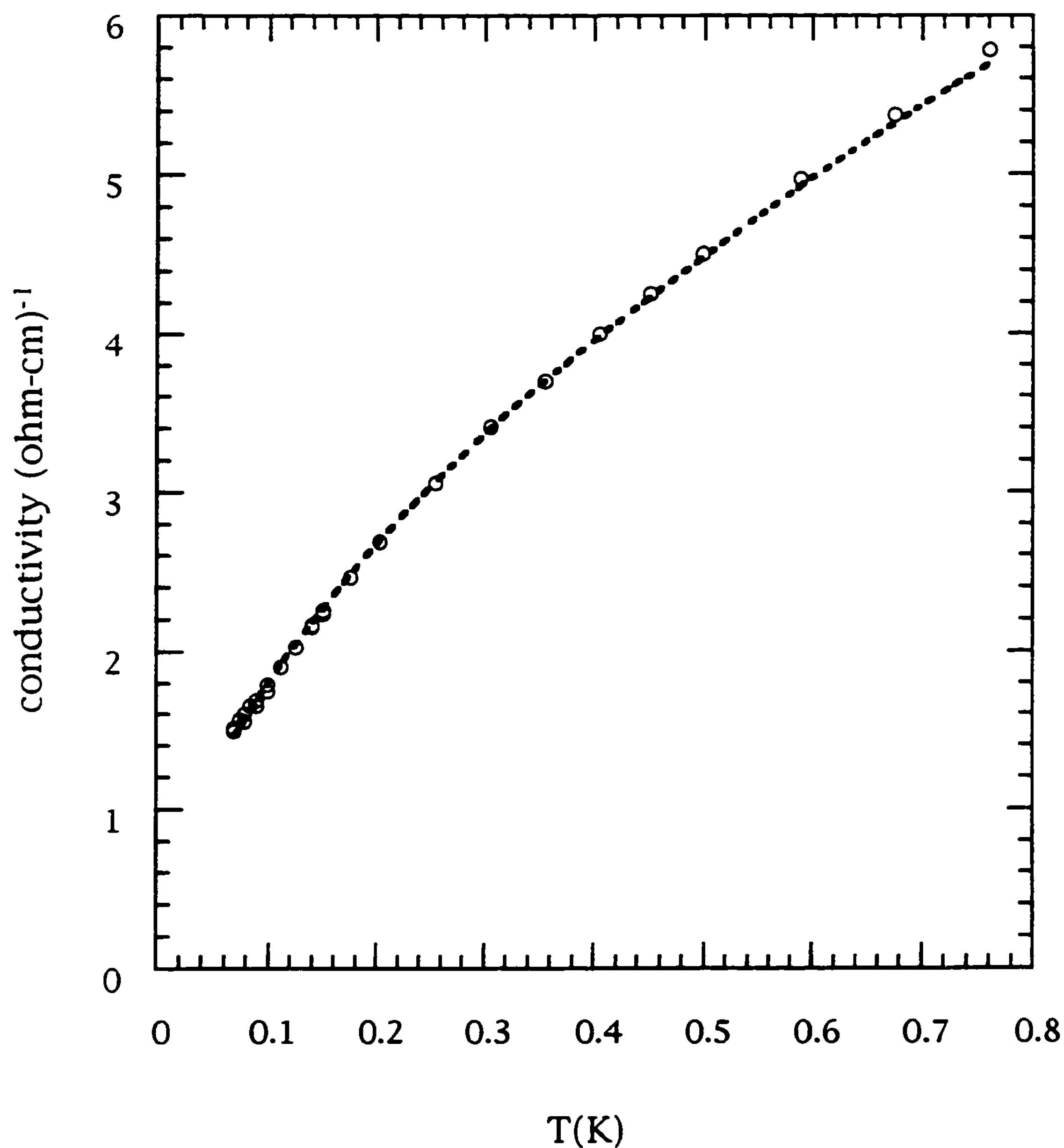

Fig. III-23 Conductivity as a function of temperature for the choice of S_c = 637 bar. Power low fit to the data gives $\sigma_c = AT^{0.57}$

Reproduced with permission of the copyright owner. Further reproduction prohibited without permission.

In the range of critical stress for which there is good scaling, different choices of critical curves $\sigma_c(T,S_c)$ yield the different values of $\mu/\nu z$ and νz, listed in the Table III-C-1 below. For S_c = 650, 637 and 613 bar one gets very similar exponents νz in both, metallic and insulating phase. For the choice of S_c =678 bar the exponent νz obtained for the metallic branch is very different from νz obtained from the insulating branch.

TABLE III-C-1 For different choices of critical stress S_c, the table lists: exponent $\mu/\nu z$ deduced from the temperature dependence of $\sigma_c \propto T^{\mu/z\nu}$, exponent νz from scaling of metallic and insulating branches, average νz, critical conductivity exponent $\mu = (\mu/\nu z) \times (\nu z)$, critical conductivity exponent from zero-T conductivity, and exponent α from critical behavior of T_0.

S_c(bar)	$\mu/\nu z$	νz metal	νz insulator	νz average	$\mu=(\mu/\nu z)$ x(νz)	μ $\sigma \to 0$	α
708		3.1± 0.1				2.5± 0.1	bad fit
678	0.72± 0.01	3.0± 0.1	2.6± 0.2	2.8± 0.2	2.0± 0.2	2.3± 0.05	1.9± 0.1
649	0.62± 0.01	3.0± 0.15	2.9± 0.2	3.0± 0.2	1.9± 0.2	2.1± 0.05	2.3± 0.1
637	0.57± 0.01	3.2± 0.2	3.2± 0.2	3.2± 0.2	1.8± 0.2	1.95±0.1	2.55±0.1
613	**0.50±0.008**	3.2± 0.2	3.2± 0.2	**3.2± 0.2**	**1.6± 0.1**	$1.75\pm^{0.15}_{0.10}$	**2.8± 0.2**
583	0.42± 0.01		3.3± 0.2			1.55± 0.05	3.3± 0.1

The analysis of the data that exhibit insulating behavior in section 3 will show that among the three choices of S_c = 649, 637 and 613 bar the best fits are obtained for S_c close to 613 bar. For S_c =613 bar the critical conductivity behaves as $\sigma_c = A(S_c)T^{1/2}$, and in the analysis of

Reproduced with permission of the copyright owner. Further reproduction prohibited without permission.

critical conductivity behaves as $\sigma_c = A(S_c)T^{1/2}$, and in the analysis of the data in the following section the conductivity of a metal will therefore be plotted as a function of $T^{1/2}$.

2. Metallic conductivity - Critical Behavior

The conductivity of a metal below 500 mK is usually fitted to the form described by equation II-C-1.1, where the $T^{1/2}$ term is due to electron-electron interactions. This equation is derived within the framework of Fermi liquid theory and is expected to be valid outside of the critical region. Since the critical curve has the form $\sigma_c = AT^{1/2}$, this implies that even within the critical region the conductivity has the same $T^{1/2}$ behavior as that due to electron-electron interactions. The conductivity as a function of $T^{1/2}$ at different fixed values of stress is presented in Fig. III-24. The striking feature of the conductivity is the change of the sign of the slope from negative to positive with increasing stress. The change of sign of the slope from negative to positive has also been observed with decreasing dopant concentration or increasing magnetic field as discussed in Chapter II, part C.

On the other hand, detailed comparison of the conductivity at different values of stress with the conductivity without the stress at different dopant concentration, shown in Fig. III-25, clearly indicates different critical behavior with and without stress. Extrapolating the data for metallic samples of Fig. III-24 to zero temperature and omitting low temperature points (associated with thermal decoupling) one obtains values of zero-temperature conductivity at each value of

Reproduced with permission of the copyright owner. Further reproduction prohibited without permission.

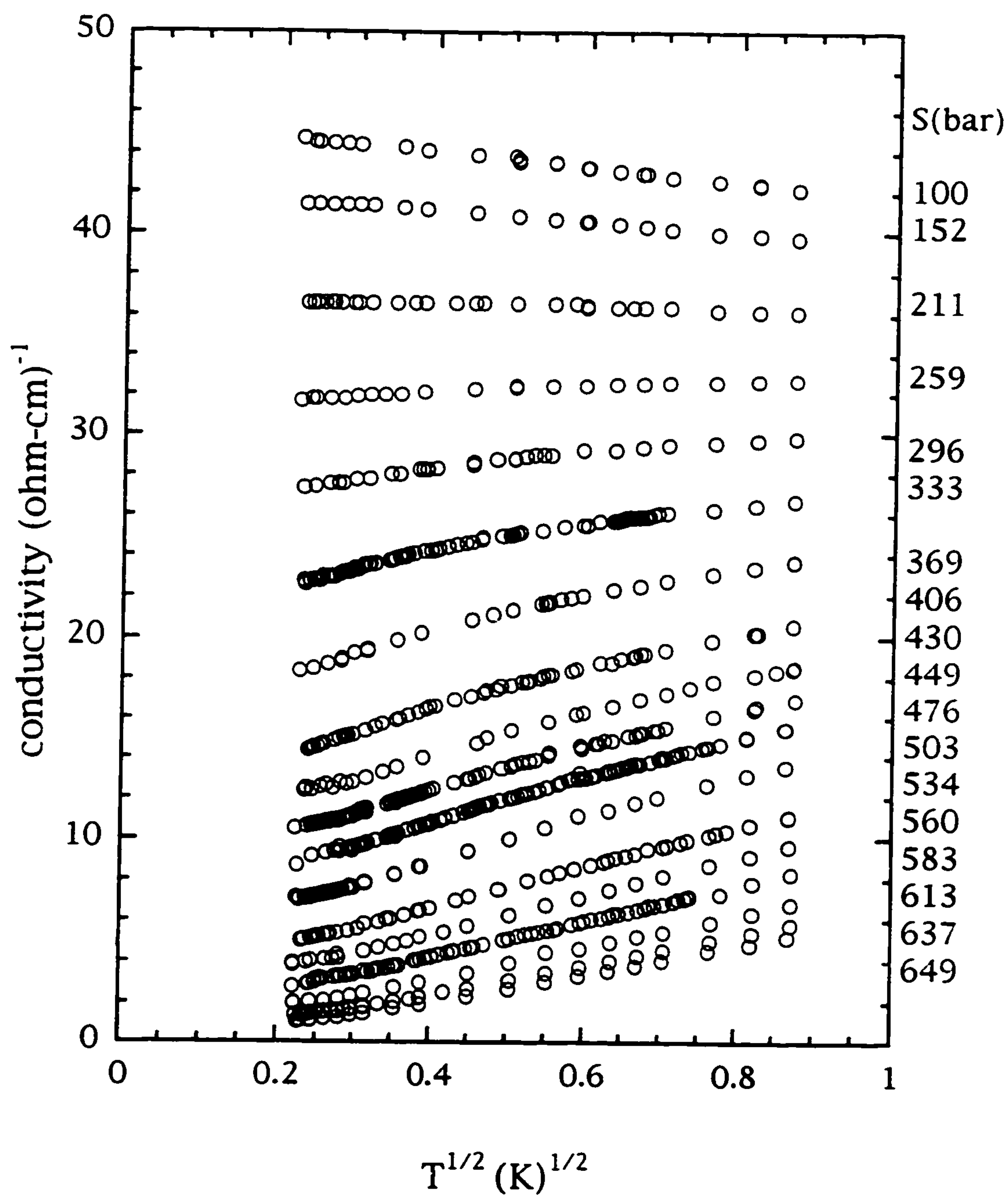

Fig. III-24 Conductivity as a function of $T^{1/2}$ for different values of uniaxial stress as shown.

Reproduced with permission of the copyright owner. Further reproduction prohibited without permission.

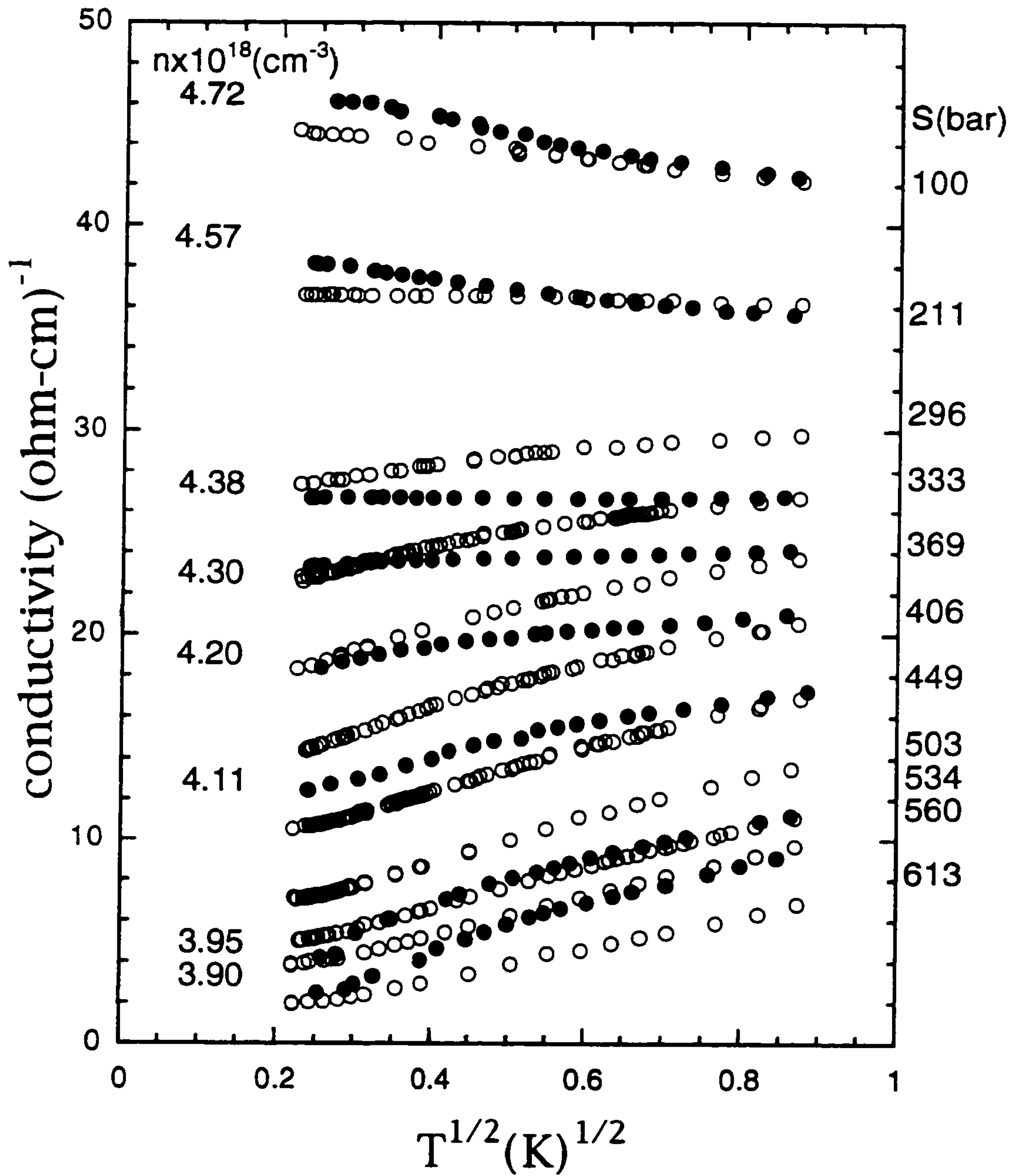

Fig. III-25 Conductivity as a function of $T^{1/2}$ for different values of uniaxial stress; open symbols, and for different values of dopant concentration; solid symbols.

Reproduced with permission of the copyright owner. Further reproduction prohibited without permission.

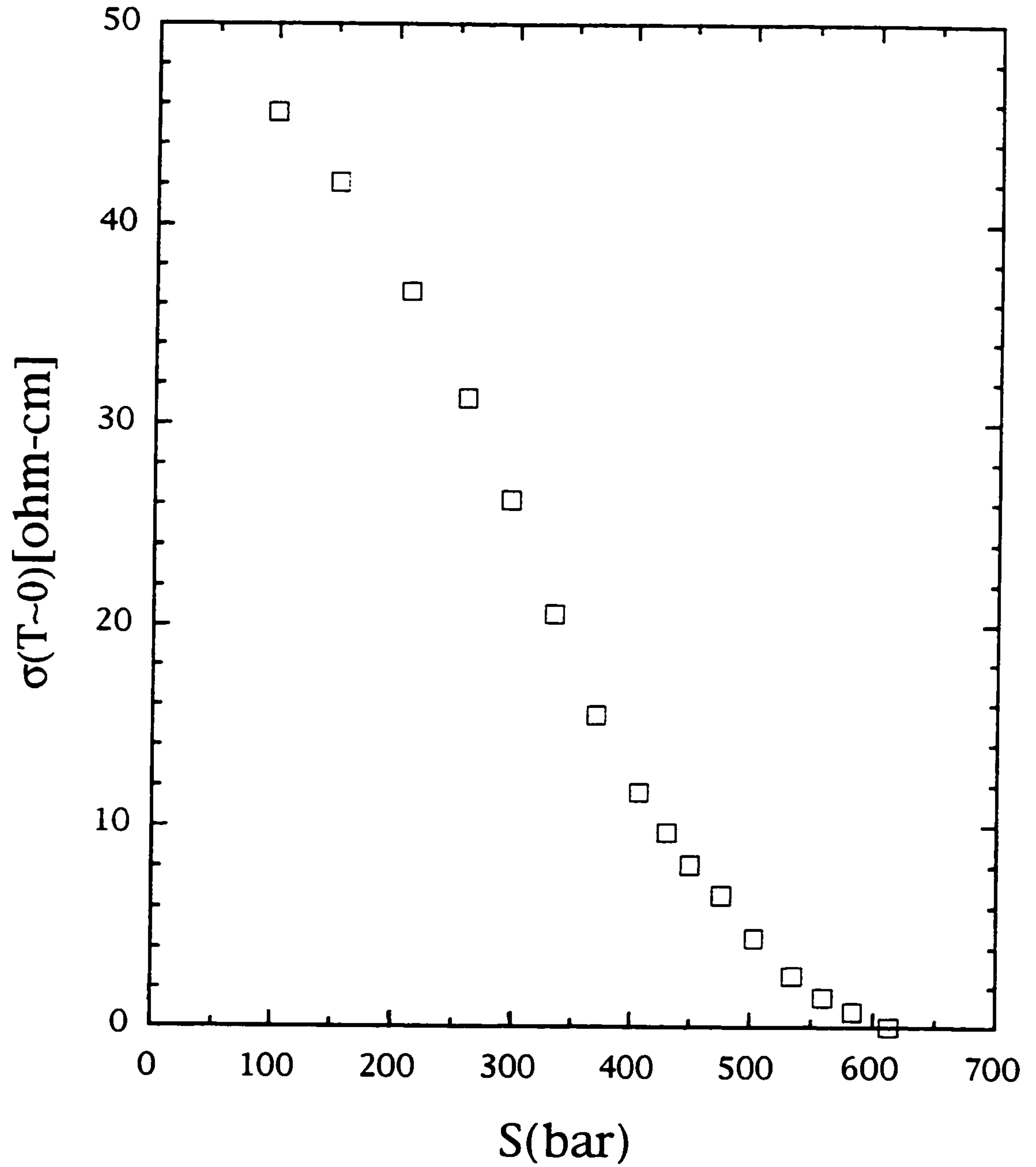

Fig. III-26 Zero-temperature conductivity as a function of stress.

Reproduced with permission of the copyright owner. Further reproduction prohibited without permission.

stress. A plot of the zero-temperature conductivity versus stress is S-shaped and is given in Fig. III-26. Reasonable fits to this curve were possible only for the data extrapolated from the conductivity with the positive slope. Nonlinear least square fits by

$$\sigma = \sigma_0 \left(1 - \frac{S}{S_c}\right)^{\mu} \qquad \text{(III-C-2.1)}$$

to the data above 250 bar for different choices of S_c yield values of exponent μ listed in Table III-C-1. They are in a very good agreement with values of μ obtained from the scaling analysis, where μ = $(\mu/\nu z)$x (νz). For the choice of S_c = 613 bar the parameters σ_0, and μ are listed in Table III-C-2 below, together with the critical parameters obtained for unstressed Si:B by Dai et al[32].

TABLE III-C-2. Critical parameters for Si:B under uniaxial stress and critical parameters obtained by Dai et al.[32] in unstressed Si:B, for a comparison.

METAL			INSULATOR		
Bogdanovich et al.[83] (stressed Si:B)					
S_c [bar]	μ	$\sigma_0[(\Omega cm)^{-1}]$	S_c [bar]	α	A [K]
$613\pm^{20}_{10}$	$1.75\pm^{0.15}_{0.10}$	$81\pm^{5}_{3}$	$613\pm^{20}_{10}$	3.2 ± 0.2	$50\pm^{6}_{3}$
Dai et al[32] (unstressed Si:B)					
$n_c[\times 10^{18} cm^{-3}]$	μ	$\sigma_0[(\Omega cm)^{-1}]$			
$4.06^{+0.12}_{-0.02}$	$0.65^{+0.05}_{-0.14}$	152^{+10}_{-18}			

Reproduced with permission of the copyright owner. Further reproduction prohibited without permission.

It is very striking that in the case of Si:B, μ obtained by varying the stress[82] is almost 3 times bigger than μ obtained by varying the dopant concentration[32]. Such a large value of μ is usually characteristic of a percolation transition ($\mu \approx 2$, see ref. 83) rather than a localization transition. Experimental findings for μ in doped semiconductors are: $\mu < 1$ or $\mu \sim 1$. Recently, a different interpretation of results in Si:P was proposed by Stupp, Von Löhneysen and coworkers[47]. Restricting the critical behavior to the region for which the slope of the conductivity as a function of temperature is positive, they obtain $\mu \approx 1.3$ which is very different from $\mu \approx 0.55$ of Paalanen et al.[3] The critical region for the metal-insulator transition is not known; the critical exponents are often deduced from curves for which the slope of the conductivity as a function of temperature was positive, zero, and negative. One should also note, however, that the two experimental groups used different methods, (see Table III-A) in obtaining the critical conductivity exponents for Si:P. In the experiments of Stupp et al.[47] μ=1.3 was obtained by varying the dopant concentration n, whereas in experiments of Paalanen et al.[3] μ=0.55 was obtained by varying the stress. The results obtained in stressed an unstressed Si:B presented above indicate that these two methods can in fact yield different critical behavior.

It suggests that the stressed tuned metal-insulator transition and concentration driven metal-insulator transition in Si:B may belong to different universality classes.

Reproduced with permission of the copyright owner. Further reproduction prohibited without permission.

3. Approach to the MIT from the Insulating Side

For values of stress greater then S_c it was found that the conductivity obeys Efros-Shklovskii hopping described by formulae (III-A-1.5), rather than Mott variable-range-hopping. With t=S and x=1/2 equation (III-A-1.5) can be written as:

$$\sigma = \sigma_0 \exp\left\{-\left(\frac{T_0}{T}\right)^{1/2}\right\}, \qquad \text{(III-C-3.1)}$$

where σ_0 has a weak temperature dependence that is not known and T_0 is expected to behave critically with stress as given by III-A-1.7:

$$T_0 = A\left(\frac{S}{S_c} - 1\right)^{\alpha}. \qquad \text{(III-C-3.2)}$$

Deep in the insulating phase the ES hopping law described by equation (III-C-3.1) is dominated by the exponential term, so that one can neglect the weak temperature dependence of the prefactor. The logarithm of the conductivity for several different values of stress as a function of $T^{-1/2}$ is presented in Fig. III-27. Data below 0.07 K were excluded from this plot, due to thermal decoupling and conductivities for 874 bar and 832 bar were plotted down to temperatures where the low frequency AC method still yielded reliable results. Linear fits to $\ln(\sigma/\sigma_0) = T_0^{1/2}/T^{1/2}$ gave values of T_0 for different stresses, which were then plotted as a function of stress in Fig. III-28. Deviations from the straight line in Fig. III-27 become

Reproduced with permission of the copyright owner. Further reproduction prohibited without permission.

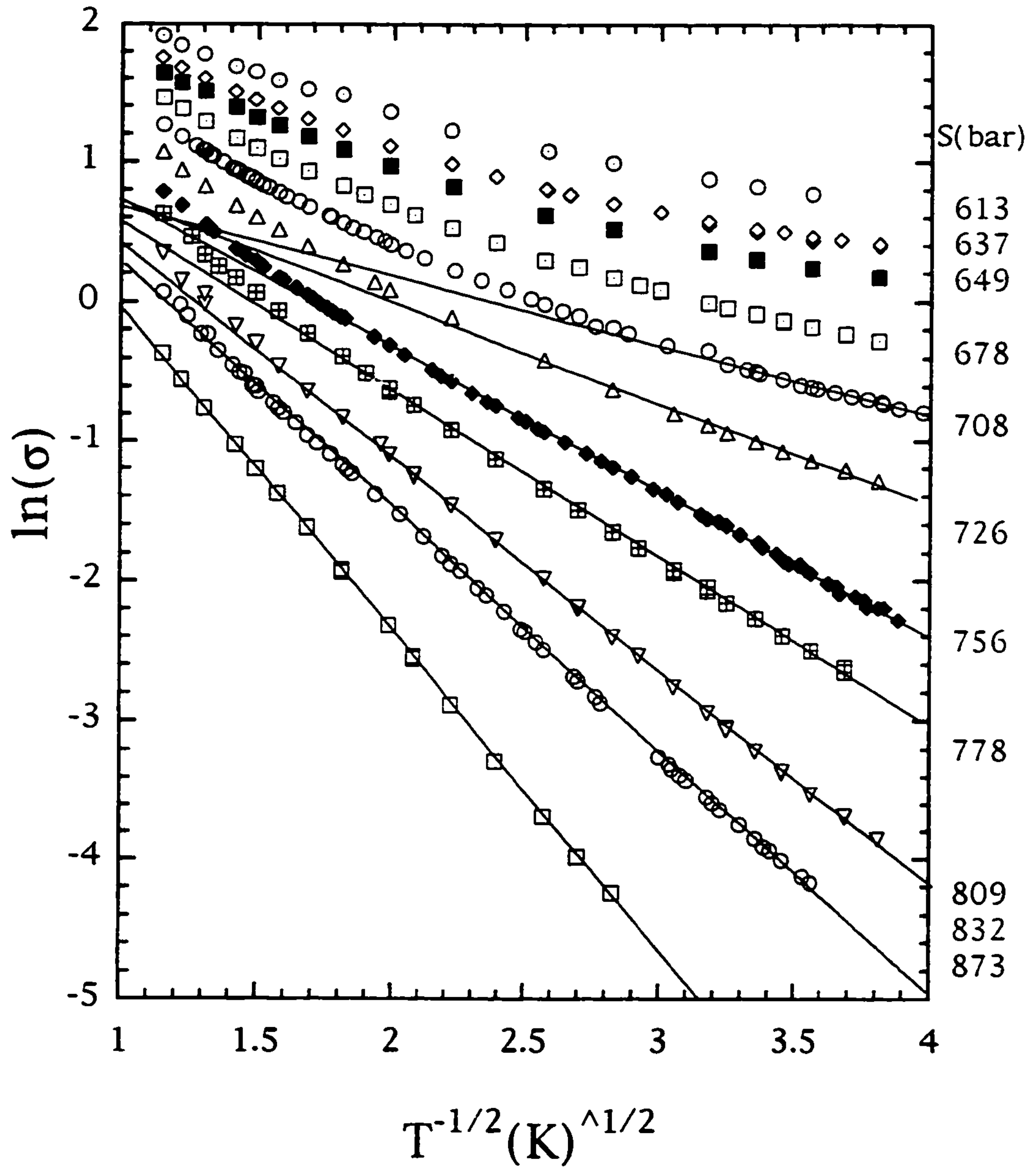

Fig. III-27 lnσ as a function of $T^{-1/2}$ for 11 fixed values of stress.

Reproduced with permission of the copyright owner. Further reproduction prohibited without permission.

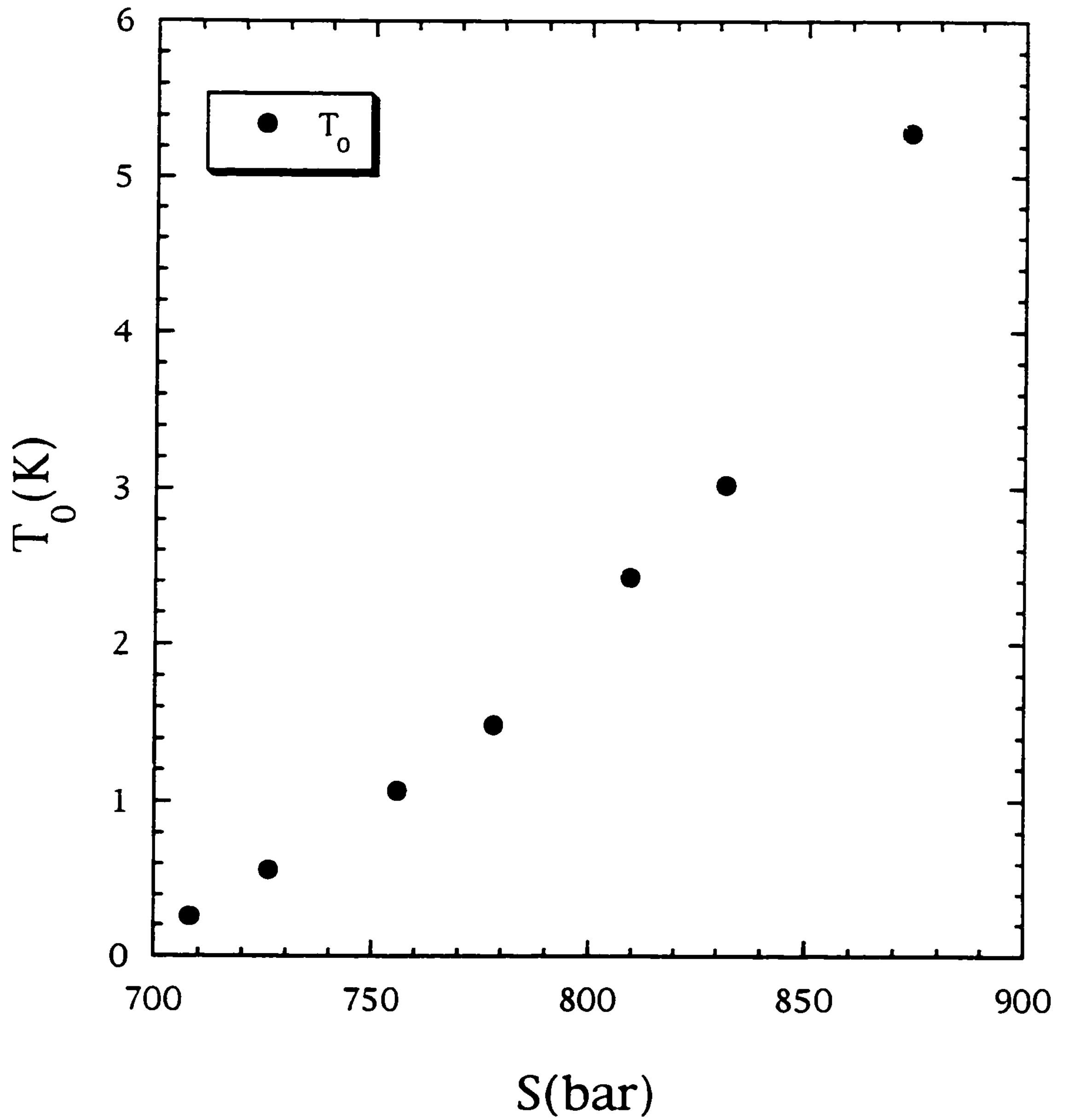

Fig. III-28 T_0 as a function of uniaxial stress S.

Reproduced with permission of the copyright owner. Further reproduction prohibited without permission.

more pronounced as one gets closer to the transition. Power law fits by equation (III-C-3.2) for different choices of critical stress S_c yielded different values of the exponent α presented in Table III-C-1. The exact form of the scaling function for the insulating branch is expected to be Efros-Shklovskii Hopping[44]. Plotting the scaled conductivity of the insulating branch for S_c =613 bar , σ/σ_c as a function of $(T^*/T)^{1/2}$ on a semi-log scale in Fig. III-A-29 gives a straight line for all the values of T^*/T except for $T^*/T < 1$, for which the Coulomb gap energy is of the order of k_BT or less. Here, T^* behaves critically with stress $T^* \propto \delta S^{vz}$, and is equivalent to $T_0 \propto \delta S^{\alpha}$, meaning $\alpha = vz$. For the choice of S_c =649, 637 and 613 bar for which reasonable scaling of data was found, one obtains α between 2.3 and 2.8, whereas vz ranges between 3.0 and 3.2, as shown in Table. III-C-1. The closest agreement is achieved by choosing S_c = 613 bar for which $\alpha = 2.8 \pm 0.2$ and the scaling exponent $vz = 3.2 \pm 0.2$.

Ignoring the temperature dependence of the prefactor σ_0 in the ES hopping formula very near the transition led to an incorrect estimate of the exponent α. One can deduce the exact form of the temperature dependence of the prefactor from the form of the scaling function presented in Fig. III-29. In fact, the temperature dependence of the prefactor is the same as the temperature dependence of the critical conductivity σ_c, namely $\sigma_c \sim T^{1/2}$ for S_c =613 bar. Plotting $(\sigma/\sigma_c)(T^*/T)^y$ as a function of $(T^*/T)^{1/2}$, and allowing y to take on different values to simulate various different temperature dependencies leads to deviations from the straight line (see Fig. III-30). Assuming a different σ_c(corresponding to different S_c) leads to deviations from a straight line. The scaling curve shown in Fig. III-31; σ/σ_c as a func-

Reproduced with permission of the copyright owner. Further reproduction prohibited without permission.

tion of $(T^*/T)^{1/2}$ is plotted at S_c = 637 bar. Downward deviation from the straight line at low temperatures (high $(T^*/T)^{1/2}$), indicate that this is not the right choice of σ_c. One observes similar deviations from a straight line for the choice of σ_c at S_c = 583 bar in Fig. III-32. Note that for S_c = 583 bar the metallic branch does not exhibit good scaling, also indicating that this is not a good choice of S_c. This leads to the conclusion that $S_c = (613\pm^{20}_{10})$ bar is the best choice for the critical stress with $\sigma_c \sim T^{1/2}$ (see Table III-C-1 and Table III-C-2), where the error bars were estimated from the quality of the nonlinear square fits to the zero-temperature conductivity and T* .

Reproduced with permission of the copyright owner. Further reproduction prohibited without permission.

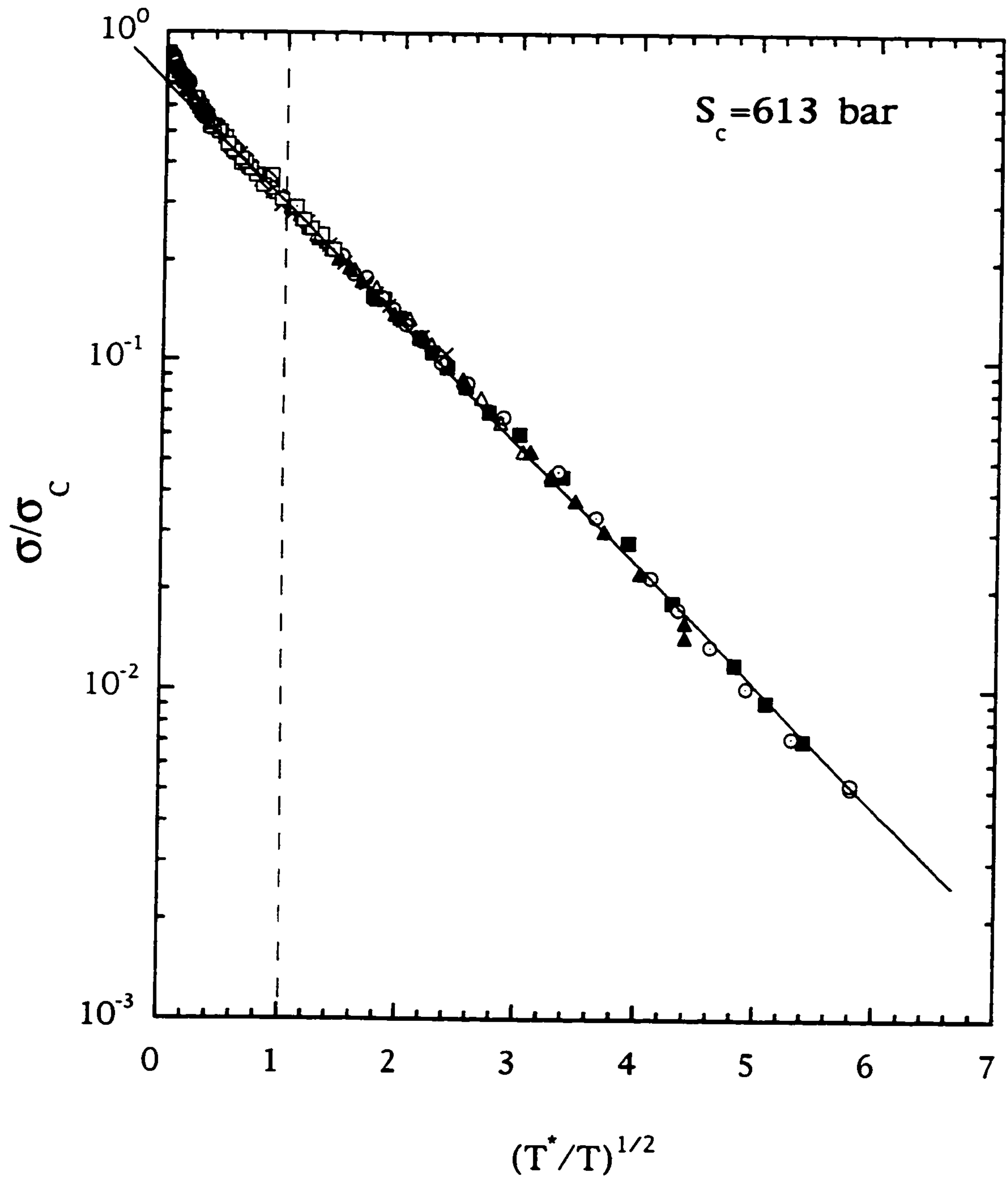

Fig. III-29 Semi-log plot of the ratio of σ/σ_c for S_c =613 bar as a function of $(T^*/T)^{1/2}$.

Reproduced with permission of the copyright owner. Further reproduction prohibited without permission.

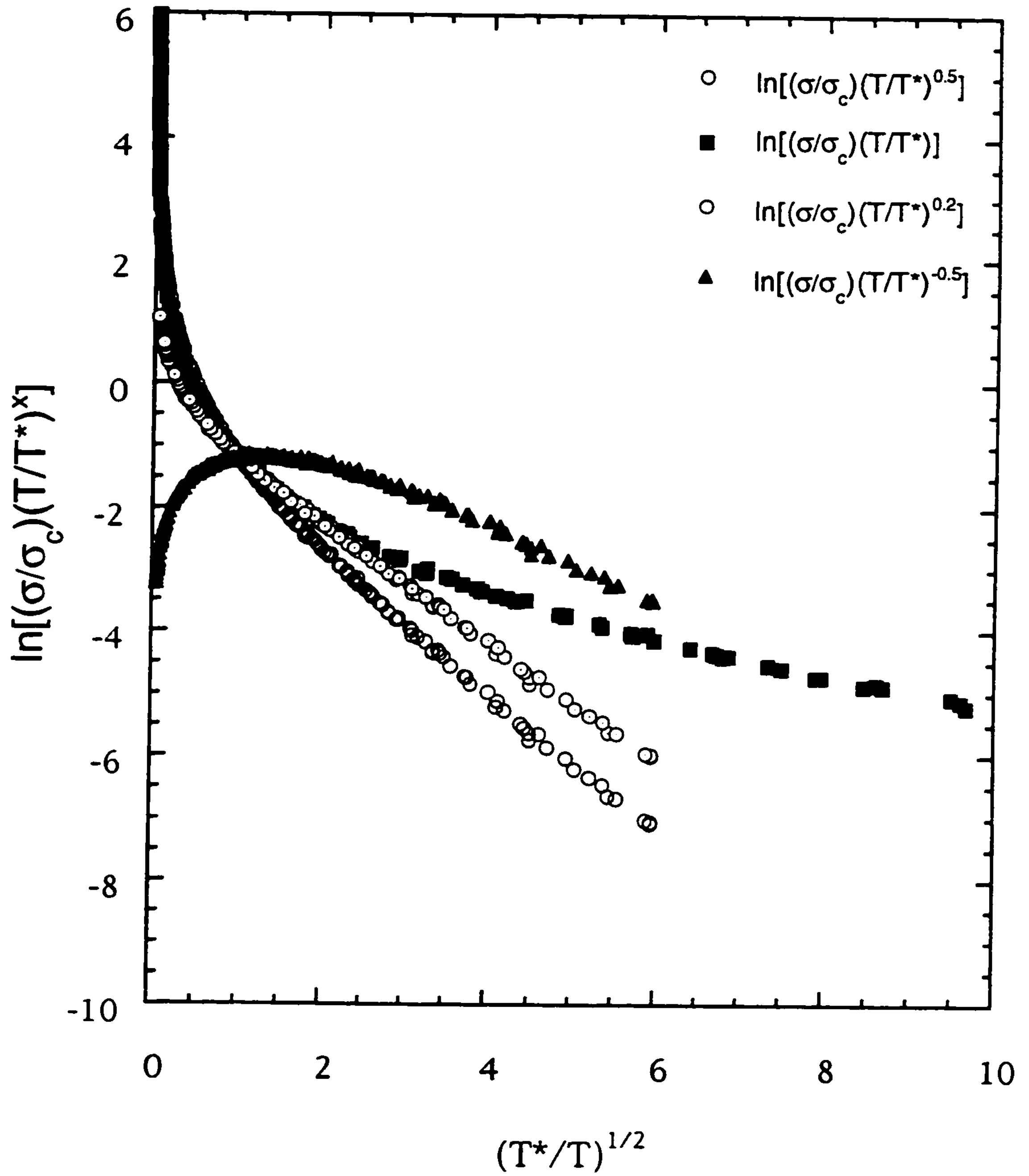

Fig. III-30 $\ln[(\sigma/\sigma_c)(T/T^*)^y]$ for S_c=613 bar and different values of y as a function of $(T^*/T)^{1/2}$.

Reproduced with permission of the copyright owner. Further reproduction prohibited without permission.

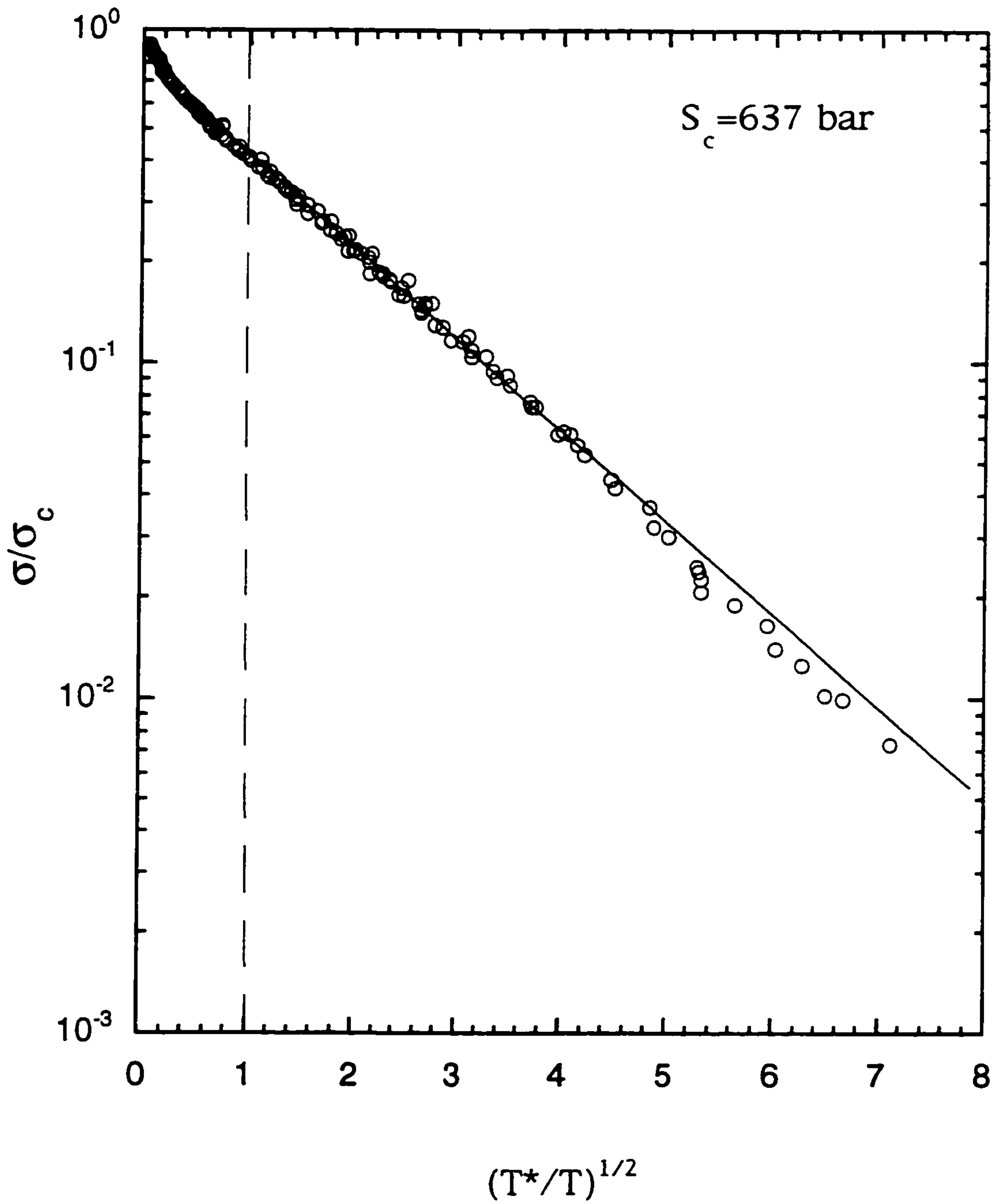

Fig. III-31 Semi-log plot of the ratio of σ/σ_c for S_c=637 bar as a function of $(T^*/T)^{1/2}$.

Reproduced with permission of the copyright owner. Further reproduction prohibited without permission.

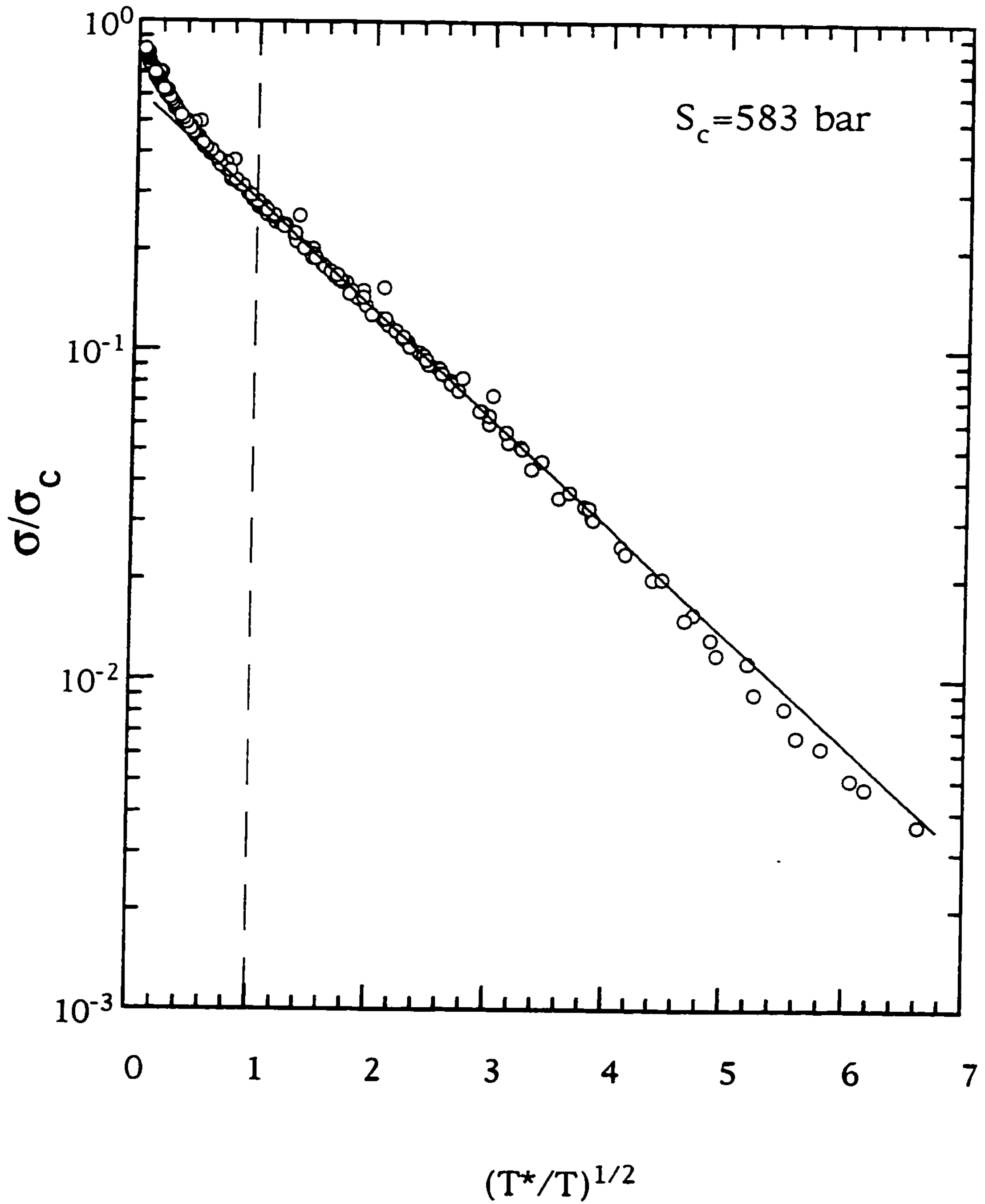

Fig. III-32 Semi-log plot of the ratio of σ/σ_c for S_c=583 bar as a function of $(T^*/T)^{1/2}$.

Reproduced with permission of the copyright owner. Further reproduction prohibited without permission.

This leads to the conclusion that the correct form of the ES law is given by:

$$\sigma(T,S) = BT^{1/2} \exp\left\{-\left(\frac{T_0}{T}\right)^{1/2}\right\}, \qquad \text{(III-C-3.3)}$$

where B depends only on stress. If one plots $\ln(\sigma/T^{1/2})$ as a function of $T^{-1/2}$ at different fixed values of stress as shown in Fig-III-33, instead $\ln\sigma$ versus $T^{-1/2}$ the straight lines through the data are obtained even very near the transition. T_0 obtained in this manner is the equivalent of T^* and the exponent $\alpha = \nu z = 3.2 \pm 0.2$ for $S_c = (613 \pm {}^{20}_{10})$ bar. The parameters obtained by fitting the $T^*(T_0)$ by formula III-C-3.2 are given in Table III-C-2. The critical behavior is given by the curves shown in Fig. III-34, where the zero-temperature conductivity is shown as a function of stress on the metallic side and T^* is shown as a function of stress on the insulating side.

Much smaller values of $\alpha \approx 2$ for Ge:As[84] and $\alpha \approx 1$ for Ge:Ga[39] have been reported for T_0 deduced from ES hopping formulae (III-C-3.1) with temperature-independent prefactor σ_0. Similar analysis of Mott variable range hopping in Si:P and Si:As led to $\alpha \approx 1.7$ for Si:P[85] and $\alpha \approx 2.9$ in Si:As[86], which are all smaller than $\alpha = 3.2$ obtained in this measurement. Large differences in exponents α are consistent with the large differences in exponents $\mu(\nu)$ ($\mu \sim 1/2$ for the systems mentioned above and $\mu \sim 1.75$ for stressed Si:B). One should also note that the assumption of temperature-independent prefactor in hopping can lead to serious underestimation of the exponent α for the data close to the transition.

Reproduced with permission of the copyright owner. Further reproduction prohibited without permission.

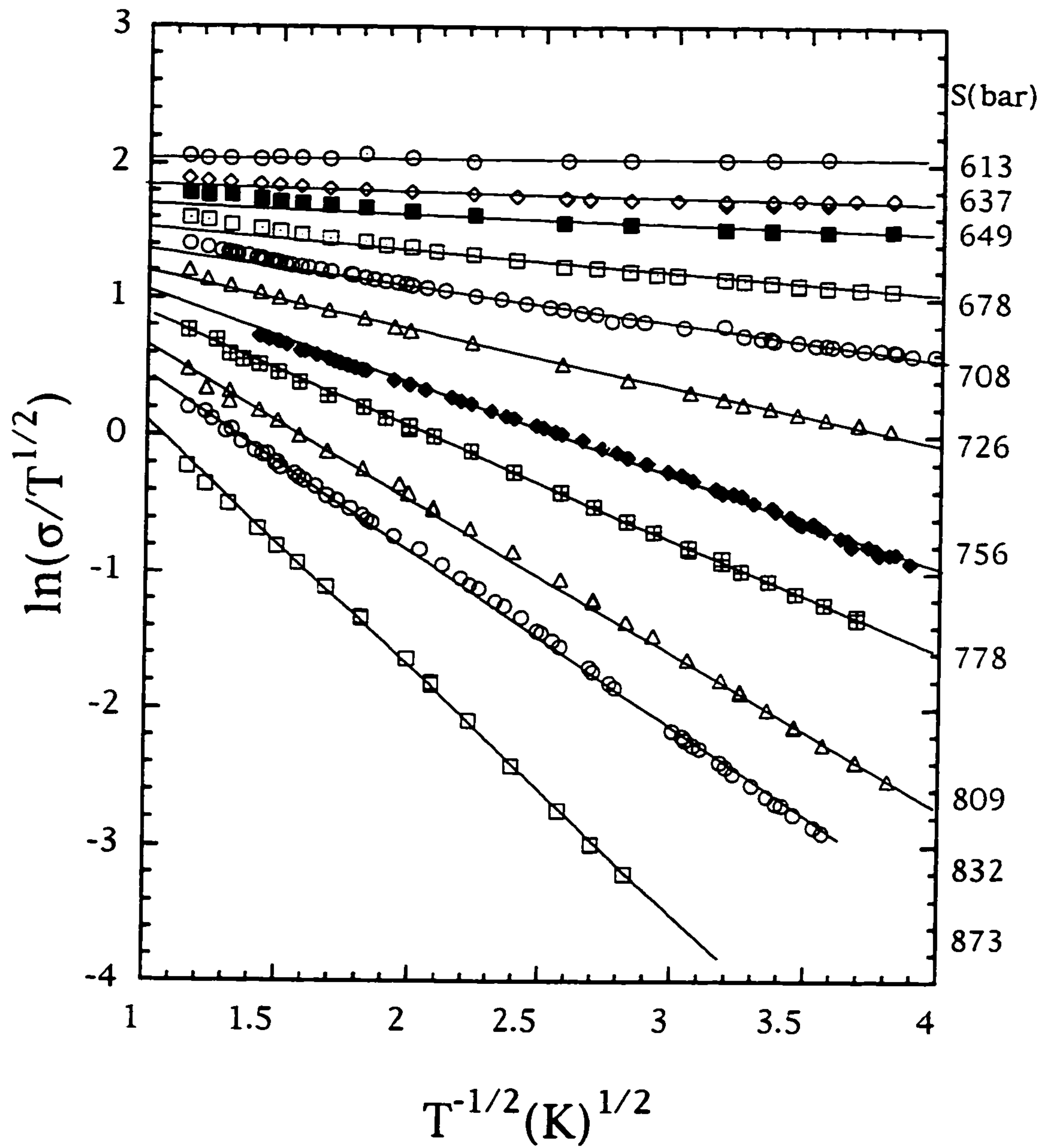

Fig. III-33 ln($\sigma/T^{1/2}$) as a function of $T^{-1/2}$at different values of stress.

Reproduced with permission of the copyright owner. Further reproduction prohibited without permission.

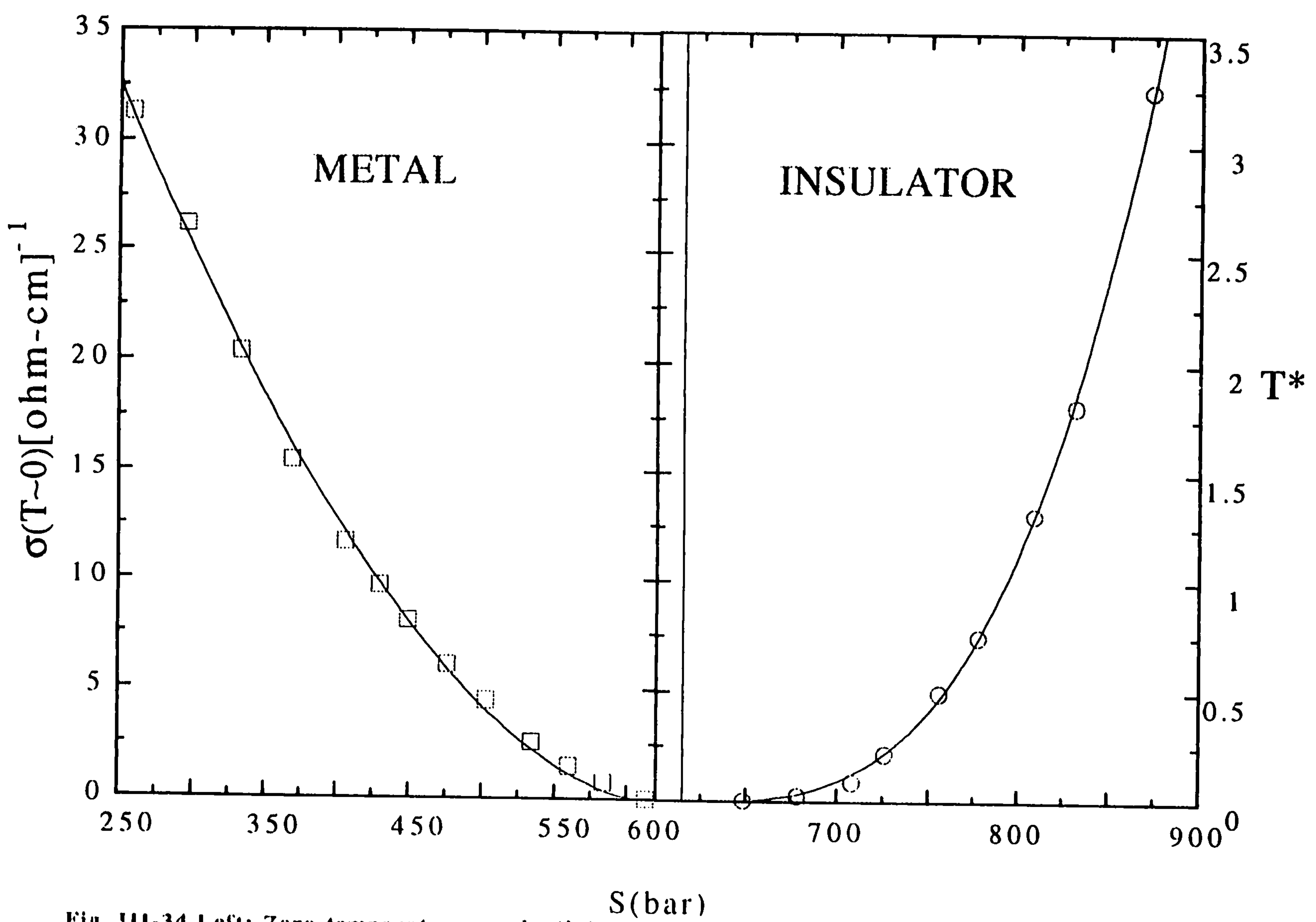

Fig. III-34 Left: Zero-temperature conductivity as a function of stress. Right: T* as a function of stress

Reproduced with permission of the copyright owner. Further reproduction prohibited without permission.

If one assumes that Wegner' s law (III-A-1.3) is valid so that $\nu = \mu = 1.75$ then our experimental finding that $\nu z = 3.2 \pm 0.2$ and $\nu = 1.75^{+0.15}_{-0.10}$ gives a dynamical exponent $z = 1.8 \pm 0.2$. Since, T_0 depends on the dielectric constant κ and the correlation length ξ through relation (III-A-1.6) one can also deduce the critical exponent ζ for the dielectric constant from $\alpha = \zeta + \nu$. Taking $\nu = 1.75$ and $\alpha = 3.2$ one obtains with $\zeta = 1.45 \pm 0.1$.

Measurements of ζ in unstressed Si:P by Capizzi et al.[87] resulted in $\zeta = 1.09 \pm 0.1$ and measurements by Hess et al.[85] gave $\zeta = 1.15 \pm 0.1$. Classical percolation theories give $\zeta \approx 0.6$ or less[88,89] a value that is much smaller than ζ deduced from the above analysis. Independent measurement of ζ would be necessary to determine its value reliably.

SUMMARY

This thesis consists of two parts:

I Magnetoconductivity measurement of Si:B have been carried out in an attempt to separate contributions due to localization and electron-electron interactions. The magnetoconductivity of p-type Si:B was found to be negative for all magnetic fields and temperatures, indicating that both contributions are negative. To separate the two contributions, the conductivity was plotted following the functional form predicted for electron-electron interactions in the particle-hole

Reproduced with permission of the copyright owner. Further reproduction prohibited without permission.

channel $\Delta\sigma = KT^{1/2} f(H/T)$. It was found that the conductivity measured at temperatures between 0.07-0.5 K in magnetic fields from 0 to 9 T collapses onto a single universal curve, as demonstrated in Fig. II-7. This suggests that the metal-insulator transition in Si:B is predominantly driven by electron-electron interactions and that localization, spin-flip scattering and spin-orbit scattering are unimportant despite the strong spin-orbit effects in Si:B. The universal behavior found in this experiment over an appreciable range of concentrations, and broad range of temperatures and magnetic fields indicates that Fermi liquid theory gives a good description of the transport properties of this system.

II A transition from metal to insulator was achieved in a single sample of Si:B with boron concentration $n= 1.2n_c$, by application of compressive uniaxial stress. Increasing stress drives metallic Si:B into the insulating phase by shifting the critical concentration n_c to lower values. The conductivity was measured at temperatures between 0.05 - 0.76 K for different values of stress. It was found that the conductivity of both metal and insulator obeys the dynamical scaling law $\sigma \sim T^{\mu/\nu z} f(\delta S/T^{1/\nu z})$ with the same exponent $\nu z = 3.2 \pm 0.2$ for critical stress $S_c = (613\pm^{20}_{10})$ bar. For this value of stress the temperature dependence of the conductivity has a functional form $\sigma_c = AT^{1/2}$, suggesting that the conductivity in the critical region has the same functional form as the conductivity outside of the critical region, $\sigma(S, T) = \sigma(S,T=0) + A(S)T^{1/2}$ predicted for electron-electron interactions by Fermi liquid theory. The zero-temperature conductivity obtained by extrapolating each curve to zero temperature behaves

Reproduced with permission of the copyright owner. Further reproduction prohibited without permission.

critically as a function of stress, as described by equation (III-C-2.1). For S_c chosen at 613 bar, the critical conductivity exponent is $\mu = 1.75\pm^{0.15}_{0.10}$ which is in good agreement with $\mu = 1.6 \pm 0.1$ obtained from the scaling analysis. The value of the critical conductivity exponent obtained in this measurement is almost three times bigger than μ=0.65 obtained for unstressed Si:B. Detailed comparison of the temperature dependence of the conductivity for different values of stress and conductivity for different dopant concentration without stress indicates different critical behavior of the conductivity with and without stress.

The conductivity behavior found in the insulating phase follows Efros-Shklovskii hopping with a temperature-dependent prefactor, described by equation (III-C-3.3). The usual analysis of data by fitting to the ES law with a temperature-independent prefactor σ_0 leads to incorrect value of the exponent α that does not satisfy $\nu z = \alpha$. The temperature dependence of the prefactor σ_0 is that of the critical conductivity, namely, $\sigma_0 = \sigma_c \sim T^{1/2}$ at S_c=613 bar. With the correct form of the ES law one obtains an exponent $\alpha = \nu z = 3.2 \pm 0.2$ for $S_c = (613\pm^{20}_{10})$ bar. With the assumption that $\mu = \nu$, one obtains a dynamical exponent $z = 1.8 \pm 0.2$. Since $\alpha = \nu + \zeta$, one can estimate the value of the exponent ζ that describes the critical behavior of the dielectric constant, taking $\nu = \mu = 1.75$. The estimated value of $\zeta = 1.45 \pm 0.1$ is larger than $\zeta \sim 1$ obtained for Si:P , and considerably larger than $\zeta \sim 0.6$ predicted for a percolation transition.

In conclusion, the observed critical behavior of the conductivity of Si:B under stress may indicate a universality class different from

Reproduced with permission of the copyright owner. Further reproduction prohibited without permission.

the conductivity under stress suggests the importance of electron-electron interactions and, together with a large value of ζ, excludes the possibility of a percolation transition.

Suggestions for Future Work

Magnetoconductivity-H/T Scaling

H/T scaling of the magnetoconductivity is a useful method for determining the relative importance of localization and electron-electron interactions in other doped semiconductors. Universal scaling observed in Si:B gives evidence for the validity of Fermi liquid theory and merits further investigation. The important question is then, under what conditions one should see the breakdown of the Fermi liquid concept? The magnetoconductivity of Si:B for high magnetic fields $H >> 1T$, follows $\Delta\sigma \sim \sqrt{H}$ as predicted by Fermi liquid theory, whereas recent measurements of magnetoconductivity of Si:P[90] showed $\Delta\sigma \sim H$, indicating that for $H >> (n-n_c)$ one might be inside the critical region where non-Fermi liquid behavior takes over.

Stress tuning the transition in different samples

Stress tuning of the transition in several samples with different dopant concentration n should yield information on how $\delta n = n-n_c$

Reproduced with permission of the copyright owner. Further reproduction prohibited without permission.

scales with $\delta S = S - S_c$, and if the results obtained in this measurement are sample dependent.

The dielectric constant

Studies on Si:P[85], and Si:As[86] have shown that the dielectric constant exhibits critical behavior with an exponent ζ which is twice that of the conductivity μ and in CdSe:In[91] it was found that $\zeta \approx \mu$. Similarly, measurements of the dielectric constant of Si:B as function of stress can be performed to obtain the critical exponent ζ. This would also allow one to check the validity of Wegner's law (if $\nu = \mu$), since ν can be deduced from $\nu = \alpha - \zeta$.

Reproduced with permission of the copyright owner. Further reproduction prohibited without permission.

References

1. N. F. Mott, Can. J. Phys. **34**, 1356(1956); Phil. Mag.**6**, 287 (1961); J. Hibbard, Prog. R. Soc. A(London) **276**, 238 (1963); ibid. **277**, 237 (1964); ibid. **281**, 401 (1964)

2. P.V. Anderson, Phys. Rev. **102**, 1008 (1958)

3. M. A. Paalanen, T. F. Rosenbaum, G.A. Thomas, and R. N. Bhatt, Phys. Rev. Lett. **48**, 1284 (1982)

4. For arguments in favor of a first order transition see, for example, A. Mobius, Phys. Rev.B **40**, 4194 (1989); J. Phys. C **18**, 4639 (1985); A. Mobius, D. Elefant, A. Heinrich, R. Muller, J. Schumann, H. Vinzelberg, and G. Zies, ibid. **16**, 6491 (1983); A. Mobius, H. Vinzelberg, C. Gladun, A.Henrich, D. Elefant, J. Schumann, and G. Zies, ibid. **18**, 3337 (1985).

5. J. T. Edwards, D. J. Thouless, J. Phys. C 5, 807 (1977), D. J. Thouless, Phys. Rep. **13**, 93 (1974)

6. F. Wegner, Z. Phys.B **25**, 327 (1976)

7. E. Abrahams, P. W. Anderson, D. C. Licciardello, T. V. Ramakrishnan, Phys. Rev. Lett. **42**, 673 (1979)

Reproduced with permission of the copyright owner. Further reproduction prohibited without permission.

8. For a review on metal-insulator transition and literature on magnetoresistance, see P. A. Lee, and T. B. Ramakrishnan, Rev. Mod. Phys. **57**, 287 (1985).

9. G. Bergmann, Phys. Reports **107**, 1 (1984)

10. B. L. Altshuler and A. G. Aronov, Zh. Eksp. Teor. Fiz. **77**, 2028 (1979) [Sov. Phys. JETP **50**, 968 (1979)].

11. B. L. Altshuler and A. G. Aronov, Pisma Zh. Eksp. Teor. Fiz. **30**, 514 (1979) [JETP Lett. **30**, 514 (1979)].

12. B. L. Altshuler and A. G. Aronov, Solid State Commun., **46**, 429 (1983).

13. R. N . Bhatt and P. A. Lee, Solid State Commun. **48**, 755 (1983).

14. S. Bogdanovich, Peihua Dai, M. P. Sarachik, and V. Dobrosavljevic, Phys. Rev. Lett. **74**. 2543 (1995).

15. B. L. Altshuler, D. E. Khmelinitskii, A. I. Larkin, and P. A. Lee, Phys. Rev. B **22**, 5142 (1980).

16. A. Kawabata, J. Phys. Soc. Jpn. **50**, 2461 (1981).

17. P. A. Lee, and T. B. Ramakrishnan, Phys. Rev. B **26**, 4009 (1982).

Reproduced with permission of the copyright owner. Further reproduction prohibited without permission.

18. B. L. Altshuler, A. G. Aronov, A. I. Larkin, and D. E. Khmelinitskii, Zh. Eksp. Teor. Fiz. **81**, 768 [Sov. Phys. - JETP **54**, 411 (1981)].

19. R. J. Elliot, Phys. Rev. **96**, 266 (1954).

20. A. Kawabata, J. Phys. Soc. Jpn. **55**, 3299 (1986) and referencies therein; J. Phys. Soc. Jpn. Suppl. A **49**, 375 (1980).

21. B. L. Altshuler, A. G. Aronov, *Electron-Electron interactions in Disordered systems*, edited by A. L. Efros and M. Pollak (North Holland, Amsterdam, 1985), p.1.

22. A. Kawabata, Solid State Commun., **34**, 431 (1980).

23. See G. Bermann, Phys Rev. B **28**, 2914 (1983); T. A. Polyanskaya and I. I. Saidashev, Pisma Zh. Eksp. Teor. Fiz. **34**, 378 (1981) [JETP Lett. **34**, 361 (1981)]; T. Y. Bilgildeyeva, V. N. Karayev, and T. A. Polyanskaya, Fiz. Tekh. Poluprovodn. **22**, 235 (1988) [Sov. Phys. Semicond. **22**, 235 (1988)]; R. C. Dynes, T.H. Geballe, G. W. Hull, Jr., and J. P. Garno, Phys. Rev. B **27**, 5188 (1983).

24. T. F. Rosenbaum, R. F. Milligan, G. A. Thomas, P. A. Lee, T. V. Ramakrishnan, and R. N. Bhatt, Phys. Rev. Lett. **47**, 1758 (1981).

25. Peihua Dai, Youzhu Zhang, and M. P. Sarachik, Phys. Rev. B **45**, 3984, (1992).

Reproduced with permission of the copyright owner. Further reproduction prohibited without permission.

26. Peihua Dai, Youzhu Zhang, and M. P. Sarachik, Phys. Rev. B **46**, 6724, (1992).

27. Peihua Dai, Thesis, City University of New York, New York, U.S.A., (1991).

28. F. A. Trumbore, BellSyst. Tech. J. **39**, 205 (1960).

29. R. J. Capik (unpublished)

30. L. J. van der Pauw, Phillips, Res. Rep. **13**, 1 (1958).

31. W. R. Thurber, R. L. Mattis, Y. M. Liu, J.J. Filiben, J. Electrochem. Soc. **127**, 2291, (1980).

32. Peihua Dai, Youzhu Zhang, and M. P. Sarachik, Phys. Rev. Lett. **66**, 1914, (1991).

33. O. V. Lounasmaa, *Experimental Principles and Methods Below 1K*, (Academic Press Limited, London, 1974).

34. R. B. Richardson, E. N. Smith, *Experimental Techniques in Condense Matter Physics at Low Temperatures*, (Addison Wesley, 1988)

35. T. F. Rosenbaum, R. F. Milligan, M. A. Paalanen, G. A. Thomas, R. N. Bhatt,and W. Lin, Phys. Rev. B **27**, 7509 (1983).

Reproduced with permission of the copyright owner. Further reproduction prohibited without permission.

36. W. N. Shafarman, D. W. Koon, and T. G. Castner, Phys. Rev. B **40**, 1216 (1989).

37. M.J. Hirsh and D. F. Holcomb, in *Disordered Semiconductors*, edited by M. A. Kastner, G. A. Thomas, and S. R. Ovshinsky (Plenum, New York, 1987), p.45.

38. G. A. Thomas, A. Kawabata, Y. Ootuka, S. Katsumoto, S. Kobayashi, and W. Sasaki, Phys. Rev. B **26**, 2113 (1982).

39. K. M. Itoh, E. E. Haller, J. W. Beeman, W. L. Hansen, J. Emes, L.A. Reichertz, E. Kreysa, T. Shutt, A. Cummings, W. Stockwell, B. Sadoulet, J. Muto, J. W. Farmer, and V.I. Ozhogin, Phys. Rev. Lett. **77**, 4058 (1996).

40. V. Dobrosavljevic and G. Kotliar (upublished).

41. See Rev. of Mod. Phys. **66**, 261 (1994) by D. Belitz and T. R. Kirkpatrick, and the referencies therein.

42. J. Chayes, L. Chayes, D. S. Fisher, and T. Spenser, Phys. Rev. Lett. **57**, 2999 (1986).

43. T. R. Kirkpatrick and D. Belitz, Phys. Rev. B **41**, 11082 (1990).

44. B. I. Shklovskii and A. L. Efros, *Electronic Properties of Doped Semiconductors*, Solid State Serias Vol. **45** (Spring-Verlag, Berlin, Heidelberg, 1984).

Reproduced with permission of the copyright owner. Further reproduction prohibited without permission.

45. A. M. Finkelshtein, Zh. Eksp. Teor. Fiz. 84, 168 (1983)[Sov. Phys. JETP **57**, 97 (1983)].

46. C. Castellani, G. Kotliar, and P. A. Lee, Phys. Rev. Lett. **59**, 323 (1987).

47. H. Stupp, M. Hornung, M. Lakner, O Madel, and H. v. Lohneysen, Phys. Rev. Lett. **71**, 2634 (1993).

48. P. F. Newman and D. F. Holcomb, Phys. Rev. B **28**, 638 (1983); D. W. Koon and T. G. Castner, Phys. Rev. B **40**, 1216 (1989).

49. A. P. Long and M. Papper, J. Phys. C **17**, L425 (1984); Solid State Electron. **28**, 61 (1985).

50. P. F. Newman and D. F. Holcomb, Phys. Rev. Lett. **51**, 2144 (1983).

51. A. N. Ionov, M. J. Lea, and R. Rentzsch, Pisma Zh. Eksp. Teor. Fiz. **54**, 470 (1991)[JETP Lett. **54**, 473 (1991)]

52. Y. Ootuka, H. Matsuoka and S. Kobayashi, in *Anderson Localization*, edited by T. Ando and H. Fukuyama (Spring-Verlag, Berlin, 1988), p.40.

53. G. A. Thomas, A. Kawabata, Y. Ootuka, S. Katsumoto, S. Kobayashi, and W. Sasaki, Phys. Rev. B **25**, 4288 (1982).

Reproduced with permission of the copyright owner. Further reproduction prohibited without permission.

54. M. J. Hirsch, U. Thomanschefsky, and D. F. Holcomb, Phys. Rev. B **37**, 8257 (1988).

55. A. G. Zabrodskii and K. N. Zinov'eva, Zh. Eksp. Teor. Fiz. **86**, 727 (1984) [Sov. Phys.-JETP **59**, 425 (1984)].

56. For a review, see G. A. Thomas, in *Localization and Interaction*, D. M. Finalayson, ed. p. 29 (The Scottish University Summer School in Physics, St Andrews, 1986), p. 172, and referencies therein; Phil. Mag. B **52**, 479 (1985).

57. H. Fritzsche, Phys. Rev. **125**, 1560 (1962).

58. F. Bassani, G. Iadonisi, and B. Preziosi, Rep. Prog. Phys. **37**, 1099 (1974).

59. W. Kohn, *Shallow impurity states in silicon and germanium*, Solid State Physics **5**, New York (1957).

60. For detailed derivations of electronic levels in periodic potential, see *Solid State Physics*, N. W. Ashcroft and N. D. Mermin, ed p.131 (Sunders College Publishing, Philadelphia, 1976).

61. J. M. Luttinger and W. Kohn, Phys. Rev. **97**, 869 (1955).

62. G. Dresselhaus, A. F. Kip, and C. Kittel, Phys. Rev. **98**, 368 (1955).

Reproduced with permission of the copyright owner. Further reproduction prohibited without permission.

63. W. Kohn, J. M. Luttinger , Phys. Rev. **98**, 915 (1955).

64. N. F. Mott, *Metal-Insulator Transitions*, p. 133 (Taylor & Francis Ltd., London, 1974).

65. R. N. Bhatt, Phys. Rev B **24**, 3630 (1981).

66. R. N. Bhatt, Phys. Rev B **26**, 1082 (1982).

67. H. Fritzsche, Phys. Rev. **125**, 1552 (1962).

68. G. L. Bir and G. E. Pikus, *Symmetry and Strain-Induced Effects in Semiconductors*, p. 214 (John Wiley, New York, 1974).

69. S. Zwerdling, K. Button, B. Lax, and L. M. Roth, Phys. Rev. Lett. **4**, 173 (1960).

70. A. Kahn, Phys. Rev. **97**, 1647 (1955).

71. J. C. Hensel and G. Feher, Phys. Rev. **129**, 1041 (1963).

72. W. Kohn, *Solid State Physics*,edited by F. Seitz and D. Turnbull (Academic Press Inc., New York, 1957), Vol. **5**, p.257.

73. W. Kohn and D. Schechter, Phys. Rev. **99**, 1903 (1955).

74. D. Schechter, J. Phys. Chem. Solids **23**, 237 (1962).

Reproduced with permission of the copyright owner. Further reproduction prohibited without permission.

75. A. Baldereschi and N. O. Lipari, Phys. Rev. B **8**, 2697 (1973).

76. K. S. Mendelson and D. R. Schultz, Phys. State. Sol. **31,** 59 (1968).

77. J. A. Chroboczek, F. H. Pollak, and H. F. Staunton, Phil. Mag. B **50**, 113 (1984).

78. H. Hasegawa, Phys. Rev. **129**, 1029 (1963).

79. H. F. Staunton, Thesis, Brown University, Providence, U. S. A. (1970).

80. G. E. Pikus, and G. L. Bir, Fizika Tverd. Tela **1**, 1642 (1959)[Soviet Phys. Solid St. **1**, 1502 (1960)], and L. D. Laude, F. H. Pollak, and M. Cardona, Phys. Rev. **3**, 2623 (1971).

81. S. Bogdanovich, S. Kravchenko, D. Simonian, and M. P. Sarachik, unpublished.

82. S. Bogdanovich, and M. P. Sarachik, unpublished.

83. H. J. Herrmann and B. Derrida, Phys. Rev. B **30**, 4080 (1984).

84. A. N. Ionov, I. S. Shlimak, and M. N. Matveev, Solid State Commun. **47**, 763 (1983).

Reproduced with permission of the copyright owner. Further reproduction prohibited without permission.

85. H. F. Hess, K. DeConde, T. F. Rosenbaum, and G. A. Thomas, Phys. Rev. B **25**, 5578 (1982).

86. W. N. Shafarman and T. G. Castner, Phys. Rev. B **33**, 3570 (1986).

87. M. Capizzi, G. A. Thomas, F. DeRosa, R. N. Bhatt, and T. M. Rice, Phys. Rev. Lett. **44**, 1019 (1980).

88. D. J. Bergman and Y. Imry, Phys. Rev. Lett. **39**, 1222 (1977).

89. V. E. Dubrov, M. E. Levinshstein, and M. S. Shur, Zh. Eksp. Teor. Fiz. 70, 2014 (1976) [Sov. Phys. JETP 43, 1050 (1976)].

90. M. P. Sarachik, D. Simonian, S. V. Kravchenko, and S. Bogdanovich, submitted to Phys. Rev. Lett.

91. Youzhu Zhang, Peihua Dai, Miguel Levy, and M. P. Sarachik, Phys. Rev. Lett. **64**, 2687 (1990).

Reproduced with permission of the copyright owner. Further reproduction prohibited without permission.

IMAGE EVALUATION TEST TARGET (QA-3)

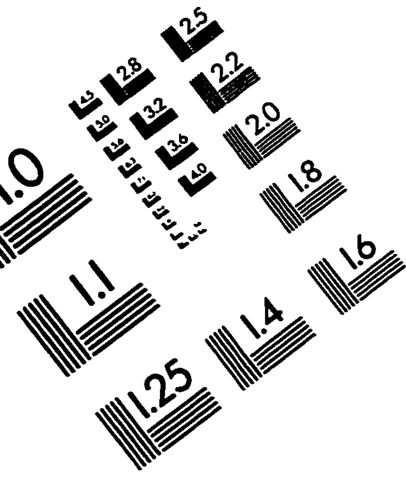
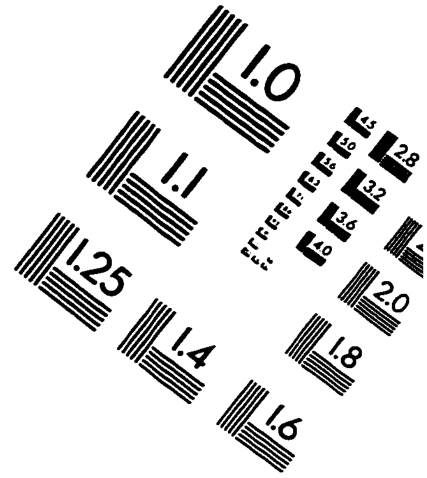
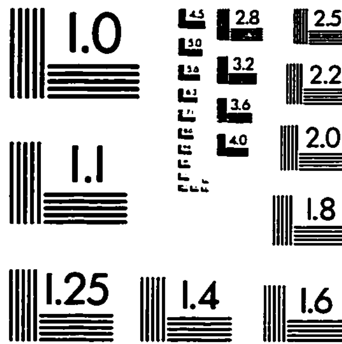
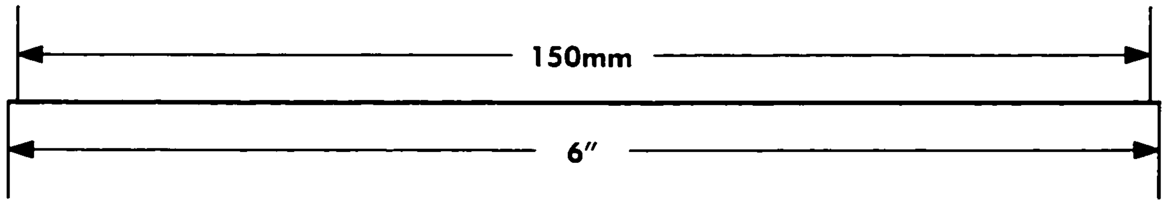

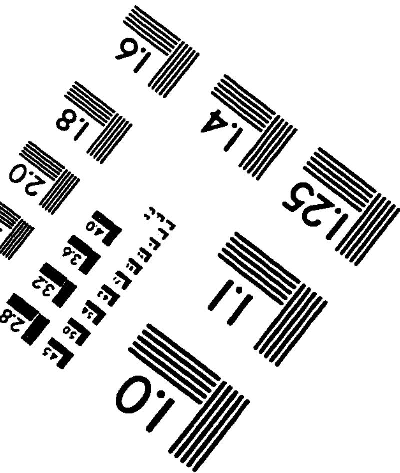
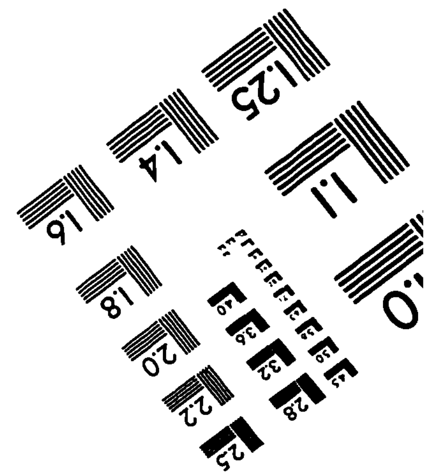

APPLIED IMAGE, Inc
1653 East Main Street
Rochester, NY 14609 USA
Phone: 716/482-0300
Fax: 716/288-5989

© 1993, Applied Image, Inc., All Rights Reserved

Reproduced with permission of the copyright owner. Further reproduction prohibited without permission.